Department of Precision and Microsystems Engineering

Characterization of In-Situ Tensile MEMS Devices for Stress Strain Measurements

Otho Granata

Report no	: 2026.044
Coach	: Vasilis Papadimitriou
Professor	: Gerard Verbiest
Specialization	: HTE-DMN
Type of report	: MSc thesis
Date	: 1 June 2026

Challenge the future

Characterization of In-Situ Tensile MEMS Devices for Stress Strain Measurements

by

Otho Granata

to obtain the degree of Master of Science
at the Delft University of Technology
to be defended publicly on June 16th, 2026 at 9:30am

Student number:	5164249	
Thesis committee:	Dr. G. Verbiest	Delft University of Technology
	Dr. M. K. Ghatkesar	Delft University of Technology
	Dr. V. Papadimitriou	DENSsolutions

TU Delft

Abstract

The mechanical, electrical, and thermal properties of two-dimensional materials such as graphene depend strongly on their applied strain and on the out-of-plane wrinkles and defects present in freestanding membranes. Quantifying the relationship between strain and structure requires applying a controlled load to a sample while simultaneously imaging it at high resolution, which is only achievable with a tensile stage small enough to operate inside an electron microscope. This thesis characterizes two such microelectromechanical (MEMS) devices, both designed for in-situ TEM tensile testing of micro- and nanoscale samples: an electrostatic device based on a comb-drive actuator, and an electrothermal device based on chevron thermal actuators. Both apply a uniaxial strain to a sample mounted across a gap and sense the resulting force through a capacitive comb structure. For each device the actuation, sensing, and operational limits were described analytically as functions of geometry, material properties, and actuation input, and the models were compared against experimental measurements obtained through SEM imaging, Raman thermometry, and capacitive readout. For the electrothermal device, a four-parameter model was fitted jointly to displacement and temperature data and reproduced both datasets well, with each fitted parameter retaining a physical interpretation. For the electrostatic device, the predicted pull-in displacement of 0.61 µm, shown analytically to depend only on the initial comb geometry, was confirmed experimentally, while the capacitance measurement was dominated by parasitics and could not be resolved. Two production-related effects shaped the results: the omitted molybdenum conductive layer, which caused the surrounding chip to heat substantially during thermal actuation, and incomplete deep reactive-ion etching, which restricted functional testing to the 5 µm devices. The two devices are found to be complementary rather than competing, each covering part of the intended measurement space, and the most impactful improvements for future work are identified as incorporating the molybdenum layer, fabricating functional 20 µm devices, and measuring the etched sidewall geometry directly.

Contents

1
Introduction

Graphene and other two-dimensional materials combine atomic thickness with exceptional mechanical, electrical, and thermal properties, making them attractive candidates for applications ranging from flexible electronics to next-generation sensors [1], [2], [3]. In a freestanding membrane, however, these properties are not governed by the ideal lattice alone. Out-of-plane wrinkles and corrugations, which are thermodynamically unavoidable at finite temperature [4], together with grain boundaries and other topographical defects, strongly influence the effective stiffness, carrier mobility, and resistivity of the material [5], [6]. As these features progressively flatten and rearrange under applied strain, the mechanical, chemical, and electronic properties of the membrane change with it [7]. Knowing the stress-strain characteristics could, for example, help replace the comb arrays of capacitive MEMS accelerometers with suspended graphene membranes [8], [9].

Establishing this relationship requires measuring the mechanical response of a sample while simultaneously observing its structure, which conventional tensile testing cannot provide at this scale [10]. The required forces fall in the micro- to millinewton range and the displacements in the micro- to nanometre range, below the resolution of macroscopic load frames, and the deforming structure must be imaged at near-atomic resolution as it is strained. In-situ Micro Electro Mechanical Systems (MEMS) address both needs at once: co-fabricated tensile stages, small enough to fit inside an electron microscope, integrate on-chip actuation and force sensing and enable mechanical loading and high-resolution imaging to be performed together [11], [12].

An in-situ tensile MEMS device must generate a controlled displacement or force on a mounted sample, and measure its resulting straining, all within the confined geometry and vacuum environment of an electron microscope. Different actuation principles trade off force, displacement, speed, and complexity against one another, and no single approach is optimal across the full range of samples of interest. This thesis examines two such approaches, developed at Delft University of Technology and DENSsolutions: an electrostatic device based on a parallel plate actuator, originally designed for measuring Q-factors with 2D materials, and an electrothermal device based on chevron thermal actuators. Both apply uniaxial strain to a sample mounted across a gap and both sense the applied force through a capacitive comb structure, but their differing physical principles give each a distinct operating range and set of limitations.

The aim of this work is to characterize both devices analytically and experimentally, to establish their operating ranges and measurement limits, and to compare their suitability for in-situ tensile testing. The samples used are silicon lamellae, whose elastic and mechanical properties are well characterized and which therefore serve as a validation standard [13], and few-layer graphene membranes as the primary target.

1.1. Thesis outline

This thesis is structured as follows: Chapter 2 introduces the background of in-situ TEM tensile testing, the relevant MEMS actuation and sensing principles and prior work regarding comparable devices. Chapter 3 describes the fabrication of both devices, the resulting structures, including the characteristics and shortcommings as a result of the fabrication steps. Two device specific chapter follow; Chapter 4 covers the electrostatic device, starting with the analytical characterization of its stiffness, capacitance, electrostatic force, and operational limits, continuing with the SEM and capacitance measurements performed. Chapter 5 follows the same structure but revolves around the electrothermal device, with the analytical model fitted to combined SEM and Raman measurements and a sensitivity analysis derived from the fitted parameters. Chapter 6 presents the (in-situ) tensile tests performed on graphene and silicon lamellae. Chapter 7 compares the two devices, discusses their strengths and limitations, and proposes improvements for follow-up research. Finally, chapter 8 closes by summarizing the main findings and answering the research questions posed in Section 1.2.

1.2. Research goals

The objective of this thesis is to characterize two MEMS devices for in-situ TEM tensile testing of samples: an electrostatic device based on a comb-drive actuator and an electrothermal device based on chevron thermal actuators. Both devices apply a controlled uniaxial strain to a sample mounted between the shuttle and a fixed support, and both measure the applied force through a capacitive comb structure. The two designs operate on different physical principles and therefore cover different ranges of force, displacement, and sample stiffness. This work aims to establish the operating range, accuracy, and limitations of each device, both analytically and experimentally.

The work is guided by the following research questions:

1. How can the actuation, sensing, and operational limits of each device be described analytically as a function of geometry, material properties, and actuation input?
2. How well do the analytical predictions agree with measured displacement, capacitance, and (for the thermal device) temperature, and what production-related effects must be included to reconcile the two?
3. What strain range, force range, and samples are within both device's operating window?
4. What is the smallest sample strain that can be resolved through the capacitive readout, and how does this resolution depend on actuated state and sample stiffness?
5. Which of the two devices is preferable for a given sample, and what improvements would extend their reliability and useful range in future work?

The first two questions are addressed in the theoretical and practical characterization sections of Chapters 4 and 5, where the analytical models are derived and compared against practical SEM, Raman, and capacitance measurements. The third and fourth questions are addressed in the sensitivity analysis sections of the same chapters, and combined in the discussion. The comparison and future improvements of both devices can be found in the discussion chapter, answering the last question.

1

2 Background

This chapter introduces the context and prior knowledge needed to understand the device design and characterization described in the following chapters. Section 2.1 describes the challenges of mechanical characterization at the micro- and nanoscale and motivates the use of MEMS-based tensile testing, with particular focus on two-dimensional materials. Section 2.2 covers the operating principles of SEM and TEM and the constraints these environments impose on any in-situ device. Section 2.3 discusses in-situ testing and the advantages of combining mechanical loading with direct imaging. Section 2.4 surveys actuation mechanisms used in tensile MEMS platforms and the available commercial systems. Finally, Section 2.5 shortly introduces the two test materials used in this work.

2.1. Characterization of micro- and nano-scale materials

Conventional tensile testing, gripping a specimen in a load frame and recording the stress–strain response, becomes impractical at the micro- and nanoscale, where the required forces fall in the milli- to micronewton range and displacements are on the order of micro- to nanometres. Specimen fabrication, small-scale force and displacement generation, and high-resolution measurements are the three generic challenges that any small-scale testing platform must address [10]. This motivates the use of microelectromechanical systems (MEMS): co-fabricated tensile stages small enough to fit inside an electron microscope specimen chamber, enabling simultaneous mechanical loading and high-resolution imaging [10], [11].

Measurements at this nanoscale is necessary as thin-film and other nanoscale materials exhibit mechanical properties that differ from their bulk counterparts, owing to increased surface-to-volume ratios and grain-boundary-dominated deformation mechanisms [10], [14]. For two-dimensional materials such as graphene, the presence of out-of-plane wrinkles and corrugations, which are thermodynamically unavoidable at finite temperature [4], further impact its properties. These corrugations suppress carrier mobility, alter electrical resistivity, and reduce effective stiffness relative to a flat membrane [5], [6], [15]. Under uniaxial tension, wrinkles aligned with the stress axis flatten progressively, while those perpendicular to it remain, producing a bi-linear stress–strain response [6], [7]. Quantifying this relationship requires in-situ tensile testing with simultaneous structural observation, which cannot be achieved by conventional means.

One reason for understanding and controlling graphene's mechanical behavior presents itself in accelerometers. In comparison with capacitive MEMS accelerometers, resonant graphene accelerometers have the potential to be smaller [8]. Conventional capacitive MEMS accelerometers rely on capacitive comb arrays whose minimum size is limited by fabrication and by the requirement to maintain measurable capacitances; further miniaturization is therefore limited [9]. Replacing the comb array with a suspended graphene membrane as the sensing element bypasses this constraint, because of the material's atomic-scale thickness and its great electrical and mechanical properties. Practically implementing such devices requires a thorough understanding of how graphene's properties depend on strain and on the initial wrinkle state.

2.2. Electron microscopy

The resolution of all visible-light microscopes is bounded by the Rayleigh criterion, which states that the smallest resolvable distance δ scales proportionally with wavelength λ and inversely with the numerical aperture $\mu sin\beta$:

$$\delta = \frac{0.61\lambda}{\mu sin\beta} \tag{2.1}$$

With a large numerical aperture and near-ultraviolet illumination, the maximum resolution of a visible-light microscope is approximately 200 nm, which is insufficient for nano-, and even micro-, scale structural characterization. Electron microscopes overcome this limitation by replacing photons with electrons, whose wavelength is related to their energy by de Broglie's relation:

$$\lambda = \frac{1.226}{\sqrt{E}} \tag{2.2}$$

A 200 keV electron, which is a realistic value for Transmission Electron Microscopes, has a wavelength of approximately 2.74 pm found with this non-relativistic approximation, in principle, sub-atomic resolution. Including the relativistic correction factor yields a wavelength of 2.51 pm. In practice, the achievable resolution is limited by spherical and chromatic lens aberrations, lens and sample stability, and sample thickness. Increasing the accelerating voltage improves the theoretical resolution but risks knock-on damage, where elastic electron–atom interactions transfer sufficient energy to displace atoms from their lattice positions. Electron microscopes therefore operate at accelerating voltages that balance resolution requirements against sample preservation. The two techniques most relevant to this work, SEM and TEM, differ fundamentally in how they interact with and image the sample, and are described in the following subsections.

2.2.1. Scanning Electron Microscopy (SEM)

A scanning electron microscope (SEM) produces images by rastering, or 'scanning', a focused electron beam across the sample surface and collecting the signals generated by electron beam to sample interactions at each point. The beam is formed by an electron gun, typically a field-emission gun (FEG), and focused to a spot by a series of electromagnetic condenser and objective lenses, with scan coils deflecting it across the sample in a raster pattern. The intensity of the detected signal at each beam position is mapped to a pixel on the display, building the image point by point. SEM operates at accelerating voltages between 1 and 30 keV, which are considerably lower than those used in TEM [16, chap. 5].

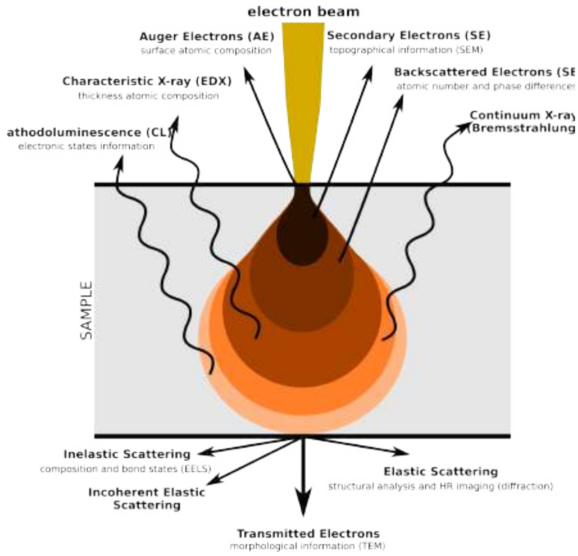

Figure 2.1: Schematic of the electron–matter interaction volume in an SEM, showing the depths from which secondary electrons (SE), backscattered electrons (BSE), and characteristic X-rays originate[17].

When the primary electron beam strikes the sample, it penetrates the surface and loses energy through a series of elastic and inelastic scattering events within a pear-shaped interaction volume whose size depends on the beam energy and sample density. Several distinct signals emerge from different depths within this volume, as illustrated in figure 2.1 , and each carries different information about the sample [17].

Secondary electrons (SE) are low-energy electrons, defined as having energies below 50 eV, ejected from the sample through inelastic scattering. Because of their low energy, they can only escape from the top few nanometers of the surface, making them highly sensitive to surface topography. Steep edges and protrusions emit more secondary electrons than flat regions, producing the characteristic three-dimensional appearance of SE images. SE imaging offers the highest lateral resolution of all SEM signals, with modern field-emission instruments achieving below 1 nm [16, chap. 3].

Backscattered electrons (BSE) are primary beam electrons that are elastically scattered back out of the sample. They originate from considerably greater depths than secondary electrons and carry compositional information: heavier elements with higher atomic numbers backscatter more electrons and therefore appear brighter in BSE images. This makes BSE imaging useful for distinguishing regions of different composition or phase, but at the cost of lower spatial resolution compared to SE imaging, as the signal integrates contributions from a larger interaction volume [16, chap. 2].

When primary electrons displace inner-shell electrons from sample atoms, the subsequent relaxation of those atoms to their ground state releases characteristic X-rays whose energy is unique to each element. These X-rays are collected by an energy-dispersive X-ray spectroscopy (EDS) detector, enabling qualitative and quantitative elemental analysis of the sample [16, chap. 4].

SEM is characterized by a large depth of field, several orders of magnitude greater than that of a visible-light microscope at comparable magnification, which makes it well suited to imaging rough or three-dimensional surfaces. Magnification can be varied continuously over approximately six orders of magnitude [18],[16, chap. 5]. Its main limitations relative to TEM are its inability to resolve atomic structure and the requirement that non-conductive samples be coated or imaged at low voltage to avoid charge accumulation. In this study, SEM was used primarily for in-plane displacement measurements of the MEMS devices, as described in Sections 5.3.4 and 5.2.1.

2.2.2. Transmission Electron Microscopy (TEM)

Where an SEM collects signals scattered back from or emitted near the sample surface, a transmission electron microscope (TEM) detects, as its name suggests, electrons that pass through a thin sample, typically below 100 nm in thickness [19, Ch. 1]. This fundamental difference in operating principle gives TEM its defining characteristics: very high resolution and a shallow depth of field, at the cost of stringent sample preparation requirements regarding thickness, cleanliness, and flatness [19].

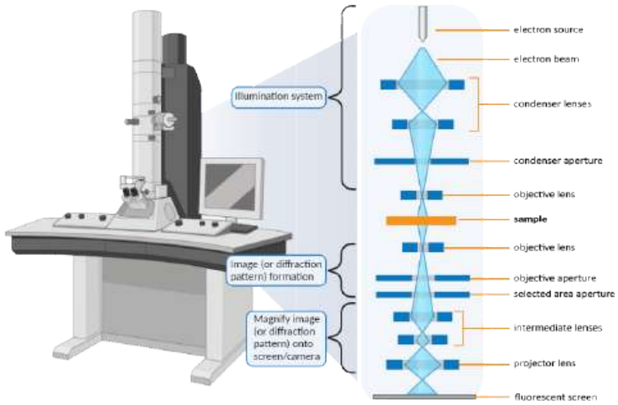

Figure 2.2: Simplified representation of the components and subdivisions of a TEM [20]

As shown in figure 2.2, a TEM consists of three main subsystems. The electron source, in this case a cold field-emission gun (FEG), extracts electrons from a tungsten tip of radius smaller than 100 nm and accelerates them to the desired energy. The condenser lenses then define the size and convergence of the beam at the sample. Depending on the operating mode, the beam is either directed parallel to the sample, as in conventional TEM imaging, or focused to a convergent probe, as in scanning TEM (STEM) and related techniques. After the beam passes through the sample, the objective lens forms an image from the forward-scattered electrons. By adjusting the strength of the intermediate lens, either a magnified image or a diffraction pattern of the sample can be projected onto the detector by the projector lens, as illustrated in figure 2.3,[19].

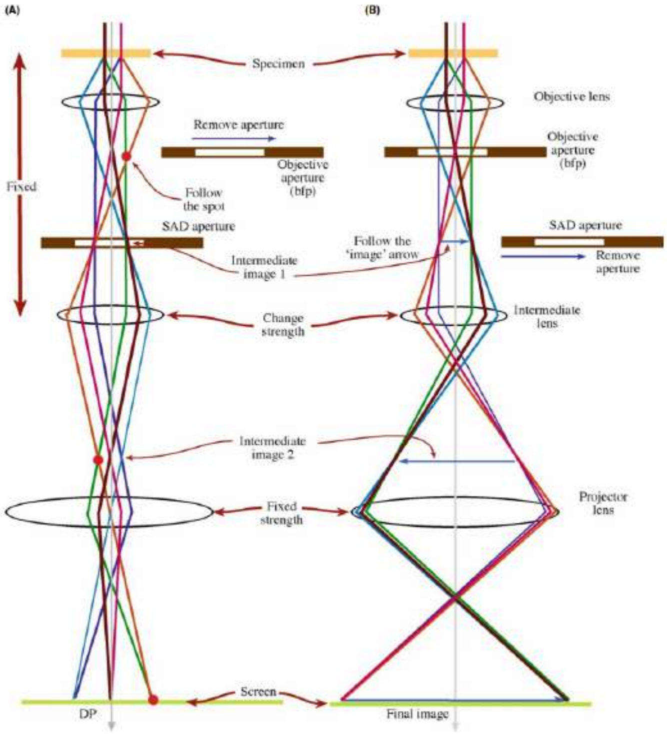

Figure 2.3: The two basic operating setups for TEM measurements. It shows a) the diffraction mode where diffraction patterns are projected on the viewing screen and b) the image mode where a direct image of the sample is projected on the screen. [19]

TEM operates at accelerating voltages that typically equal or exceed 100 keV, which is significantly higher than those used in SEM. This provides the short electron wavelengths needed for atomic-scale resolution but also increases the risk of knock-on damage in beam-sensitive materials. TEM additionally requires a higher vacuum than SEM: while a field-emission SEM operates at around 10^{-4} to 10^{-5} Pa, a TEM column requires 10^{-5} to 10^{-7} Pa, with the gun region of cold-FEG instruments approaching 10^{-8} Pa [19].

2.2.3. EM environment constraints

Operating inside an electron microscope imposes constraints on any in-situ device with respect to size, material selection, and electrical design.

Both SEM and TEM operate under high vacuum, as described in Sections 2.2.1 and 2.2.2. Any in-situ device must therefore be built from low-outgassing materials, and moving parts cannot rely on lubrication. Electrical connections to the device pass through vacuum-compatible feedthroughs in the sample holder.

Physical space in the TEM is severely limited. The pole piece gap of the objective lens is typically 2–6 mm, and standard side-entry holder tips measure 3.3 mm in diameter for Thermo Fisher Scientific (TFS) instruments and 3.0 mm for JEOL instruments [19], [21]. Any device must fit within these bounds while accommodating the sample, actuation mechanism, sensors, and electrical contacts.

Ferromagnetic materials are incompatible with TEM and SEM environments as they interact with the magnetic objective lens and deflect the beam. The choice of conductive materials on the chip and holder is therefore restricted to non-magnetic metals. Combined with the requirement to survive the HF release step of the fabrication process and to be compatible with cleanroom silicon processing, this led to the selection of molybdenum as the conductive layer, as discussed in chapter 3.

Electrically isolated structures accumulate charge under beam irradiation, which distorts the local electric field and deflects the beam, degrading image quality and causing image drift [22]. Figure 2.4 shows an electrostatic device where the fin supports were not grounded; the isolated parts appear significantly brighter than the grounded parts of the device. All conductive parts must therefore be connected to ground through the stage or through the holder contacts.

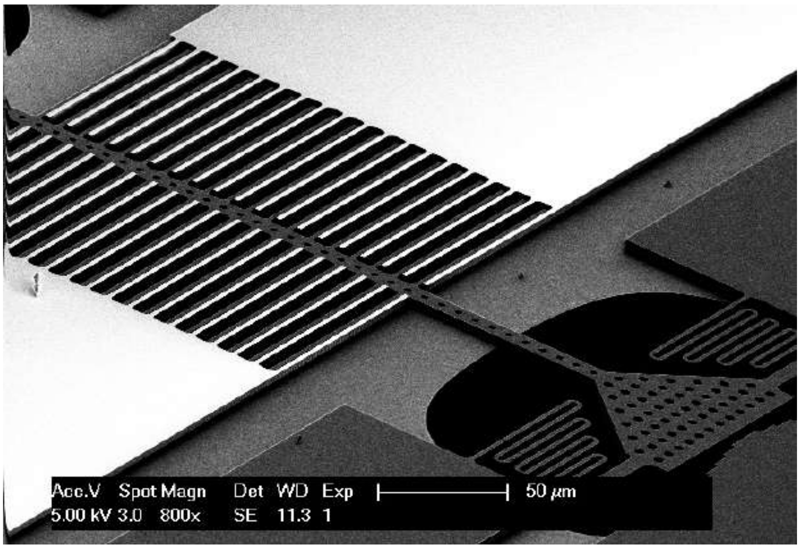

Figure 2.4: SEM image of an electrostatic device where the fin (supports) where not grounded. These electrically isolated parts accumulated charge and show up very bright as compared to the other, grounded, parts of the device.

2.3. In-situ tensile testing

Conventional mechanical testing provides quantitative stress–strain data but offers no direct observation of the underlying microstructural processes. In-situ testing addresses this limitation by performing the mechanical experiment inside the electron microscope column while simultaneously imaging the sample. This allows deformation mechanisms, crack initiation, and structural changes to be directly correlated with the measured mechanical response, rather than inferred from post-failure observation of a sample that has already failed [23, Ch. 7].

Electron microscopes are particularly well suited for in-situ tensile testing of micro- to nanoscale specimens. The high vacuum environment eliminates oxidation and environmental interference during testing. The high spatial resolution, particularly in TEM, allows atomic-scale structural changes to be resolved during loading. And the specimen geometry required for electron transparency, a thin, freestanding membrane, is compatible with the geometry required for uniaxial tensile testing [23].

In-situ TEM systems include a wide range of environmental stimuli beyond mechanical loading, including heating, cooling, electrical biasing, and controlled gas or liquid environments [23]. For thermal and electrical measurements, specialized MEMS-based sample holders provide on-chip actuation, electrical feedthroughs, and environmental control while fitting within the sample space of the microscope column. The devices developed in this thesis are designed to be compatible with DENSsolutions' Lightning holder platform and are described in detail in Chapters 3, 4, and 5.

2.4. State of the art tensile MEMS mechanisms

In-situ tensile testing platforms can be categorized by their actuation mechanism and integration approach. Understanding the trade-offs between different actuation technologies is essential for selecting or designing appropriate platforms for specific testing requirements. In this section, multiple MEMS actuation mechanisms are discussed and the commercial availability shortly mentioned.

Figure 2.5: Sideview of a sample holder where the tip (right) holds the sample [24]

2.4.1. Actuation mechanisms

Tensile testing devices employ four actuation mechanisms: piezoelectric, electrothermal, electrostatic, and bimetallic actuators, each with distinct advantages and limitations. Piezoelectric, electrothermal, and electrostatic actuation are the most widely used in modern MEMS tensile platforms, while bimetallic actuation is less common due to fabrication complexity and reliability concerns [11].

Piezoelectric actuation Piezoelectric actuators utilize the piezoelectric effect, where mechanical strain is induced by an applied electric field [25]. Commercial nanoindentation systems such as the Bruker Hysitron PicoIndenter series employ piezoelectric actuators for positioning and force application. Zhang et al. [26] note that compared to electrothermal MEMS actuators, piezoelectric systems possess capabilities such as high frequency response, low power consumption, and no hysteresis.

The Hysitron PI 89 SEM PicoIndenter, see figure 2.6, achieves load ranges from less than 1 μN to 3.5 N with displacement control from less than 1 nm to 150 μm [27]. The PI 95 TEM PicoIndenter provides similar capabilities within TEM pole-piece constraints [27]. These systems utilize three-plate capacitive transducers for force and displacement sensing, achieving noise floors as low as 2 nN force and 0.02 nm displacement [27].

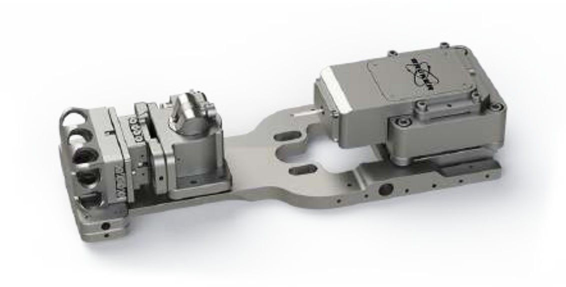

Figure 2.6: Render of Bruker Hysitron pi 89 auto picoindenter [27]

Piezoelectric systems are typically external to the specimen holder. In TEM applications, the piezoelectric actuator pushes against a MEMS platform or push-to-pull device [12]. See figure 2.7 for two such examples from literature. This configuration introduces additional compliance into the load train and requires careful design of the mechanical interface between the external actuator and the on-chip device.

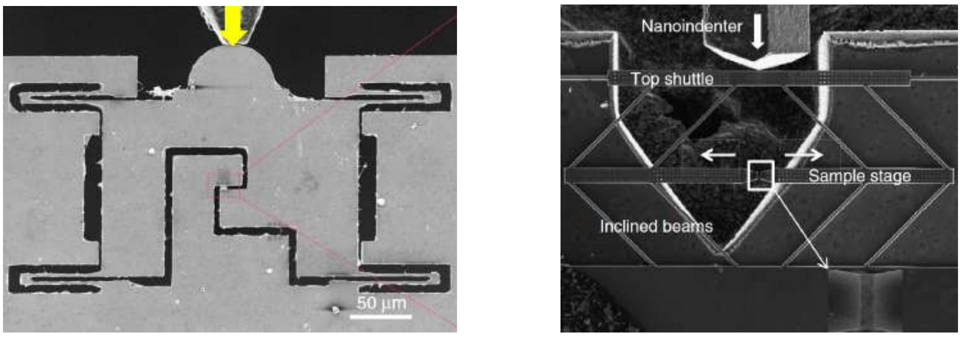

(a) (b)

Figure 2.7: Two in-situ tensile mechanism with external pico-indenter [28] and [29] respectively.

The primary limitations are the external actuation requirement and higher cost compared to integrated MEMS actuators. External actuation necessitates more complex sample holder designs and may introduce additional sources of mechanical compliance that reduce measurement precision [11].

Electrothermal actuation Electrothermal actuators exploit thermal expansion induced by Joule heating to generate displacement [30]. The most common design uses V-shaped or chevron beams: when voltage is applied across the inclined freestanding beams, current flow causes Joule heating and thermal expansion [31]. The thermal fins connect to a central shuttle which then translates as a result of this thermal expansion.

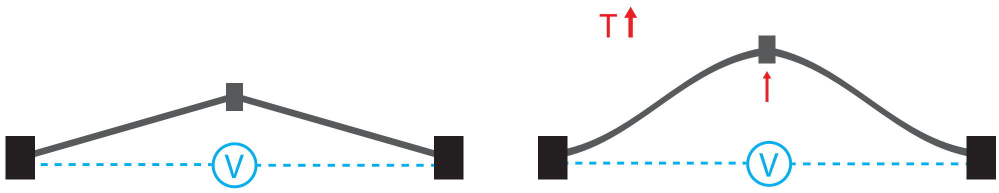

Figure 2.8: Schematic of chevron fin actuation mechanism, where joule heating of the fins results in their thermal expansion which, given the geometry, actuates the shuttle.

Thermal actuators can deliver large forces up to tens of millinewtons and moderate displacements up to tens of micrometers [32]. Phinney et al. [30] report that thermal microactuators have higher output force and lower input voltage compared to electrostatic actuation methods.

In general, the thermal actuator is displacement controlled, prescribing the displacement to the specimen for a given supplied voltage [32]. However, the effective control mode depends on the relative stiffnesses of the actuator beams, supporting flexures, and test specimen. This mechanical behavior is analyzed in detail for the thermal device developed in this work in Chapter 5.

Baracu et al. [33] report operating powers as low as 51 mW (at 0.2 V and 257 mA) for chevron-type thermal actuators achieving 12 µm displacement. Operating temperatures can reach several hundred degrees Celsius, often up to ≈ 600 °C or more, in the heated beams [30], where the shuttle temperature rise is typically kept much lower due to thermal isolation design [34].

The primary limitation is actuation speed. Ramachandramoorthy et al. [35] stated that the maximal displacement rate, after which nonlinearities occur, were around 10 µm s^{-1}. Additionally, thermal actuators consume more power than electrostatic alternatives [36] and introduce temperature gradients that may affect temperature-sensitive specimens [37].

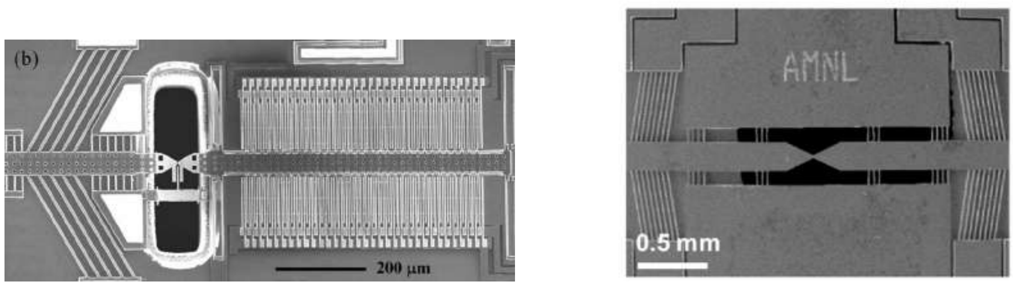

(a) (b)

Figure 2.9: a) A thermal tensile device with an actuating and sensing side from [29] and, b) a thermal tensile device with symmetrical actuation from [38].

Electrostatic actuation Electrostatic actuators generate force through electrostatic attraction between charged electrodes. Two primary designs are employed in MEMS tensile devices: parallel-plate (gap-closing) actuators and comb-drive (interdigitated) actuators.

Parallel-plate actuators consist of two opposing electrodes separated by a gap. When voltage is applied, electrostatic attraction draws the electrodes together. The force scales quadratically with voltage and inversely with the square of the gap spacing, resulting in nonlinear force-displacement behavior [39]. This design is susceptible to pull-in instability, where the electrostatic force exceeds the mechanical restoring force, causing the movable electrode to snap to the fixed electrode [40].

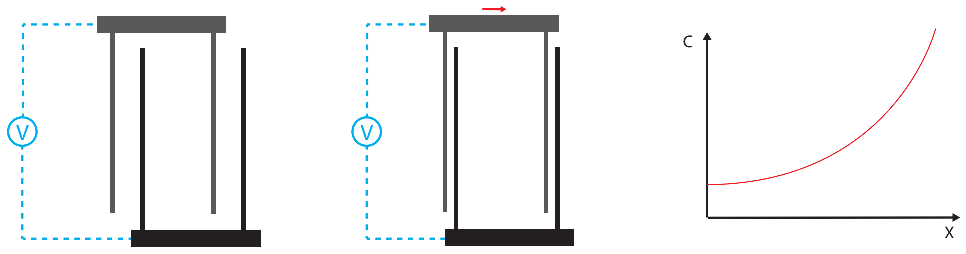

Figure 2.10: Schematic of working principle of parallel plate actuation with a figurative visualization of the capacitance change with displacement

Comb-drive actuators use interdigitated finger electrodes that slide laterally relative to each other [41]. The electrostatic force in a comb drive is proportional to the applied voltage and the number of comb fingers, but remains approximately independent of displacement within the linear operating range [42]. This provides more stable operation and avoids the pull-in instability characteristic of parallel-plate designs.

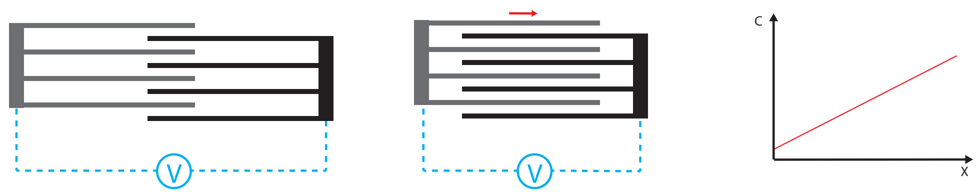

Figure 2.11: Schematic of working principle of comb-drive actuation with a figurative visualization of the capacitance change with displacement

Zhu and Espinosa [32] explain that the comb drive actuator is force controlled, whereas the thermal actuator is displacement controlled. Li et al. [42] note that compared to electrothermal actuators, comb-drive actuators can provide constant force under constant actuation voltage regardless of travel distance and with no heating effect.

This force-controlled operation enables precise load application and high-speed testing. Li et al. [42] demonstrated displacement rates exceeding 220 $\mu m\,s^{-1}$ with electrostatic actuators, compared to approximately 10 µm s^{-1} for thermal actuators [36], representing a two-order-of-magnitude improvement in actuation speed.

The absence of heating effects makes electrostatic actuation ideal for applications requiring precise temperature control or high strain rate measurements [11]. The fast response time allows capture of transient events such as dislocation bursts and fracture initiation [42].

The main disadvantages are lower force output compared to thermal actuators and higher operating voltages, typically tens of volts [32]. Electrostatic actuators are also susceptible to stiction between closely spaced electrodes that must be considered in device design [40]. In chapter 4, a parallel plate electrostatic device and its working principles are discussed in higher detail.

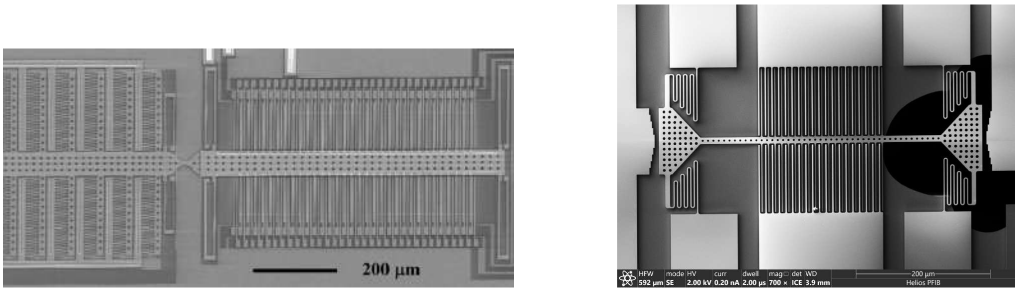

(a) (b)

Figure 2.12: Two electrostatically actuated devices with, a), comb-drive [11] and, b), parallel plate mechanisms. The second device, with parallel plate actuation is studied in this thesis.

(Pseudo) Bimorph actuation Bimetallic or bimorph actuators exploit differential thermal expansion between materials with different thermal expansion coefficients [43]. A complete in-situ device and its mechanism is shown in figure 2.14. Liu et al. [44] describe bimetallic arms where each arm comprises two layers of different materials with widely distinct thermal expansion coefficients, so that they can deflect considerably even at relatively low operating temperatures.

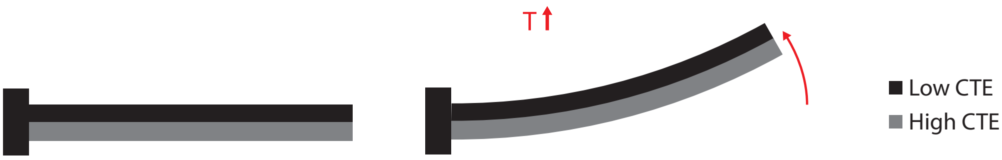

Figure 2.13: Illustration of working mechanism of a bimorph cantilever. When temperature is increased, the difference in thermal expansion of both materials results in bending.

Bimetallic actuators bond two materials together creating a bilayer structure. When heated uniformly, the material with higher thermal expansion coefficient expands more than the material with lower coefficient, causing the structure to bend out of plane.

For small displacements, this deflection is proportional to the temperature change, the difference in thermal expansion coefficients, and the length of the bimetallic beam [43].

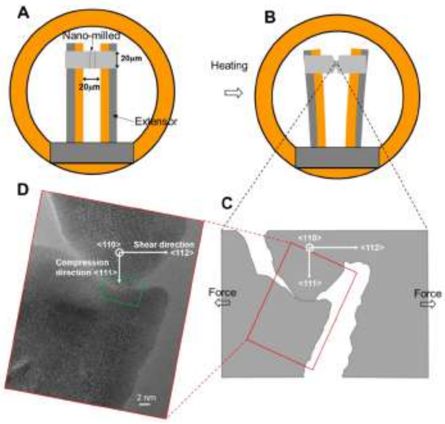

Figure 2.14: Working mechanism and design of a tensile device with which atomic resolution was achieved tracking of grain boundaries at atomic scale, see [45]

Bimetallic actuators suffer from several limitations that restrict their widespread adoption. The bonded interface between dissimilar materials is prone to delamination during thermal cycling, particularly at the elevated temperatures required for significant actuation [46]. Fabrication complexity is higher than single-material thermal actuators due to the need for depositing, patterning, and bonding dissimilar materials without introducing excessive residual stress [47]. The out-of-plane bending motion requires more complex integration into planar tensile testing geometries compared to in-plane actuators. These factors have led to limited use of bimetallic actuation in modern MEMS tensile devices compared to thermal and electrostatic alternatives.

Pseudo-bimorph designs achieve similar functionality using differential heating of a single material rather than relying on differing thermal expansion coefficients [47]. These designs are simpler to fabricate but typically produce smaller displacements.

Figure 2.15: When current flows through the structure, the thin arm, hot side, experiences joule heating and expands while the thick arm remains at a lower temperature, cold side. This asymetrical expansion results in actuation.

Bimetallic actuators can generate large displacements at relatively low temperatures compared to single-material thermal actuators, as the bending deflection amplifies the thermal expansion [47]. They have been demonstrated in TEM tensile holders [44] and various MEMS devices [43].

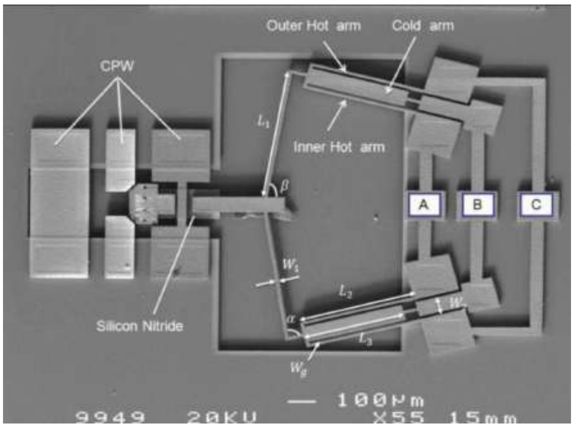

Figure 2.16: SEM image of a RF MEMS switch actuated through pseudo-bimorph structures, from [48]

2.4.2. Commercial and research platforms

Commercial in-situ mechanical testing platforms are available from several manufacturers. DENSsolutions (Delft, Netherlands) offers MEMS-based heating, cooling, environmental (liquid or gaseous), and electrical biasing holders. The Lightning holder platform, which provides heating up to 900 °C with 6–8 electrical device contacts for electrical biasing and sensor readout [24]. Bruker provides the Hysitron PicoIndenter series for SEM and TEM, using piezoelectric actuation with capacitive force sensing [27]. The PI 89 supports techniques including nanoindentation, tensile testing via push-to-pull devices, pillar compression, and tolerates elevated testing temperatures up to 1000 °C [27]. Hummingbird Scientific, Protochips, Gatan, and Bestron also manufacture in-situ holders with various capabilities including heating, cooling, electrical biasing, and gas/liquid environments [21].

Research platforms demonstrate the wealth of MEMS tensile testing approaches. Zhu and Espinosa [32] developed an influential early platform combining thermal actuation with capacitive sensing for force measurement and displacement control, enabling quantitative tensile testing of nanowires inside SEM and TEM. Espinosa et al. [11] extended this work with true displacement control and feedback mechanisms critical for capturing softening events during plastic deformation. More recent work has integrated high-temperature capabilities [49] and atomic-resolution imaging during testing [45].

Huang et al. [12] note that MEMS devices utilize on-chip actuation (thermal or electrostatic actuators) and load sensors (capacitive sensors or flexible beams), enabling compact, cost-effective testing platforms compatible with both SEM and TEM. The small size and customizable functional design of MEMS technology offers advantages over external piezoelectric systems in terms of compactness and integration within microscope geometries [12].

2.5. Test samples

In this thesis, tensile tests are performed with two materials: silicon lamellae as calibration specimens and suspended graphene membranes as the primary target for mechanical characterization. Sample preparation and transfer are described in Chapter 6.

Silicon lamellae, prepared by focused ion beam (FIB) milling, serve as calibration specimens owing to their well-characterized mechanical properties. Silicon's elastic properties are known with high accuracy, with Young's modulus in the $\langle 110 \rangle$ crystal direction equal to 170 GPa [13], making it well-suited for validating the displacement and force measurement systems. These specimens provide a baseline for assessing device performance.

Suspended graphene membranes are the primary target for mechanical characterization. As discussed in Section 2.1, graphene's out-of-plane wrinkles produce a characteristic bi-linear stress–strain response, which in-situ testing helps quantify [6], [7]. The combination of simultaneous imaging and mechanical loading enables direct correlation between wrinkle morphology and mechanical response.

3
Production

This chapter describes the fabrication of the MEMS chips used for tensile testing. Both the electrostatic and electrothermal devices are produced on a single SOI wafer using a multi-step photolithographic process. Section 3.1 outlines this process flow step by step, and Section 3.2 covers the practical side: the issues encountered during the first fabrication runs—over-release of structural supports during the vapor HF step, the omitted molybdenum layer in a simplified variant, and incomplete frontside etching of the thicker devices—and their implications for device behavior.

3.1. Production process flow

Both the electrostatic and electrothermal devices are fabricated on a single SOI wafer, one half of the wafer dedicated to each device type. The process begins with an SOI wafer consisting of three layers: a thin monocrystalline silicon device layer (5 or 20 µm), a 1.5 µm buried silicon dioxide layer, and a 400 µm silicon handle or structural wafer, see figure 3.1. The buried oxide serves as both an electrical insulator between the device and the handle wafer as well as a self-terminating etch stop during deep silicon etching. At each photolithographic step, a stepper sequentially exposes a photoresist-coated wafer through a mask, transferring the device geometry into the resist before the underlying layer is etched or deposited upon. The complete process is condensed to eight steps, described below.

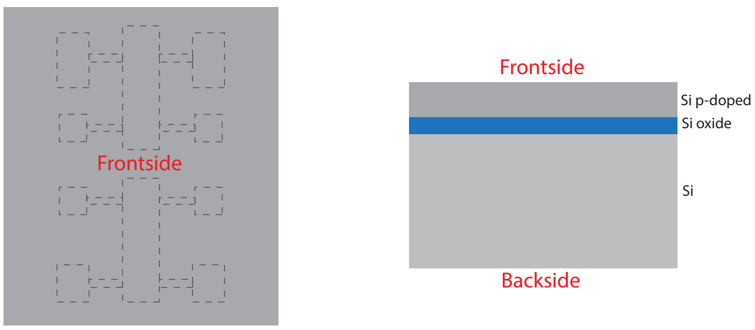

Figure 3.1: Initial SOI wafer structure and materials shown form the top (left) and with a crossection (right). The dashed figure on the top-view acts shows the location and shape of the future finished device. All colors and layout remain constant in subsequent visualizations of the production process.

1. **Silicon Nitride ($SiNx$) Deposition and Patterning:** A ~500 nm layer of silicon nitride ($SiNx$) is deposited on both the frontside and backside of the wafer by

Plasma-Enhanced Chemical Vapour Deposition (PECVD). On the frontside, the layer is subsequently patterned by photolithography and etching, leaving $SiNx$ only in the regions where metal conductors will later need to be electrically insulated from the underlying silicon device layer. The purpose of the $SiNx$ is to serve as an electric isolation layer. On the backside, the SiN_x layer protects the handle wafer surface during subsequent processing steps. Silicon nitride is preferred over silicon dioxide as an isolation material for several reasons: it has a higher dielectric constant, lower leakage current, acts as a diffusion barrier preventing metal contamination of the device layer, and — mainly — is highly resistant to HF, meaning it survives the vapor HF release step at the end of the process intact [50], [51].

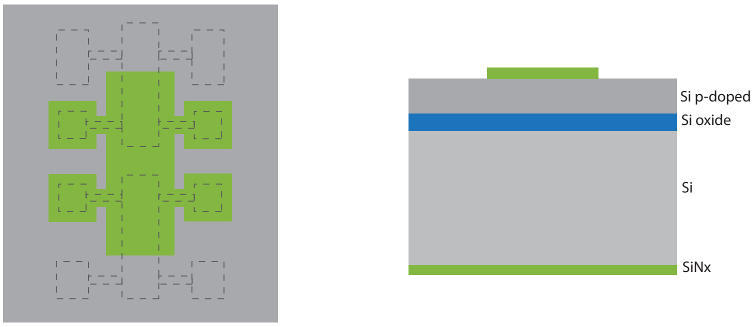

Figure 3.2: Silicon Nitride, green, is deposited on the back and front. On the front, the silicon nitride is solely patterned where the biasing probes connect.

2. **Metal Deposition and Patterning:** A 100 nm layer of molybdenum (Mo) is sputter-deposited over the entire frontside, covering both the patterned SiN_x regions and the exposed silicon, and subsequently patterned by photolithography to define the conductive wires and contact pads. Where Mo is deposited on SiN_x, it forms electrically insulated conductor traces; where contact pads sit directly on silicon, they form an electrical contact to the device layer. The latter is essential for the electrothermal device, whose actuation relies on current flowing through the silicon device layer itself. Molybdenum is chosen for several reasons. Most critically, it is not attacked by hydrofluoric acid, allowing it to survive the vapor HF release step intact [52]. It is also non-magnetic, making it compatible with both TEM and SEM environments where ferromagnetic materials would interfere with the electron beam [53]. Finally, unlike metals such as copper and gold, which are classified as deep-level silicon contaminants and are restricted in standard cleanroom environments, molybdenum is fully compatible with silicon processing and is a well-established material in MEMS fabrication [54].

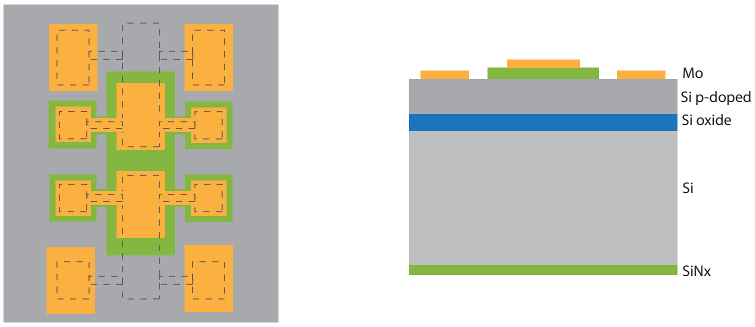

Figure 3.3: The added Molybdenum, yellow, placed on the conductive wires and biasing paths.

3. **Frontside Oxide Deposition (DRIE Hard Mask):** A 200 nm layer of silicon dioxide is deposited by PECVD over the entire frontside, covering the Mo conductors, the $SiNx$, and the exposed silicon. This layer serves as the hard mask for the subsequent frontside DRIE. This step is necessary as photoresist alone cannot withstand the extended plasma exposure required to etch through the silicon device layer[55].

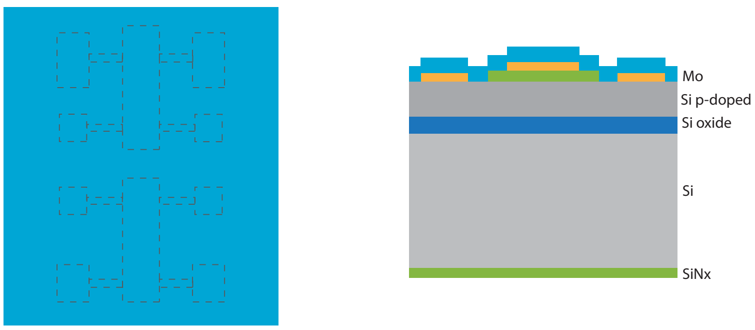

Figure 3.4: Resulting wafer composition with the, newly added, frontside silicon dioxide layer covering the entire frontside.

4. **Backside Oxide Deposition (DRIE hard mask):** A ~3 µm layer of SiO_2 is deposited on the backside by PECVD. This mask is significantly thicker than the frontside equivalent because it must withstand etching through the full 400 µm handle wafer, a considerably longer process that places greater demands on mask selectivity [56].

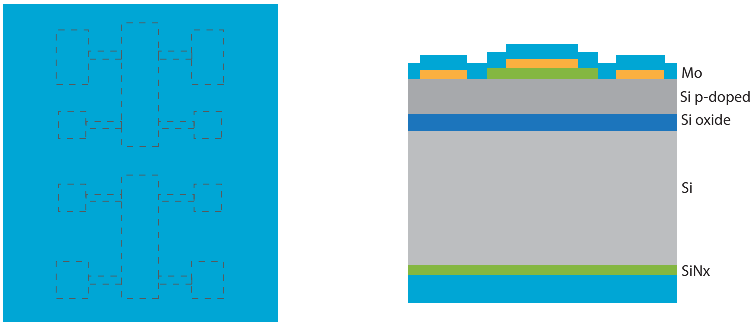

Figure 3.5: After the backside oxide deposition a thick, ~3 µm, layer of silicon dioxide is added to the bottom.

5. **Frontside and Backside Lithography:** Both oxide layers are patterned in this step. The backside oxide is patterned first using photolithography and Deep Reactive Ion Etching (DRIE), opening windows where the handle silicon must be removed by backside DRIE. DRIE is anisotropic because the ions in the plasma are accelerated normal to the wafer surface by the bias voltage, so the etching proceeds primarily downward rather than laterally [57]. This step requires accurate double-sided alignment to the frontside features, as any lateral offset would misplace the backside cavity relative to the device structures above it. The frontside oxide is then patterned by RIE, opening windows in the device geometry and exposing the Mo layer beneath. The exposed Mo is wet-etched using hydrogen peroxide (H_2O_2), which oxidises Mo selectively without attacking SiN_x, SiO_2, or silicon [58]. The SiN_x now exposed beneath the etched Mo regions is subsequently removed by RIE, ensuring the silicon surface is fully accessible for the subsequent DRIE step.

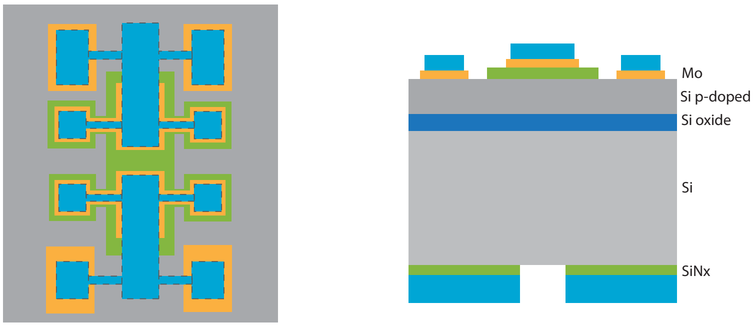

Figure 3.6: After frontside and backside lithography, silicon dioxide is removed where the subsequent DRIE etching will take place.

6. **Backside DRIE:** Deep Reactive Ion Etching (DRIE) is performed from the backside

through the full 400 µm silicon handle wafer, stopping automatically on the buried SiO_2 layer [59]. The Bosch process is used: alternating cycles of SF_6 isotropic etching and C_4F_8 sidewall passivation produce deep, near-vertical trenches with aspect ratios far beyond what is achievable with wet or conventional RIE etching [60]. With the specific cleanroom recipe for these chips, each DRIE cycle etches around 1 µm of material. Processing the backside first, while the wafer remains structurally intact, avoids the handling risks associated with a partially released wafer.

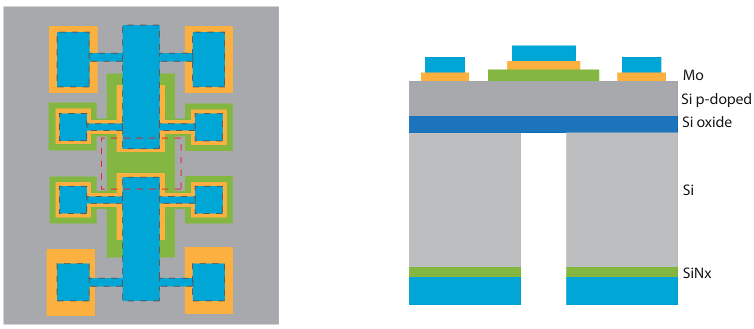

Figure 3.7: After backside DRIE, the handle wafer is fully etched through beneath the device structures, stopping on the buried SiO_2 layer.

7. **Frontside DRIE:** With the backside complete, DRIE is performed from the frontside through the silicon device layer (5 or 20 µm) using the patterned oxide as a hard mask, stopping on the buried oxide layer. At this stage the device layer is fully patterned in-plane but remains mechanically supported by the buried oxide layer beneath it.

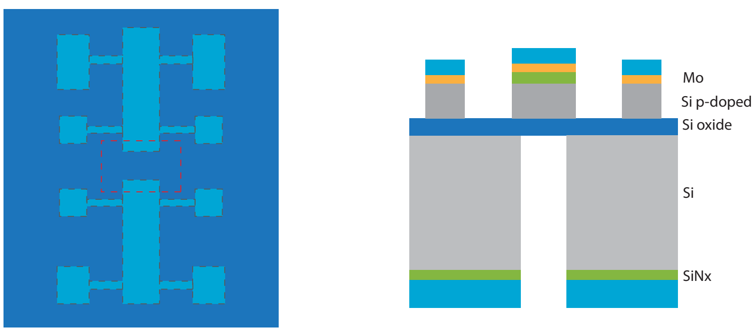

Figure 3.8: After frontside DRIE, the device layer is fully patterned but remains connected to the buried oxide layer.

8. **Device Release with Vapor HF:** The final step selectively removes the buried

silicon dioxide layer *HF* attacks SiO_2 but leaves all other layers, molybdenum, silicon nitride, and monocrystalline silicon, unaltered [61]. Vapor *HF* is used rather than liquid *HF* to avoid stiction: liquid etchants introduce a liquid-vapor interface during drying whose capillary forces can permanently adhere released structures to the substrate, for which the capacitive fins of the devices are especially sensitive [62]. Large footprint structures, such as the contact pads and device base, remain anchored to the handle wafer as the *HF* cannot reach sufficiently far beneath them [61]. Narrower features, such as the flexures, fins, and shuttle, are fully undercut and released. To promote release of larger suspended areas, perforations are introduced, providing additional *HF* access points to the oxide beneath.

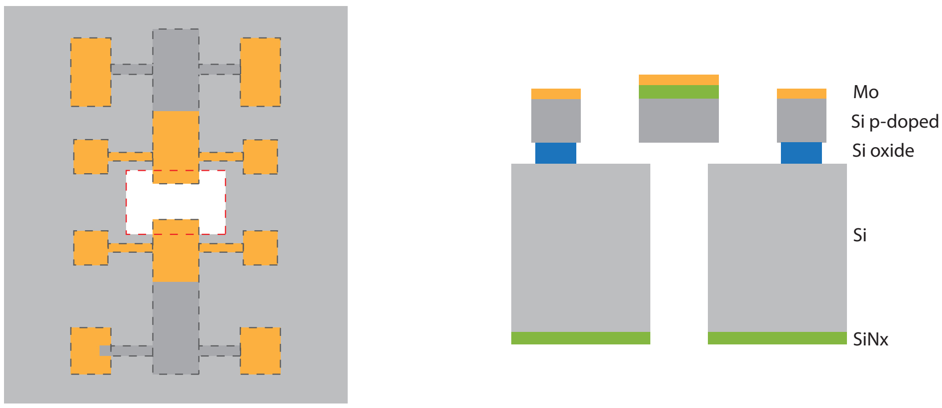

Figure 3.9: After vapor *HF* release, narrow suspended features are freed from the buried oxide while large-footprint structures remain anchored to the handle wafer.

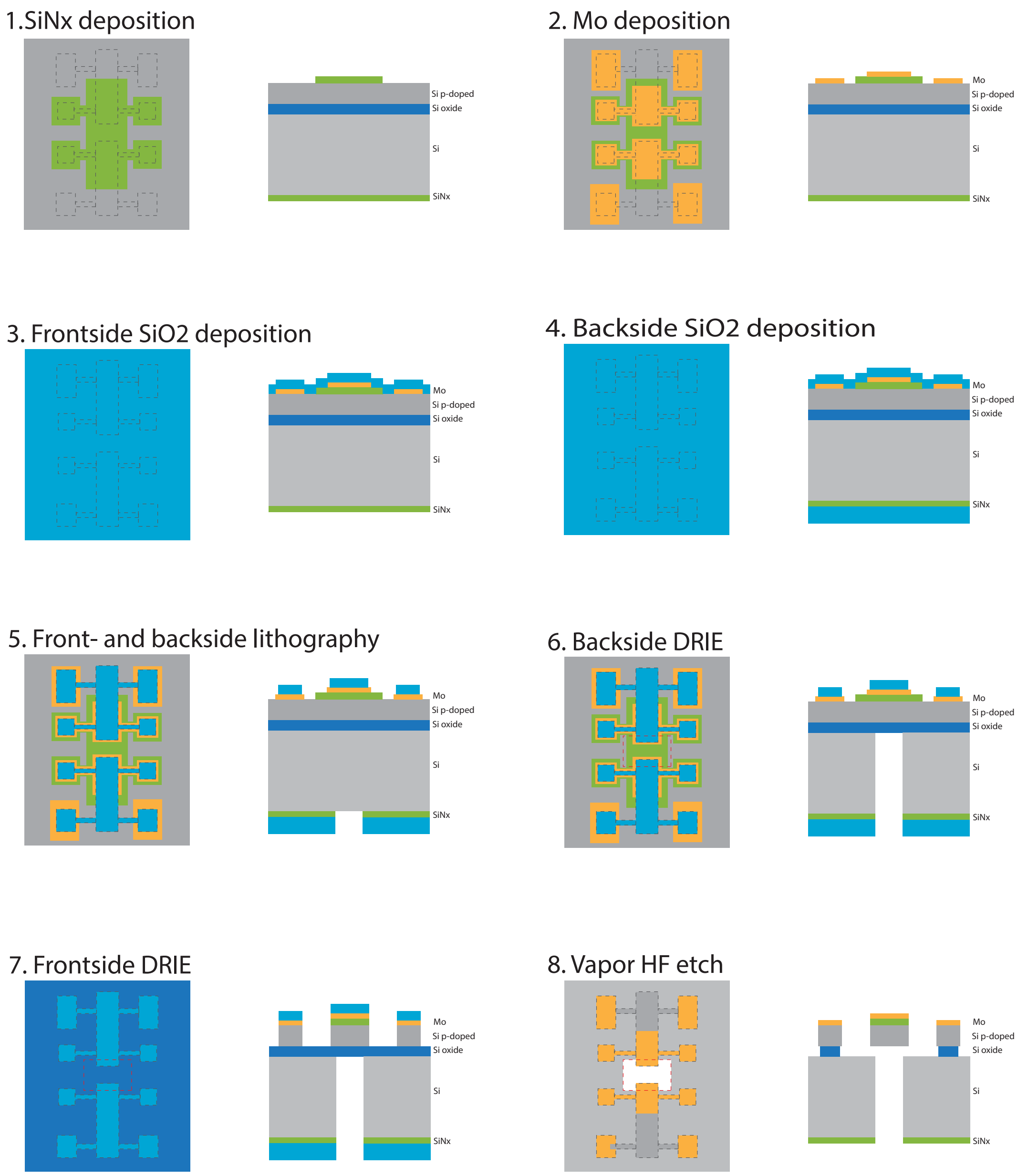

Figure 3.10: Figure combining all 8 production steps

3.2. Practical production

The fabrication of the first production runs revealed several issues affecting device yield and functionality. The main issues encountered are: over-release of structural supports during the vapor *HF* step, simplification of the devices, and insufficient frontside DRIE in the 20 μm devices. Additionally, a deliberate simplification was made to the first production run, to promote faster production, by omitting the molybdenum layer, the implications of which are discussed separately. Not all issues affect all device variants equally, and where relevant the specific impact on the electrostatic or electrothermal device, or on a particular chip format or thickness, is noted.

3.2.1. Overetching

During sample transfer, structural supports of some devices detached, indicating that the vapor *HF* etched beyond what is required for the intended partial release. Inspection of detached device layer parts revealed that the buried oxide beneath these supports had, at some locations, been almost entirely removed. This was most apparent near the backside windows, where the *HF* vapor had better access to the oxide. Since the vernier supports that detached have a relatively large footprint compared to the flexures and other narrow structural elements, it is likely that over-release affects the latter even more severely given their smaller contact area with the buried oxide.

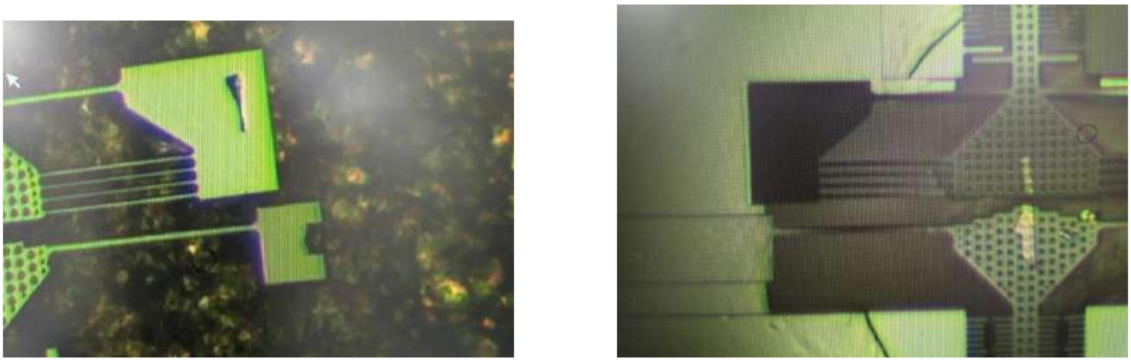

(a) (b)

Figure 3.11: Images of transfer failure as a result from overetched supports also showing how much support is missing. The images are taken during graphene transfer.

This over-release introduces fragility and has two distinct consequences. First, supports could detach during sample transfer compromising mechanical integrity rendering the device virtually useless. Secondly, the same could happen during actual tensile testing. Even if the device would not break, the uncertainty of its structural integrity introduces doubts of results. Checking if a device is functioning properly after every test is time intensive and impractical. A supplementary SEM image, see figure 3.12, shows the underetch distance of one such feature.

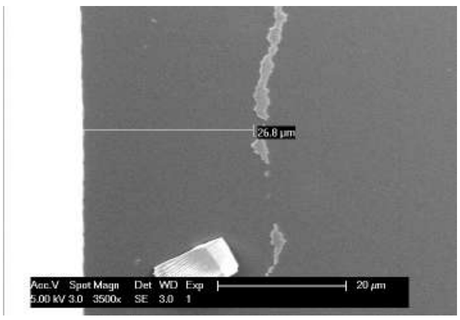

Figure 3.12: SEM image of the residual Silicon Oxide underneath the broken feature shown above (see figure 3.11). The measurement shows the underetch distance at this particular feature.

Overetching of the conductive paths could also result in handle wafer to conductive wire contact which, should this be the case, would increase or enable leakage currents.

3.2.2. Device simplification

To reduce production time and cost, the first production run used a simplified device variant in which the molybdenum conductive layer was omitted. The *Mo* layer serves two purposes: enabling four-point bias measurements, which require the sample to be electrically isolated from the shuttle and connected through a dedicated conductive pad, and reducing the electrical resistance of the on-chip wiring. The former is not required for the initial device characterisation and exploratory tensile tests performed in this study and can therefore be omitted without consequence. The latter, however, has implications for the electrothermal device: without *Mo*, current must flow entirely through the p-doped silicon device layer, whose resistivity is orders of magnitude higher than that of molybdenum. This introduces unwanted Joule heating along the conductive path outside the thermal actuator. The electrostatic device is unaffected as its actuation currents are negligible. The extent of this effect differs between the JEOL and TFS chip formats due to their different wire path lengths, see figure 3.13. Using equation 3.1, the path resistance is estimated for both formats and thicknesses, with and without *Mo*.

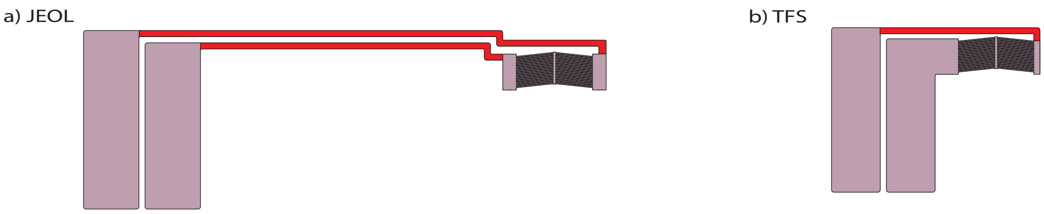

Figure 3.13: The electrical circuit for the electrothermal actuator of the JEOL, a, and TFS, b, chip architecture. The conduction wire path is highlighted in red.

The electrical resistance is calculated as follows:

$$R = \frac{\rho L_{path}}{wt} \tag{3.1}$$

Where ρ is the resistivity of the conductor, L_{path} the conductive wire path length, w the width and t the thickness of the cross-section, see figure 3.14.

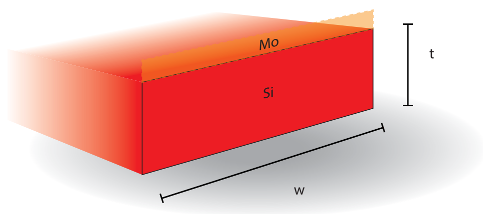

Figure 3.14: Cross-section of a conductive wire, where the device layer p-doped silicon is highlighted in red and the, absence of, the molybdenum layer is suggested in yellow.

The JEOL chips have a total wire path length of around 6,2 mm while that of the TFS chips is only 1,3 mm. Below, in table 3.1, the path resistances for each device version, JEOL or TFS, with different thicknesses and conductive wire material are shown.

	w_{cond} [µm]	$\mathbf{L_{cond}}$ [mm]	**Material**	ρ_0 [Ωm]	$\mathbf{t_{cond}}$ [µm]	**R** [Ω]
JEOL	50	6.2	Silicon (p-doped)	1/5000	5	4960
					20	1240
			Molybdenum	$1/2e7$	0.1	62
TFS	50	1.3	Silicon (p-doped)	1/5000	5	1040
					20	260
			Molybdenum	$1/2e7$	0.1	13

Table 3.1: Here all values for the wire paths and their respective electrical resistance are shown. The electrical conductivity values of the materials are taken at room temperature.

Without Mo conductors, the full actuation current flows through the silicon device layer along the entire wire path. For the TFS chip, the resistance of the thermal actuator fins is approximately one tenth of the total path resistance, meaning that only one tenth of the total electrical power is dissipated in the actuator itself, the remaining nine tenths heat the surrounding chip. This is undesirable as it may affect the mechanical properties of the sample, and it risks damaging the TEM or SEM holder. The situation is worse for the JEOL chips, whose wire paths are approximately five times longer than those of the TFS chips, further increasing the fraction of power dissipated outside the actuator.

To assess how much of the chip heats up in practice, probe point Raman spectroscopy measurements were performed at multiple locations along the chip, see chapter 5.2.2.

Using sputtering, some devices were coated with a thin, ~100 nm, layer of gold with the intention of increasing the conductivity of the wires. A mask, see 3.15a, was made to block the gold from coating the thermal actuator. This layer of gold is too thin, as compared to the device layer, to result in short circuits in between the conductive wires. After sputtering, these masks could be hard to remove and a pair of tweezers is used to push the chip loose, hence the scratches of the gold.

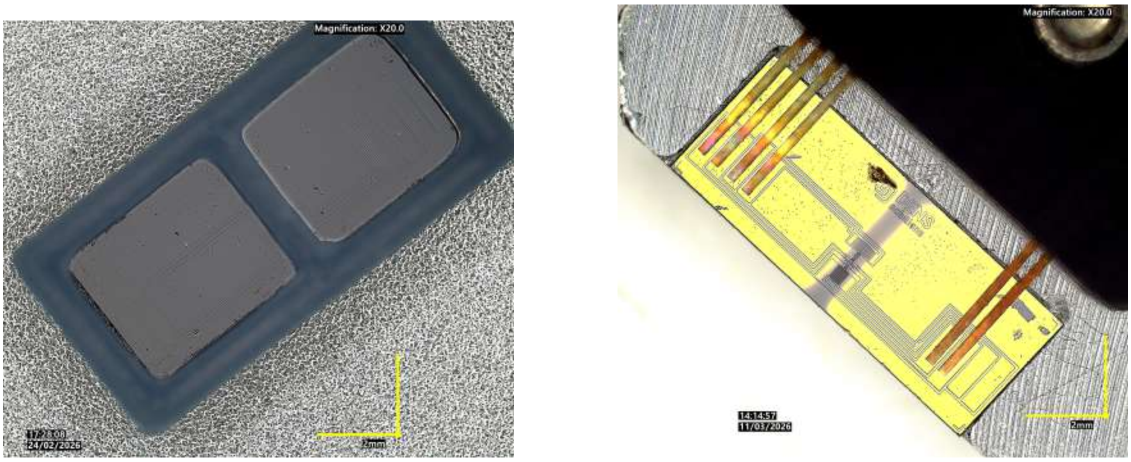

(a) (b)

Figure 3.15: a) A JEOL chip placed under the sputtermask and b) the resulted gold coat with a scratchmark at the right most corner for raman probepoint measurements. From b) it is clear that the sputtermask prevented gold from depositing on the device itself.

These devices were tested but the resistance through the device seemed significantly higher then expected. After closer inspection, the piece of wire just above the thermal actuator, which wasn't gold coated, was found to have a large impact, especially when increasing the actuation voltages where this conductive wire would heat up noticeably. At setpoints, where around 20 mA flowed through the wires, it was even possible to see the thermal radiation with the naked eye.

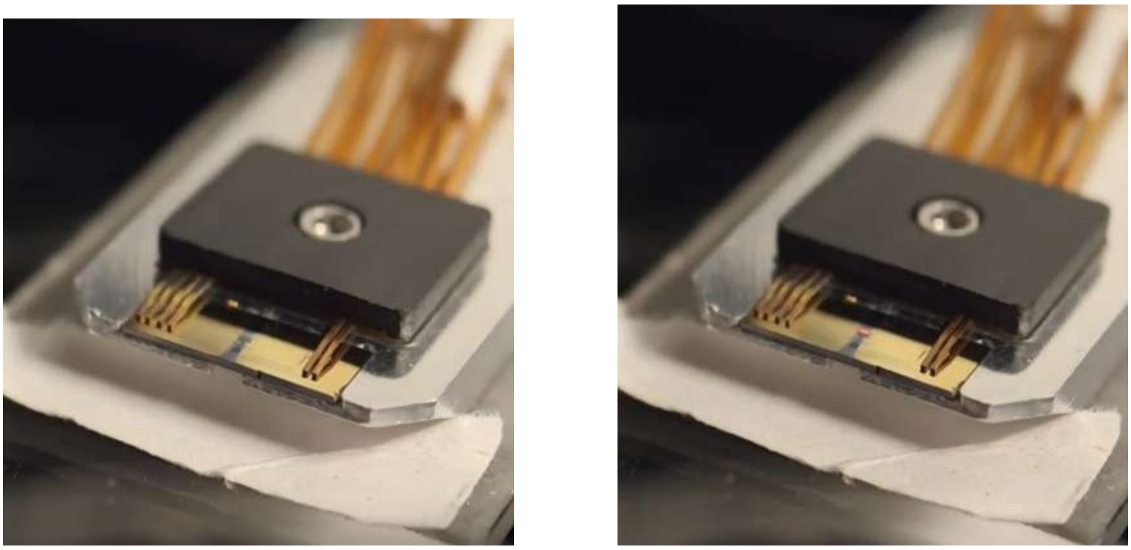

(a) (b)

Figure 3.16: Two images of a gold sputtered JEOL thermal device in a holder on the raman spectroscopy device. Without an applied voltage not much is to be seen, left, but when a voltage is applied the glowing of the wire becomes visible, right. These mechanisms could damage the holder and, while generally they must be avoided at all costs, can only be shown for short durations.

3.2.3. Incomplete Frontside DRIE

During initial tests, the 20 µm devices showed no displacement in response to actuation voltages. Closer inspection revealed residual silicon bridging narrow features of the device, indicating that the frontside DRIE had not etched fully through the device layer in these regions. Imaging from the top surface by SEM proved difficult but allowed them to be barely resolved, see figure 3.17a. Clearer inspection was achieved by imaging through the backside window, see figure 3.17b. To remove these residuals, a subset of chips was subjected to an additional 3 minute DRIE step at an etch rate of 400 nm min^{-1}, the result of which is shown in figure 3.17c. These residuals were not visible through white light interferometry, see Appendix C for these results.

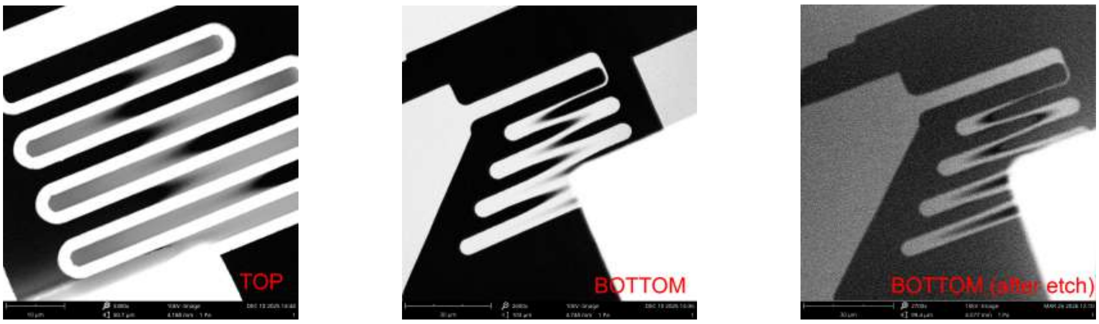

(a) (b) (c)

Figure 3.17: Three SEM images of the same flexure, one as seen from the top and the others from the bottom, showing the residual material connecting and blocking parts of the structures. The rightmost image is taken after additional DRIE etching and shows its ineffectiveness

Large areas of the shuttle are perforated to promote the etching of the oxide, which is otherwise blocked. Now that it is known that the frontside DRIE was insufficient and that most of these holes are not etched through, it is possible that residual oxide structures remain in between the shuttle and structural chip. The shuttles of some devices were destructively removed using double sided tape and a microscope slide to verify this theory, see 3.18.

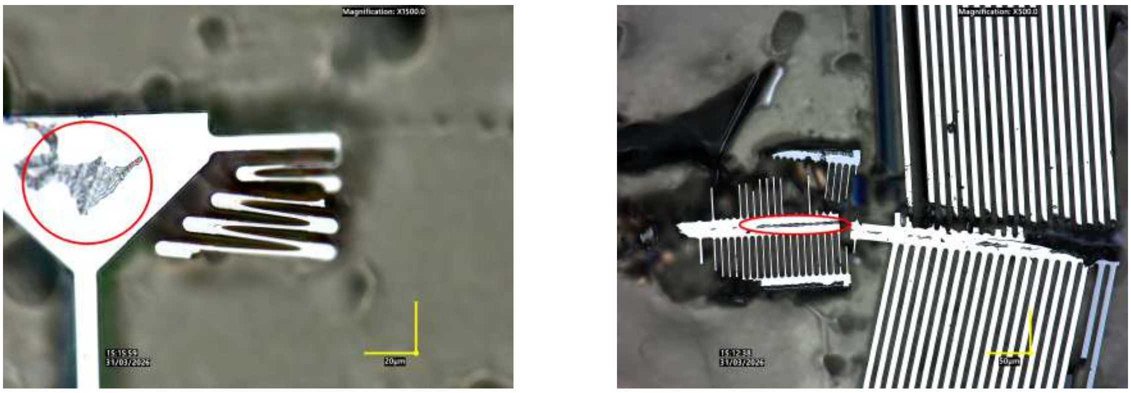

(a) (b)

Figure 3.18: Two VLM images showing leftover silicon dioxide on the bottom of the severed shuttles, highlighted in red, both for the electrostatic (left) and electrothermal device (right). Device layer residuals are visible too in the flexures of the electrostatic device. These images also show the absence of through holes.

These images prove the theory as there clearly are no through holes in the shuttle resulting in leftover silicon dioxide 'glueing' the shuttle and handle silicon together. These remnants are not apparent at the viewing window, which further proves the theory, as, through this viewing window, the oxide was exposed to the vapor HF.

A new mask was created aiming to cover the thermal mechanism while exposing all circuit current paths. This new mask could solve the issue described above. The results of this mask are shown below:

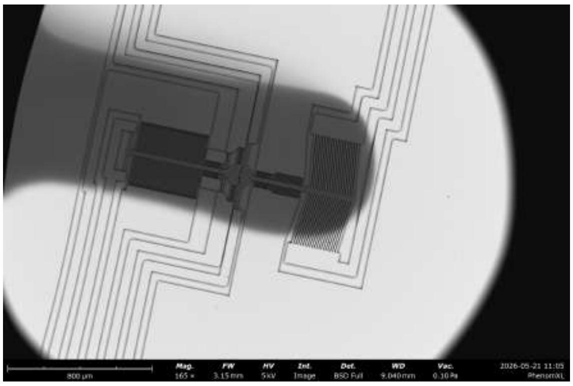

Figure 3.19: Sem image of an electrothermal device after gold sputtering with new mask which exposes all actuation conduction paths. The gold layer appears bright.

3

4
Electrostatic Device

The electrostatic device induces strain through a parallel plate actuator. This device consists of a movable shuttle suspended by four serpentine flexures with a central comb array that functions both as actuator and capacitive sensor. The shuttle displacement is controlled and measured electrostatically through the parallel plates.

These devices were originally designed at Delft University of Technology for quality factor measurements of two-dimensional materials [63]. The original design included a suspended silicon beam underneath the sample for interferometric membrane motion measurements. However, this study focuses on quasi-static strain-stress measurements and omits the beam and includes a through hole to facilitate transmission electron microscopy (TEM) access and simplify the device structure. Figure 4.1 shows a SEM image of the complete electrostatic device.

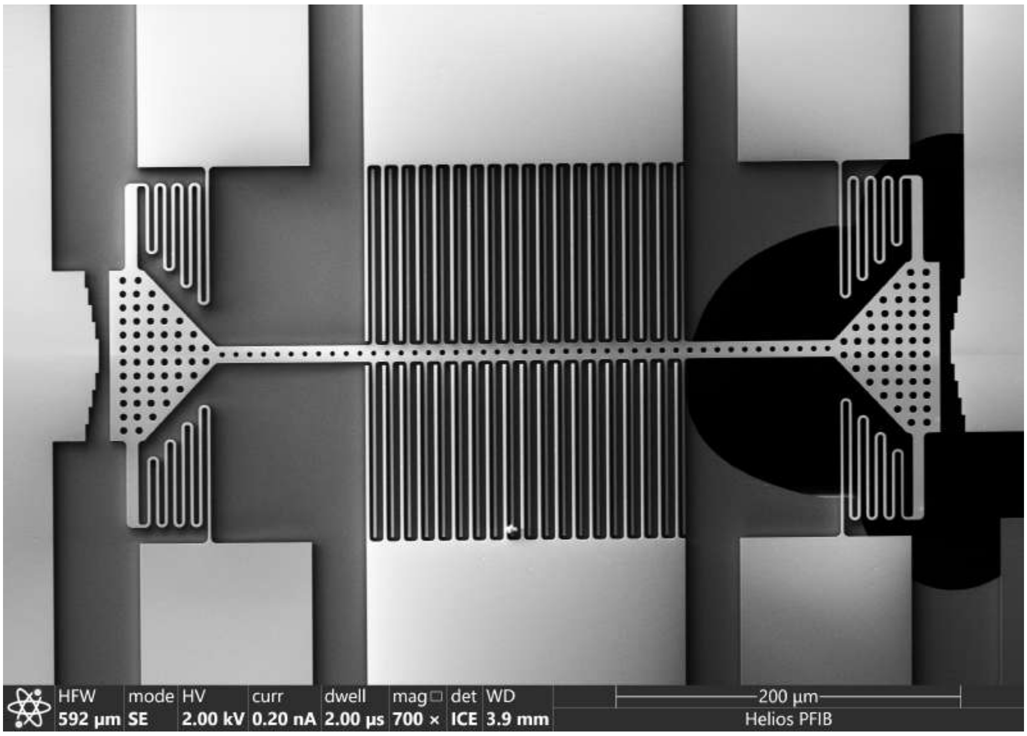

Figure 4.1: SEM image of the electrostatic device

The devices are designed and placed on chips compatible with JEOL and TFS electron microscopy architectures. Actuation, measurement, and biasing solely require 6 contacts. The JEOL holders are wider and allow for up to 8 contact pads, in this case two are thus unused. See figure 4.2 below which shows the actual mask pattern for both versions;

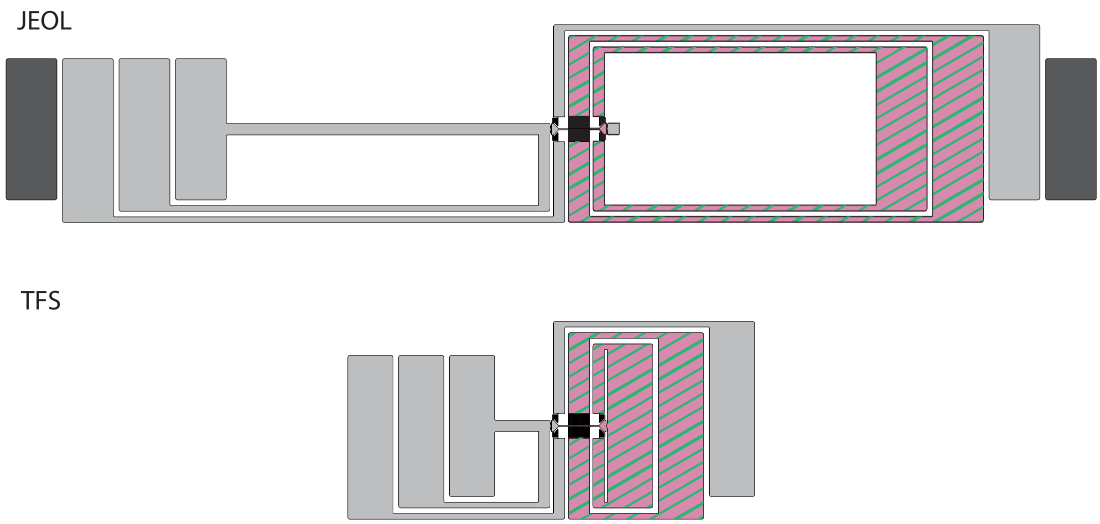

Figure 4.2: Schematic of the chip layout of the electrostatic device for JEOL and TFS compatible systems. The actuation and measurement conduction paths and pads are shown in pink and green. Given the mechanics of the device, both are possible through one circuit and both colors are applied together.

4.1. Theoretical characterization

The theoretical characterization of the electrostatic device initially defines and approaches the individual structural and functional mechanisms composing the complete system analytically. The stiffness of all supporting flexures is derived first, as these values govern the displacement response of the shuttle under actuation. The comb sensor model is then established, relating shuttle displacement to measurable capacitance change through the parallel-plate approximation including a fringe correction factor validated by COMSOL simulations. The actuation force through the central comb follows and the electrostatic force as a function of applied voltage and displacement are derived. The pull-in instability, which defines the maximum stable operating range, is characterized analytically. Breakdown voltage limitations under high-vacuum conditions and fin deformation are then discussed, setting the practical upper bound on actuation force. The section concludes with an analysis of strain measurement sensitivity, which characterizes the achievable strain range and measurement resolution as a function of sample stiffness and actuation voltage.

4.1.1. Stiffness

The mechanical behavior of the electrostatic device is governed by total shuttle stiffness, which includes the sample stiffness and the four serpentine flexures that suspend the shuttle, see figure 4.3 for a simplified representation of the device. All flexures are geometrically identical and therefore contribute equally to the total stiffness.

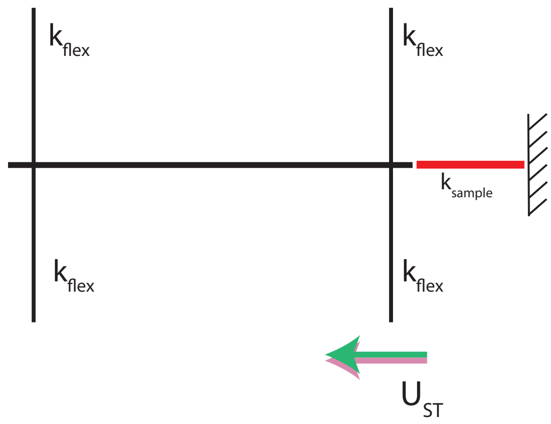

Figure 4.3: Simplified schematic of the device showing the four flexures and the sample with stiffness k_{flex} and k_{sample}. The actuated and measured displacement of the shuttle is shown in pink and green respectively.

The in-plane stiffness must be minimized to reduce the actuation voltage required for a given displacement, while the out-of-plane stiffness must be maximized to constrain the shuttle vertically and prevent contact with the substrate, height misalignment with the support, and sample preparation damage. A lumped mechanical model of the complete device, shown in Figure 4.4, reduces the system to the shuttle mass connected to the support structure through the combined flexure stiffness k_{fl} and to a sample (if present) through the sample stiffness k_s.

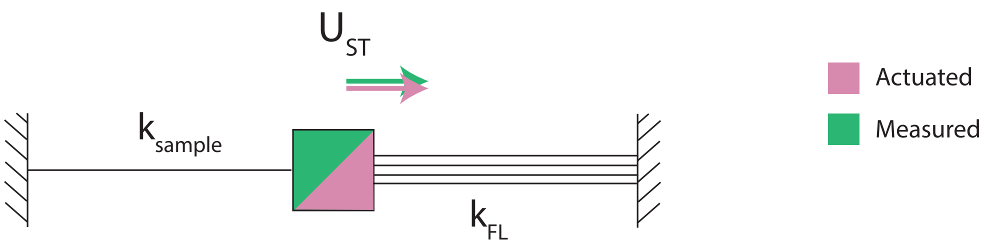

Figure 4.4: Lumped mechanical model of the electrostatic device. The shuttle is suspended by four identical serpentine flexures with combined stiffness $k_{\text{fl}} = 4k_{\text{flex}}$ and connected to a sample of stiffness k_s through the sample mounting points. The shuttle is actuated, pink, and its displacement measured, green, through the same central comb and are thus highlighted together.

Serpentine flexure stiffness Each serpentine flexure consists of eight beam segments of varying length connected by short corner sections, as illustrated in Figure 4.5a. The corner sections are significantly stiffer than the beam segments due to their shorter length and are therefore neglected in the compliance calculation. The flexure is modeled as a series combination of eight cantilever beams, each contributing to the total compliance. The resulting stiffness of a single serpentine flexure is calculated with:

$$k_{\mathrm{flex}} = \frac{12EI}{l_1^3 + l_2^3 + l_3^3 + l_4^3 + l_5^3 + l_6^3 + l_7^3 + l_8^3}, \tag{4.1}$$

where $E = 170\,\mathrm{GPa}$ is Young's modulus of silicon in the $\langle 110 \rangle$ crystal direction, $I = t w_{\mathrm{fl}}^3/12$ is the second moment of area of the beam cross-section for in-plane bending, $w_{\mathrm{fl}} = 2\,\mu\mathrm{m}$ is the flexure width, and t is the device layer thickness ($5\,\mu\mathrm{m}$ or $20\,\mu\mathrm{m}$). The individual beam lengths l_i are listed in Table 4.1 and indicated in Figure 4.5a. The out-of-plane stiffness is calculated using the transposed moment of inertia $I_{\mathrm{oop}} = w_{\mathrm{fl}} t^3/12$, which accounts out of plane deformations; this yields a substantially higher stiffness due to the larger device thickness compared to the flexure width.

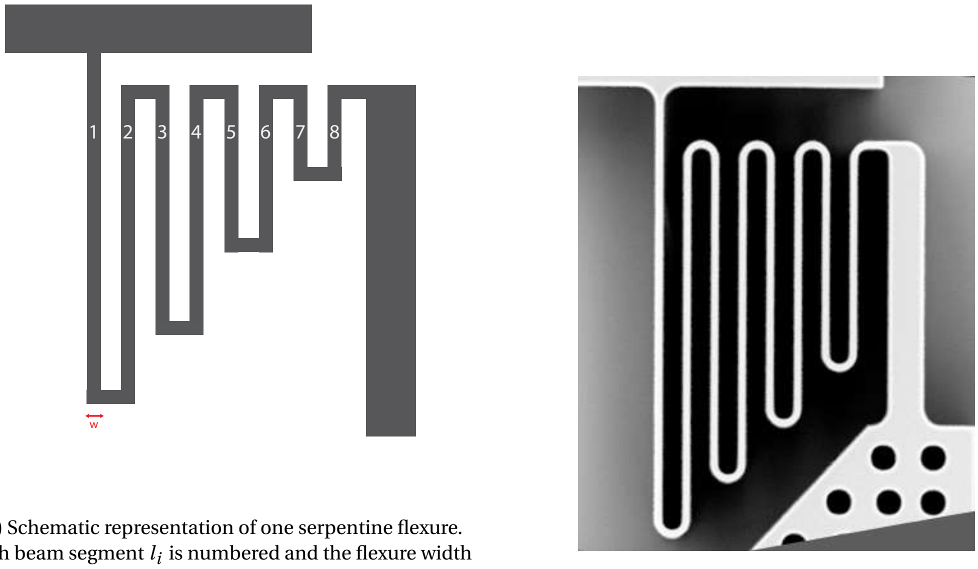

(a) Schematic representation of one serpentine flexure. Each beam segment l_i is numbered and the flexure width w_{fl} is indicated.

(b) SEM image of the serpentine flexure array.

Figure 4.5: Serpentine flexure geometry and SEM image.

	w_{fl}	l_1	l_2	l_3	l_4	l_5	l_6	l_7	l_8
dimension (µm)	2	80	68	58	58	48	48	38	38

Table 4.1: Width and length values of the individual beam segments of serpentine flexure.

Total device stiffness The four flexures and the sample are mechanically in parallel, so the total shuttle stiffness is their sum:

$$k_{\mathrm{fl}} = 4k_{\mathrm{flex}} + k_s. \tag{4.2}$$

The analytical model assumes rigid connections between the flexure legs. In practice, these elements deform slightly under load, reducing the effective stiffness below the predicted value. However, the discrepancy is small: for device layer thicknesses of $5\,\mu\mathrm{m}$ and $20\,\mu\mathrm{m}$, the analytical model yields $k_{\mathrm{fl}} = 16\,\mathrm{N\,m^{-1}}$ and $k_{\mathrm{fl}} = 64\,\mathrm{N\,m^{-1}}$, respectively, while COMSOL force–deflection simulations predict $k_{\mathrm{fl}} = 15\,\mathrm{N\,m^{-1}}$ and $k_{\mathrm{fl}} = 60\,\mathrm{N\,m^{-1}}$.

This agreement validates the analytical approximation and confirms that the neglected compliance contributions are indeed minor. Up until now, in both the analytical and COMSOL approximations, the vertical surfaces of the flexures are assumed to be perfectly flat and smooth. In practice, these vertical features are characterized by scallops resulting from the DRIE Bosch process.

4.1.2. DRIE sidewall corrections

The vertical features of the device layer are etched using the DRIE Bosch process, see Chapter 3. The resulting sidewalls deviate from a vertical smooth geometry in three ways: periodic elliptical scallops along the sidewalls, a mask undercut at the top edge of each feature, and a small inclination angle between the sidewall and the vertical direction, see image 4.6. The first two effectively reduce the width of the flexures and fins, and therefore affect both the bending stiffness from Section 4.1.1 and the overlap area of the comb sensor. The third is unknown for the present device and is assumed minor for the layer thicknesses considered here, and is briefly discussed at the end of this section.

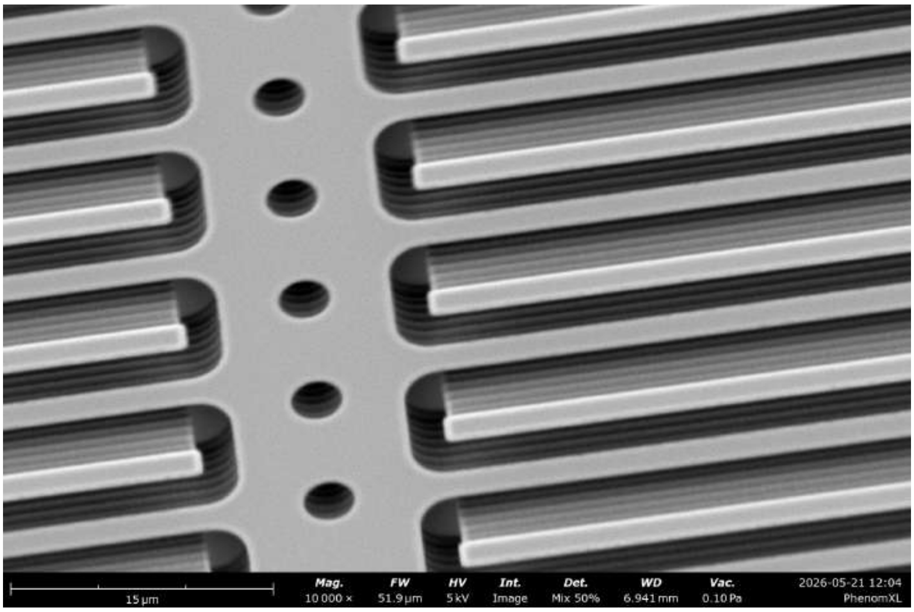

Figure 4.6: SEM image of the capacitive fins of an electrostatic 5 microns device showing the scallops in the vertical features.

Scallops The vertical features of the device layer where etched using the DRIE Bosch process, see the production chapter 3. The scallops, which are trenches modeled as ellipses (see equation 4.3 from [64]) with depth, b, and height, $2a$, which decrease the effective flexure width, further decreasing the in plane bending stiffness, shown schematically in figure 4.7 below.

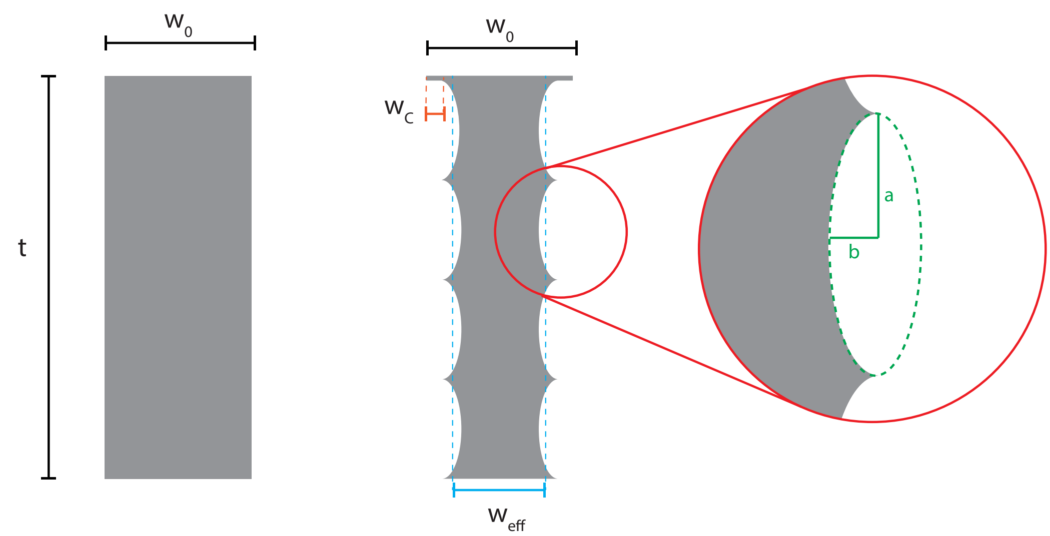

Figure 4.7: Scallop and mask-undercut schematic. The scallop is modeled as an ellipse of depth b and pitch $2a$, where $2a$ equals the etched depth per Bosch cycle. The mask undercut w_C reduces the initial beam width w_0 by $2w_C$ before the scallop correction is applied. On the left a perfectly smooth vertical structure is shown with on the right the effective structure made with DRIE.

Each DRIE cycle etched to a depth of 1 µm, and thus, $2a = 1\mu\text{m}$. From literature, values for scallops with comparable height values depth range from $100 \leq b \leq 300$ nm [64], [65], [66]. From now, lacking formal measurements, the value of this depth, b, is set as 150 nm.

$$w(z) = w_0 - 2b\sqrt{1 - \left(\frac{z-a}{a}\right)^2} \tag{4.3}$$

Mask undercut In addition to the scalloped sidewalls, the DRIE Bosch process produces a small lateral undercut beneath the hard mask. This effect decreases the fin and flexure width w_0 by $2w_C$, where w_C is the undercut per side, see figure 4.7. The exact value of w_C depends on the etch recipe, chamber pressure, passivation timing, and mask material, and varies between tens and hundreds of nanometres per side [66], [67]. For SiO_2 hard masks under optimized Bosch recipes, w_C is at the lower end of this range. Lacking direct measurements, a value of $w_C = 50\,\text{nm}$ per side is adopted here, consistent with optimized SiO_2-mask Bosch processes. This reduces the initial beam width from $w_0 = 2\mu\text{m}$ to $w_0' = w_0 - 2w_C = 1.9\mu\text{m}$ before the scallop correction is applied.

Effective beam width An effective beam width, w_{eff}, is introduced as to include the effect these scallops have on the bending stiffness. This is done by equating the in plane area moment of inertia for a beam with w_{eff}, I_{eff}, to the area moment of inertia of a beam including the elliptical scallops, I_{sc}.

$$I_{\text{sc}} = \int_0^t \frac{w(z)^3}{12} dz \tag{4.4}$$

$$I_{\text{eff}} = \frac{t w_{\text{eff}}^3}{12} \tag{4.5}$$

with $0 \geq z \geq t$, t being the beam thickness and $w_0' = w_0 - 2w_C = 1.9\,\mu\text{m}$ the initial beam width including the mask undercut correction. By substituting $u = \frac{z-a}{a}$ (and $(t = \frac{t}{2a}2a)$) in equation 4.4 and combining with equation 4.5:

$$\frac{t w_{\text{eff}}^3}{12} = \frac{t}{2a}\int_{-1}^{1} \frac{\left(w_0' - 2b\sqrt{1-u^2}\right)^3}{12} a\,du \tag{4.6}$$

Which simplifies to:

$$w_{\text{eff}}^3 = \frac{1}{2}\int_{-1}^{1} \left(w_0' - 2bs\right)^3 du \tag{4.7}$$

with $s = \sqrt{1-u^2}$. Working this out for the effective beam width, w_{eff}, this boils down to:

$$w_{\text{eff}}^3 = w_0'^3 - \frac{3\pi}{2} w_0'^2 b + 8 w_0' b^2 - \frac{3\pi}{2} b^3 \tag{4.8}$$

For $b = 150\,\text{nm}$ and $w_C = 50\,\text{nm}$, an effective flexure beam width of $w_{\text{eff}} = 1.67\,\mu\text{m}$ follows. Using this value, shuttle stiffnesses of 10,18 and 40,7 $\text{N}\,\text{m}^{-1}$ for the 5 and 20 µm devices are calculated respectively.

4

Effect on capacitance The DRIE scallops introduced above also affect the comb sensor capacitance. The scalloped sidewalls slightly increase the distance between opposing fins, decreasing the parallel-plate capacitance compared to a smooth-wall reference. Pawar et al. [64] showed that going from no scallops ($b = 0$) to $b = 150\,\text{nm}$ decreases the electrostatic force by approximately 7%, and that the number of scallops along the fin height does not influence this result, only their presence and depth do. While Pawar's analysis uses a linear comb drive geometry, the underlying mechanism, namely the periodic scallops reducing the effective capacitance, still apply here. Using the same scallop depth $b = 150\,\text{nm}$ and pitch $2a = 1\,\mu\text{m}$ adopted above, the corresponding capacitance correction is expected to be on the order of 5–10%.

Inclination angle Sidewalls are not perfectly vertical and in this study, its angle deviation is unknown, which would affect the local capacitance and electrostatic force. This difference increases with device thickness. The effect is excluded from the present model because the angle is not measured and its effect is assumed to be minimal, and is left for future work.

4.1.3. Comb sensor

When the shuttle translates parallel to the actuation axis, the distance between the movable (shuttle) and fixed (stator) comb fins changes, producing a measurable capacitance variation which can then be measured. In theory, all forces, both the electrostatic actuation force and the sample reaction force, act parallel to the shuttle axis by design. The capacitance change therefore arises from pure unidirectional in-plane translation, with no lateral or out-of-plane motion components. The comb sensor thus provides a direct readout of shuttle position along the actuation axis.

Parallel-plate capacitance model The comb geometry is simplified to a series of parallel-plate capacitors. Figure 4.8 shows the simplified configuration: each fin on the shuttle is positioned between two fins on the stator, creating two capacitive gaps per fin pair. One gap closes as the shuttle advances (the "close gap," initial width d_{10}), while the opposite gap opens (the "far gap," initial width d_{20}). The capacitance between two parallel plates separated by distance d with overlapping area A_o is:

$$C = \frac{\epsilon_0 A_o}{d}, \tag{4.9}$$

where $\epsilon_0 = 8.854 \times 10^{-12}\,\mathrm{F\,m^{-1}}$ is the permittivity of free space. For a shuttle displacement x in the positive actuation direction, the two gap distances become:

$$d_1(x) = d_{10} - x, \tag{4.10}$$

$$d_2(x) = d_{20} + x. \tag{4.11}$$

The two capacitance formed by each fin are electrically in parallel, so their capacitances add. The structure is mirrored on both sides of the shuttle, and the comb array contains n fin pairs, giving a total capacitance of:

$$C_{\mathrm{tot}}(x) = 2n\left(C_1(x) + C_2(x)\right) = 2n\epsilon_0 A_o \left(\frac{1}{d_{10} - x} + \frac{1}{d_{20} + x}\right). \tag{4.12}$$

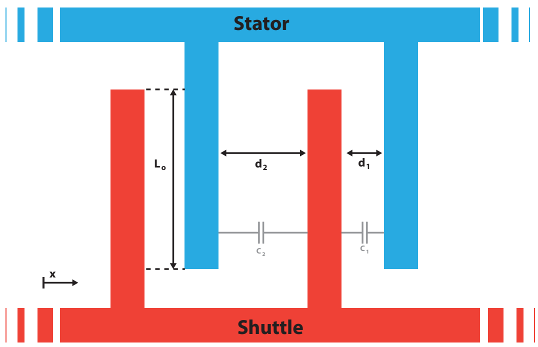

Figure 4.8: Simplified schematic of the interdigitated comb sensor. The shuttle (red) translates in the positive x-direction relative to the stator (blue). Each fin creates two capacitive gaps: C_1 (close gap, $d_{10} - x$) and C_2 (far gap, $d_{20} + x$). The structure is mirrored symmetrically about the shuttle centerline.

Fringe field correction Equation (4.12) assumes an ideal parallel-plate configuration with a uniform electric field confined to the overlapping region. In practice, the electric field extends beyond the plate edges, creating fringe fields that increase the effective capacitance. This effect is particularly pronounced when the gap spacing is comparable to or smaller than the fin dimensions, as is the case here. Multiple analytical approximations for fringe capacitance exist, including Palmer's formula [68] and Nemirovsky's square-plate approximation [69], but these require geometric parameters that are difficult to find accurately from the present device layout. A simpler empirical approach is adopted instead.

COMSOL electrostatic simulations are performed for both device thicknesses (5 µm and 20 µm) over the full displacement range. Two simulation cases are run for each configuration: one allowing electrical fields to extend beyond the overlapping fin area, and one with artificial boundary conditions that suppress fringe effects by confining the field to only the overlapping region. The analytical parallel-plate formula (4.12) is compared against both simulation results, as shown in Figure 4.10. The no-fringe simulation agrees almost perfectly with the analytical prediction, confirming the validity of the parallel-plate approximation when fringe effects are excluded. The full simulation, which includes fringe fields, yields systematically higher capacitance values, as expected.

A fringe correction factor f is defined as the ratio of the fringe-inclusive capacitance to the parallel-plate capacitance. While f varies slightly with displacement, it remains approximately constant over the limited actuation range considered here (<1 µm), see section 4.1.5 regarding the pull-in condition defining the actuation range. The corrected total capacitance is therefore:

$$C_{\text{tot}}(x) = 2nf\epsilon_0 A_o \left(\frac{1}{d_{10} - x} + \frac{1}{d_{20} + x} \right), \tag{4.13}$$

4

where f is extracted by averaging the ratio $C_{\text{full,sim}}/C_{\text{analytical}}$ over the working displacement range, see figure 4.10. The fringe factor depends heavily on the device layer thickness: thinner devices, 5 µm, exhibit a larger relative fringe contribution because their smaller nominal capacitance makes the edge fields more significant, as compared to the 20 µm thick devices. Figure 4.9 shows the variation in fringe factor across the displacement range for both device thicknesses.

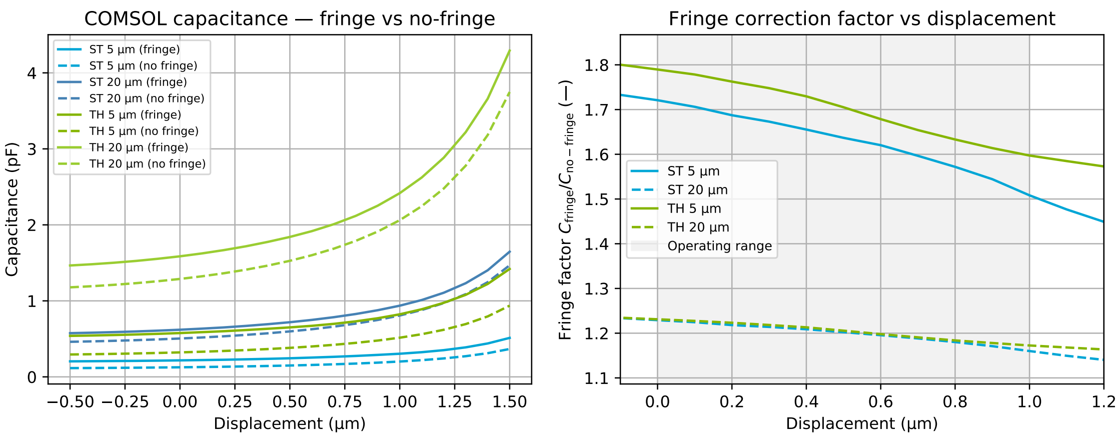

Figure 4.9: Plot of the COMSOL simulation with and without the fringe difference, left, and their respective fringe factors, right. These results are for both the electrostatic and electrothermal comb structures.

The corrected analytical model (4.13) is compared against the simulation in Figure 4.10 and shows good agreement, validating the constant-fringe-factor approximation over the working range.

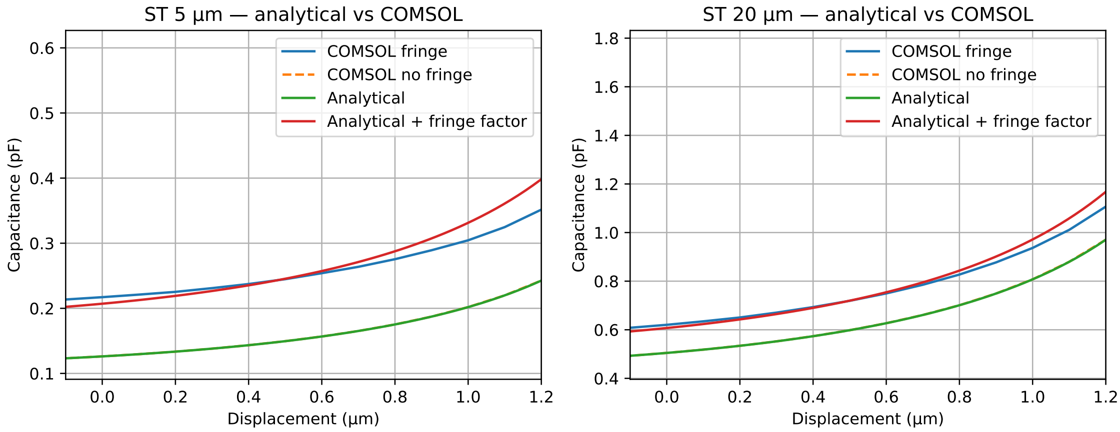

Figure 4.10: Capacitance versus displacement for the 5 µm (left) and 20 µm (right) devices. The analytical parallel-plate formula (dashed orange), not including fringes, matches the no-fringe COMSOL simulation (green) closely. The full simulation including fringe fields (blue) shows the expected capacitance increase due to edge effects. The analytical model corrected with a constant fringe factor f (red) approximates the full simulation well over the limited displacement range.

4.1.4. Eigenfrequencies

Measurement error and undesired resonant actuation can occur when the excitation frequency approaches an eigenfrequency of the device. Using COMSOL, the six most prominent eigenfrequency modes are identified and visualized in Figure 4.11 for both device thicknesses.

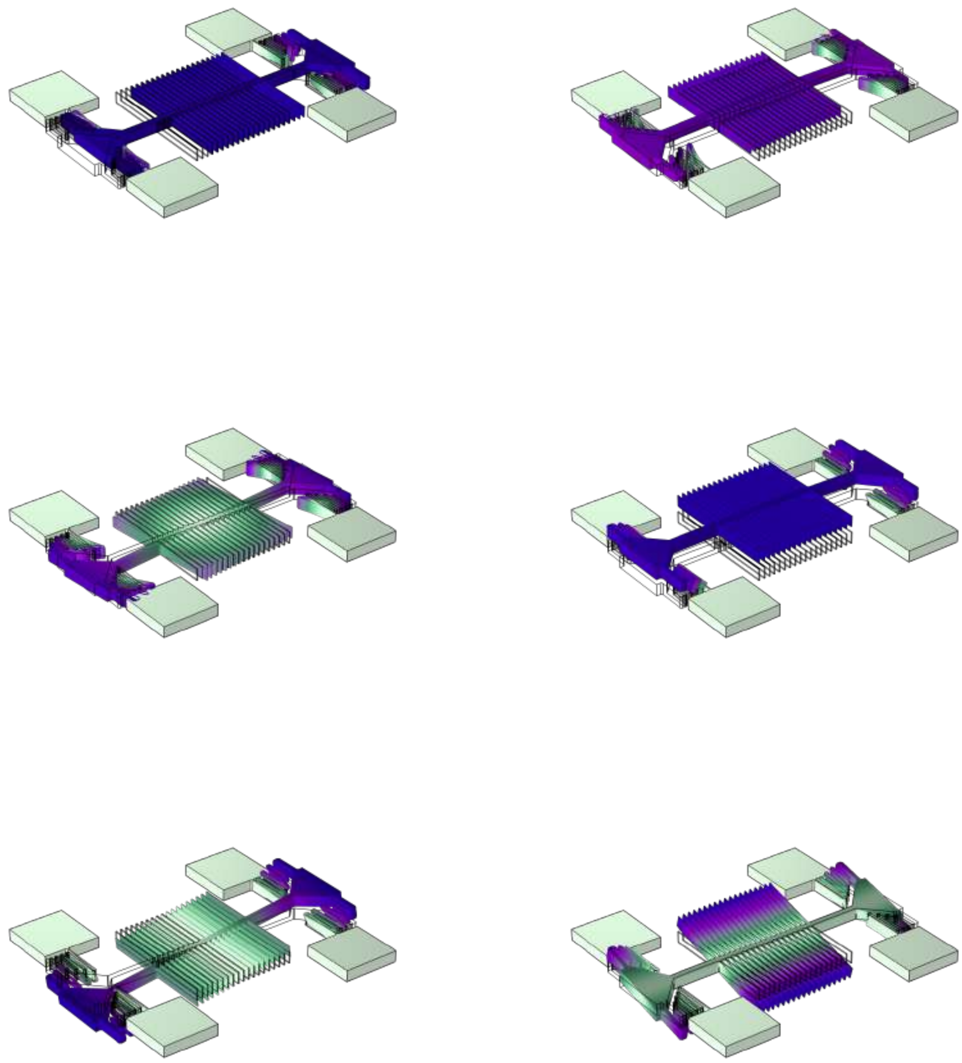

Figure 4.11: Eigenfrequency mode shapes for the 20 μm device: modes 1 and 2, top, 3 and 4, middle, and 5 and 6, bottom.

The first mode is an in-plane vibration along the actuation axis and is therefore the mode most susceptible to excitation during measurements. The eigenfrequency values for all six primary modes are listed in Table 4.2 for both device thicknesses.

Device	Mode 1	Mode 2	Mode 3	Mode 4	Mode 5	Mode 6
20 μm	38.4	59.3	68.0	70.0	86.5	124
5 μm	37.9	58.7	67.4	43.4	61.6	74.3

Table 4.2: Eigenfrequencies of the 20 μm and 5 μm devices. All values in kHz.

The first three modes are purely in-plane for both devices. Because the in-plane stiffness and shuttle mass both scale linearly with thickness, the ratio $\sqrt{k/m}$ is approximately unchanged, and the two devices yield nearly identical in-plane eigenfrequencies. The out-of-plane bending stiffness, however, scales with t^3 through the area moment of inertia, while the mass scales only with t; which explains why modes 4–6 of the 5 µm device are considerably lower than their 20 µm counterparts. Operating above 150 kHz ensures a safe margin from all identified resonances.

4.1.5. Comb drive

The same central comb through which the shuttle displacement is measured generates the electrostatic actuation force that displaces it. By applying a potential over the movable (shuttle) and fixed (stator) fins, charge accumulates on the opposing surfaces and produces an attractive force. This force can be derived from energy considerations: the electrostatic energy stored in the capacitor varies with displacement, and the force is obtained as the negative gradient of this energy with respect to position. The equilibrium displacement is determined by the balance between the electrostatic force and the mechanical reaction force of the flexures and sample. Three limiting factors are worked out to define the operational range: the pull-in instability, which occurs when the electrostatic force gradient exceeds the mechanical stiffness; the breakdown voltage, which sets the maximum field strength before electrical discharge; and the fin-bending contact limit, which sets the maximum voltage at which the stator fins bend and just avoid contact with the shuttle fins. Leakage currents through the dielectric are also briefly discussed, but their magnitude is negligible at all operating voltages.

4

Electrostatic force The electrostatic energy stored in a capacitor is $E_{st} = C(x)V^2/2$, where $C(x)$ is the displacement-dependent capacitance from (4.13) and V is the applied voltage. The force exerted on the shuttle is the negative derivative of this energy with respect to displacement:

$$F_{st} = \frac{\partial E_{st}}{\partial x} = \frac{V^2}{2}\frac{\partial C(x)}{\partial x}. \tag{4.14}$$

Substituting the total capacitance (4.13) and evaluating the derivative yields:

$$F_{st} = nf\epsilon_0 A_o V^2 \left[\frac{1}{(d_{10}-x)^2} - \frac{1}{(d_{20}+x)^2}\right]. \tag{4.15}$$

The force is attractive and increases nonlinearly with displacement: as the close gap narrows, the field strengthens and the force increases rapidly. This nonlinearity is the origin of the pull-in instability discussed below.

Force equilibrium At equilibrium, the electrostatic force F_e equals the mechanical force from the flexures and the sample:

$$F_{st}(x,V) = (k_{\text{fl}} + k_s)x, \tag{4.16}$$

where k_{fl} is the total flexure stiffness from (4.2) and k_s is the sample stiffness. If the shuttle displacement x is measured independently (e.g., through TEM imaging or comb sensor capacitance measurements) and the applied voltage V is known, the sample stiffness can be calculated by rearranging (4.16):

$$k_s = \frac{F_{st}(x,V)}{x} - k_{\text{fl}}. \tag{4.17}$$

This expression is valid only within the stable operating range, before pull-in occurs. At high actuation forces, the comb fins may deform elastically, introducing a displacement-dependent error in both the measured x and the effective capacitance. This effect is neglected with regards to the force equilibrium.

Pull-in instability The pull-in point limits the maximum stable displacement of the shuttle. Beyond this point, the system becomes mechanically unstable: the shuttle accelerates toward the stator, and the fins snap together. This instability arises as the electrostatic force increases faster with displacement than the linear mechanical restoring force. The pull-in condition is found by equating the rate of change of the electrostatic force to the mechanical stiffness:

$$\frac{\partial F_{st}}{\partial x} = k_{\text{fl}} + k_s. \tag{4.18}$$

Differentiating (4.15) and equating to the total stiffness yields:

$$2nf\epsilon_0 A_o V^2 \left[\frac{2}{(d_{10}-x)^3} + \frac{2}{(d_{20}+x)^3}\right] = k_{\text{fl}} + k_s. \tag{4.19}$$

At the pull-in point, both the force equilibrium (4.16) and the instability condition (4.18) must hold simultaneously. Dividing (4.16) by (4.19) eliminates the voltage, stiffness, and material parameters, leaving a purely geometric relation:

$$x_{\text{pull-in}} = \frac{1}{2}\frac{(d_{10}-x)^{-2} - (d_{20}+x)^{-2}}{(d_{10}-x)^{-3} + (d_{20}+x)^{-3}}. \tag{4.20}$$

This equation is solved numerically for $x_{\text{pull-in}}$ given the initial gap spacings d_{10} and d_{20}. Remarkably, this pull-in condition, equation (4.20), is independent from all system parameters except the initial gap geometry: the pull-in displacement is the same regardless of the number of fin pairs n, the permittivity ϵ_0, the overlapping area A_o, the fringe factor f, the total stiffness $k_{\text{fl}} + k_s$, or the applied voltage V. This universality holds only for samples with constant stiffness; for nonlinear or displacement-dependent sample stiffness, (4.20) no longer applies.

For the present device geometry with $d_{10} = 2\,\mu\text{m}$ and $d_{20} = 4\,\mu\text{m}$, the pull-in displacement is $x_{\text{pull-in}} = 0.61\,\mu\text{m}$ for both the 5 µm and 20 µm devices. Given an initial sample gauge length equal to the gap size (6 µm), this corresponds to a maximum achievable strain of approximately 10 %. Figure 4.12 illustrates the pull-in condition graphically:

the electrostatic and mechanical forces are plotted as functions of displacement, and the pull-in point occurs where the shuttle displacement increases for lower voltages.

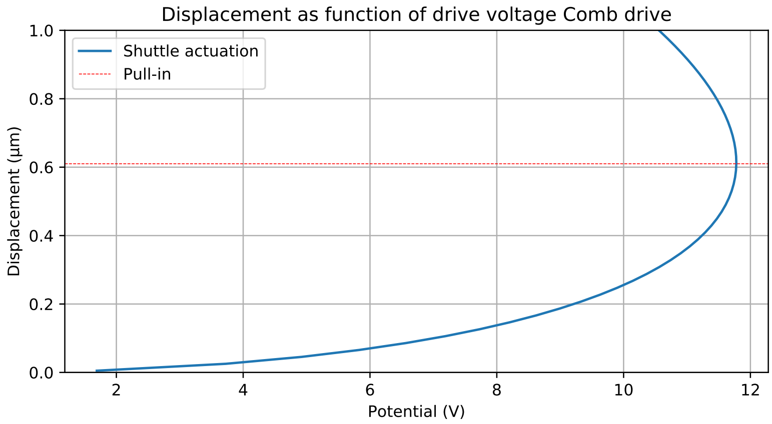

Figure 4.12: An example of the shuttle displacement relating to the actuation voltage where, at the pull-in condition, an instability shows. The pull-in displacement is highlighted is red.

However, this condition only holds true for samples with linear stress-strain characteristics. A softening sample would decrease the maximal stable displacement while a hardening sample would increase this range. For nonlinear samples, the sample stiffness becomes displacement-dependent and no longer cancels when dividing (4.16) by (4.19).

Fin deformation The pull-in and breakdown voltage limits assume that all comb fins remain rigid and straight. In reality, the electrostatic force between two opposing fins pulls each fin sideways. As the actuation voltage increases, individual fins bend toward their closest neighbor, eventually reaching contact.

Each fin is modeled as a clamped cantilever beam of length L_{fin}, in-plane width w_{fin}, and out-of-plane thickness equal to the device layer thickness t. At a shuttle displacement x, the close-side gap is $d_{10}-x$ and the far-side gap is $d_{20}+x$, so the net rigid-fin electrostatic load per unit length pulling the fin toward the close stator fin is:

$$q_{\text{rigid}}(x, V) = \frac{\epsilon_0 V^2 t}{2}\left[\frac{1}{(d_{10}-x)^2} - \frac{1}{(d_{20}+x)^2}\right]. \tag{4.21}$$

A uniformly distributed load along the fin underestimates the deflection: as the fin bends, the gap closer to the fin tip closes, and the electrostatic force redistributes toward the tip [41]. A point load at the tip overestimates the deflection. A linearly increasing load distribution, zero at the base and maximum at the tip, captures the redistribution effect without solving the fully coupled electromechanical problem:

$$q(z) = q_{\text{tip}} \cdot \frac{y}{L_{\text{fin}}}, \tag{4.22}$$

where y is the coordinate along the fin length. The tip deflection of a clamped cantilever under this linearly increasing load is:

$$\delta_{\text{tip}} = \frac{11 q_{\text{tip}} L_{\text{fin}}^4}{120 E I_{\text{fin}}}, \qquad I_{\text{fin}} = \frac{t w_{\text{fin}}^3}{12}. \tag{4.23}$$

Contact between the deformed fin and the closer stator fin occurs when $\delta_{\text{tip}} = d_{10} - x$. Substituting (4.21) and (4.23) and solving for V gives the fin-bending contact-limit voltage:

$$V_{\text{finbend}}(x) = \sqrt{\frac{20\, E\, w_{\text{fin}}^3 (d_{10} - x)}{11\, \epsilon_0\, L_{\text{fin}}^4 \left[(d_{10} - x)^{-2} - (d_{20} + x)^{-2}\right]}}. \tag{4.24}$$

4

The device layer thickness t appears in both q_{rigid} and I_{fin} and therefore cancels: V_{finbend} is the same for the 5 µm and 20 µm devices, given identical in-plane geometry. With the present fin dimensions ($L_{\text{fin}} = 100$ µm, $w_{\text{fin}} = 1.67$ µm, accounting for scallop and mask undercut corrections from Section 4.1.1), V_{finbend} ranges from approximately 143 V at $x = 0$ to 75 V at $x = x_{\text{pull-in}}$. Figure 4.13 shows the fin-bending geometry, and the resulting voltage limit is incorporated into the voltage-displacement operating map in the following paragraph.

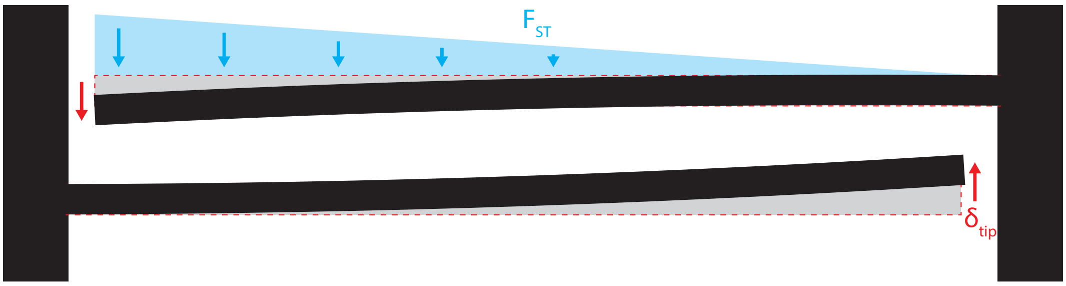

Figure 4.13: schematic of fin bending under electrostatic load, showing the linearly increasing load distribution along the fin and the resulting tip deflection δ_{tip}.

The linear-ramp model is itself an approximation. In reality, both fins bend towards eachother and the force distribution changes from uniform, under low actuation force, to concentrated towards the sides as the force is highest where the fin (tips) are closest to eachother. The fin tip of the other fin would increase the force at the base of the one in question. The proposed model overestimates the fin tip deflection as it overestimates the force distribution towards the fin tips. A fully self-consistent treatment of the coupled electromechanical problem is given by Legtenberg et al. [41] using an energy-based assumed-shape method. The simplification is retained because (i) the present model is intended as a design constraint rather than a precise representation, (ii) the dominant effect, fin bending lowers the safe voltage well below the breakdown limit, is captured, and (iii) the impact of fin bending on the comb capacitance is not included either, which would further shift both the equilibrium displacement and the contact voltage. A complete coupled analysis is left for future work.

Breakdown voltage Rearranging the force equilibrium (4.16) to express voltage as a function of displacement and sample force yields:

$$V(x, F_{st}) = \sqrt{\frac{2(k_{\text{fl}}x + F_{st})}{f\epsilon_0 A_o \left[\frac{1}{(d_{10}-x)^2} - \frac{1}{(d_{20}+x)^2}\right]}}. \tag{4.25}$$

While (4.25) suggests that arbitrarily large sample stresses can be achieved by increasing the applied voltage, two upper limits exist: the fin-bending contact limit derived above, and the electrical breakdown voltage discussed here. Above the breakdown threshold, in ambient environments, the electric field between the fins is strong enough to ionize residual gas molecules or initiate field emission from surface asperities, resulting in a discharge that can damage or destroy the device.

4

In high vacuum, the breakdown mechanism still persists but differs fundamentally from the Paschen breakdown observed at ambient pressure. Under vacuum conditions, gas ionization is suppressed, and breakdown is instead governed by field emission from (microscopic) protrusions on the fin surfaces. Fowler-Nordheim emission becomes the dominant mechanism: electrons tunnel from sharp features on the cathode surface when the local field exceeds approximately $10^9\,\mathrm{V\,m^{-1}}$ [70]. The emitted electrons are accelerated across the gap and can trigger localized heating, desorption of adsorbed gas, and ultimately a micro-arc that shorts the device.

The breakdown voltage in vacuum depends on the gap spacing and surface roughness. Experimental studies have shown that for gaps in the range 20 nm to 300 nm, the breakdown voltage scales approximately linearly with gap [71]. For gaps between 0.3 µm to 1 µm, a power-law relationship is observed [72]. At gaps exceeding 1 µm, the breakdown voltage plateaus at a nearly constant value [73], likely because field emission from the largest protrusions begins to dominate over the average gap-dependent field. Given that the minimum gap in the present device exceeds 1 µm (the close gap spacing at the pull-in point, $d_{10} - x_{\text{pull-in}}$, including a safety margin for strain-stiffening samples and fin deformation), a conservative breakdown voltage of 180 to 200 volts applies to the undeformed geometry.

This nominal breakdown voltage lies above the fin-bending contact limit of (4.24) (75 V to 143 V over the actuation range). For the rigid, undeformed gaps, the fins therefore bend into contact before the breakdown field is reached across the nominal gap, so fin deformation rather than breakdown sets the operating ceiling. The two limits are not independent near contact, however. As a fin bends, the local gap at its tip closes and the local field there rises sharply, so field emission sets in across the narrowing gap shortly before mechanical contact is made; the breakdown and contact voltages effectively converge in this regime. Resolving the exact combined limit would require the coupled fin-deflection and field model together with a measured surface field-enhancement factor, and is left to future work. For design purposes, both the fin-bending limit and the nominal breakdown voltage are treated as conservative ceilings that are not approached during operation.

Voltage-displacement operating map Now, all the above is brought together to define a working regime linked to the sample stiffness, meaning; voltage range, force range and displacement. Stiff samples are expected to require a higher voltage to achieve the same strain as a ductile sample. Given the increased overlapping fin area, the thick devices are expected to require lower voltages to achieve the same strain with the same sample on the thin devices. Figure 4.14 presents the complete voltage-displacement characteristic for both device thicknesses, incorporating all operational limits.

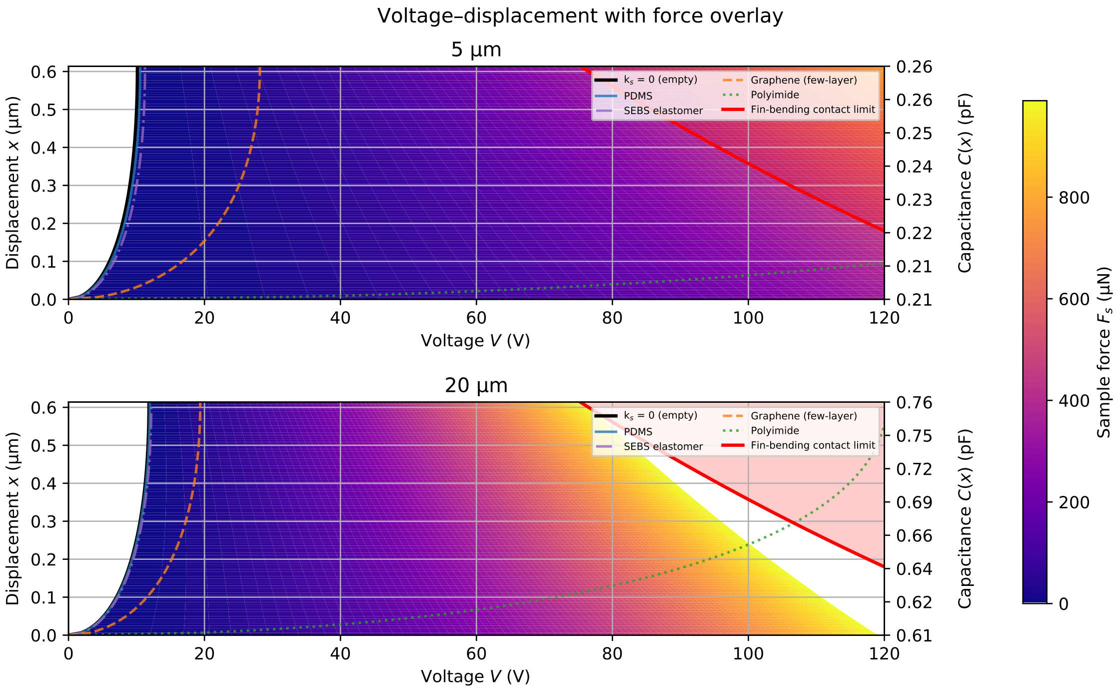

Figure 4.14: Voltage-displacement operating map for the 5 µm (top) and 20 µm (bottom) devices. Some example sample stiffnesses are included to visualise the achieveable strain and force regime. The fin-bending contact-limit voltage from (4.24) is shown as a red curve; the shaded region to its right shows operating points beyond where the deformed shuttle fins would contact the opposing stator fins.

The 20 µm device offers a substantially higher force range, roughly fourfold, compared to the 5 µm device due to its greater capacitance (scaling with layer thickness). The 5 µm device is severely limited: achieving even moderate forces requires voltages approaching the fin-bending contact limit, and stiff samples cannot be strained significantly before reaching this limit. The leakage current through the dielectric (vacuum) is expected to remain in the picoampere to low nanoampere range at all operating voltages, so Joule heating of the device is negligible and does not impose an additional constraint, see Appendix E.

4.1.6. Stiction

Two stiction modes are possible: fins coming into contact (Figure 4.15a), and the shuttle sticking to the substrate (Figure 4.15b). Fin stiction happens when the device passes the pull-in point during testing or when the shuttle is bumped/ moved, bringing opposing fins close enough for surface forces to take over. Shuttle stiction can occur from rough handling during sample preparation or from electrostatic charging.

At the microscale, van der Waals forces become significant. For two parallel surfaces separated by distance d_0, the attraction force follows the Hamaker relation, derived in 1937 [74]:

$$F_{\text{vdW}} = \frac{A_H A_c}{6\pi d_0^3} \tag{4.26}$$

where A_H is the Hamaker constant, A_c is the contact area, and d_0 is the surface separation (for silicon in vacuum, $A_H \approx 2 \times 10^{-19}\,\text{J}$ [75](chapter 13, p263)). The problem with (4.26) is that it diverges as $d_0 \to 0$: the force goes to infinity when surfaces touch, which is impossible. For atomically smooth hard surfaces in contact, the equilibrium separation is taken as $d_0 \approx 0.165\,\text{nm}$ [75](chapter 13, p280). This cutoff prevents the divergence, but still predicts unrealistically large adhesion forces for real MEMS structures as it assumes perfectly smooth surfaces.

The DRIE process produces characteristic scalloping on the vertical sidewalls from the alternating etch and passivation cycles. The scallop size depends on trench width and depth: narrow trenches show reduced scalloping at high aspect ratios due to radical transport limitations, an effect called aspect-ratio-dependent scalloping attenuation (ARDSA) [76]. Chabloz et al. measured sidewall roughness for 2 µm wide trenches etched to 40 µm depth and found RMS roughness of 33 nm at the top surface decreasing to 10 nm at the trench midpoint [77]. For the 1 µm fin scallops in this device with 5 µm etch depth (aspect ratio 5:1), the fin sidewall roughness is estimated at 30 nm to 40 nm RMS near the top and 10 nm to 20 nm deeper down [78]. The shuttle bottom surface and substrate top surface are released by vapor HF rather than DRIE, and expose the silicon layers with a roughness of typically 0.2 nm RMS [79].

Rabinovich et al. developed a model for adhesion between rough surfaces [80]. The key idea is that surface roughness increases the effective separation distance in contact:

$$d_{\text{eff}} = d_0 + 1.48 \cdot \text{RMS} \tag{4.27}$$

This d_{eff} replaces d_0 in (4.26) for the force calculation. For fin sidewalls with RMS $\approx 30\,\text{nm}$, the effective separation becomes $d_{\text{eff}} \approx 44\,\text{nm}$, reducing the adhesion force by a factor of $(d_{\text{eff}}/d_0)^3 \approx 17\,000$ compared to the smooth-surface prediction.

For fin-to-fin stiction, the effective contact area is limited by roughness to a small fraction of the nominal overlap. Taking a conservative contact area of $15\,000\,\mu\text{m}^2$ and RMS = 20 nm, (4.26) with d_{eff} from (4.27) gives an adhesion force of approximately 5.7 µN and 23 µN for the 5 and 20 micron thick devices. The restoring force from a single flexure at 2 µm deflection is roughly 32 µN and 126 µN, so it seems the van der waals forces are overcorrected and no, stable, fin stiction would be possible.

This effect has only been seen with the 5 µm thick devices, the 20 µm weren't functional yet. It can be hypothesized that the shuttle slightly shifts in the z-direction for the fins to have better surface contact with eachother increasing the van der waals forces. According to this theory, fin stiction would not be possible for the thick devices as teh out of plane stiffness is many times larger. Furthermore, during testing, it was relatively easy to dislodge the shuttle by gently blowing compressed air on the device or gently tapping the device on a table.

For shuttle-to-handlewafer stiction, the contact area includes the shuttle and support structures: approximately 12 000 µm^2. Using the lower roughness estimate for vapor-HF surfaces (RMS ≈ 20 nm), the effective separation is $d_{\text{eff}} \approx 0.46$ nm and the adhesion force is approximately 1.23 N. The out-of-plane restoring force from the four flexures at 1.5 µm vertical deflection is $(4 \times k_{\text{oop}}) \times 1.5\,\mu\text{m} \approx 0.15$ mN for the 5 µm device and 100 mN for the 20 µm device. For both device thicknesses, the stiction force is enormous and practically irreversible, especially at this scale. This stiction must be avoided at all costs.

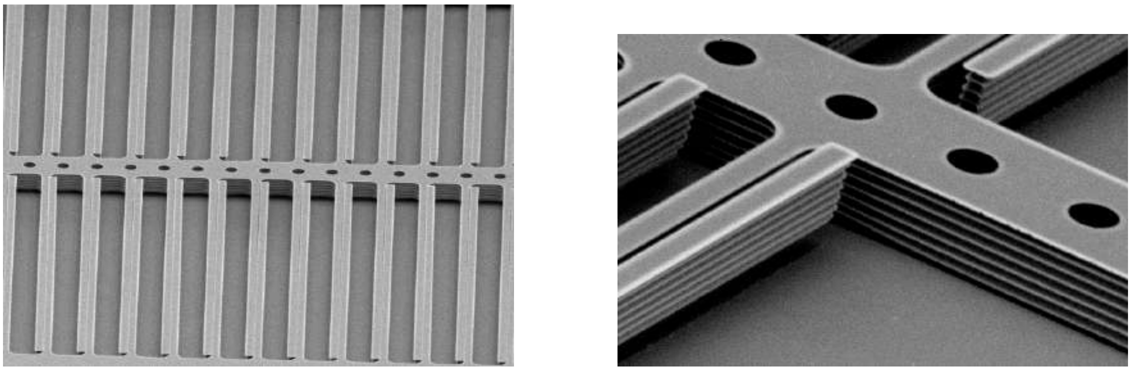

(a) Fin-to-fin stiction following pull-in.

(b) Shuttle-to-substrate stiction.

Figure 4.15: Two stiction failure modes.

The thickness dependence differs between the two modes. For fin stiction, both the adhesion force and in-plane flexure stiffness scale linearly with thickness. For shuttle stiction, the adhesion force overshadows the displacement force even for thicker devices.

4.1.7. Measurement sensitivity

The measurement range for tensile stress-strain tests is characterized as a function of sample stiffness k_s over the actuation range stipulated earlier, see 4.1.5. The shuttle displacement equals the sample elongation directly, and increased displacement improves capacitance sensitivity.

Achievable strain Figure 4.16 shows the achievable sample strain ε_s versus k_s for both device thicknesses. Softer samples reach higher strains at any given voltage, and the strain increases until the pull-in point or until the fin contact voltage limit is reached. The 20 µm device achieves substantially higher strains for stiffer samples due to its, roughly, fourfold greater actuation force.

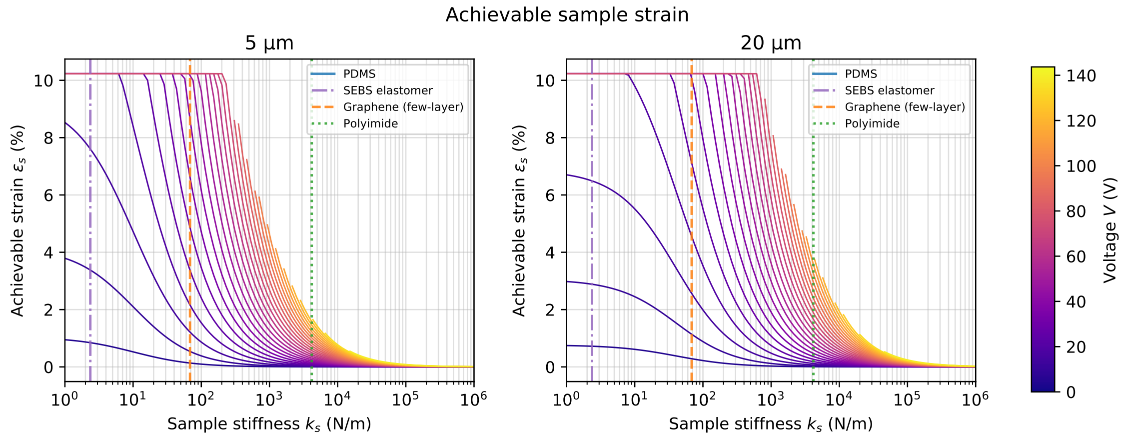

Figure 4.16: Achievable sample strain ε_s versus sample stiffness k_s for the 5 µm (left) and 20 µm (right) devices. Each line corresponds to an actuation voltage value, colored from purple (low) to yellow (high). The fin deformation contact voltage limit constrains the maximum strain, particularly for the 5 µm device with stiff samples.

Strain measurement uncertainty The strain, which equals the shuttle displacement, is calculated from the measured capacitance C. Given an arbitrary measurement resolution of $\delta C = \pm 0.01$ pF, the strain uncertainty is:

$$\delta\varepsilon_s = \frac{\delta C}{\left|\frac{dC}{dx}\right| \cdot L_0}, \tag{4.28}$$

where dC/dx is the local capacitance gradient from (4.13) and $L_0 = 6$µm is the initial sample gauge length. As displacement increases, the close gap $d_{10} - x$ decreases and dC/dx increases due to the nonlinear capacitance-displacement relationship, improving precision. Figure 4.17 shows $\delta\varepsilon_s$ versus k_s for both devices. At higher actuation voltages and larger displacements, the measurement uncertainty decreases. Additionally, this figure shows that the strain measurement uncertainty is multitudes higher for the thin device, 5 µm, as compared to the thick device, 20 µm. Softer samples, which stretch more at a given voltage, benefit from both higher achievable strain and lower measurement uncertainty. Stiffer samples require higher voltages to achieve comparable precision but are limited by the fin contact voltage.

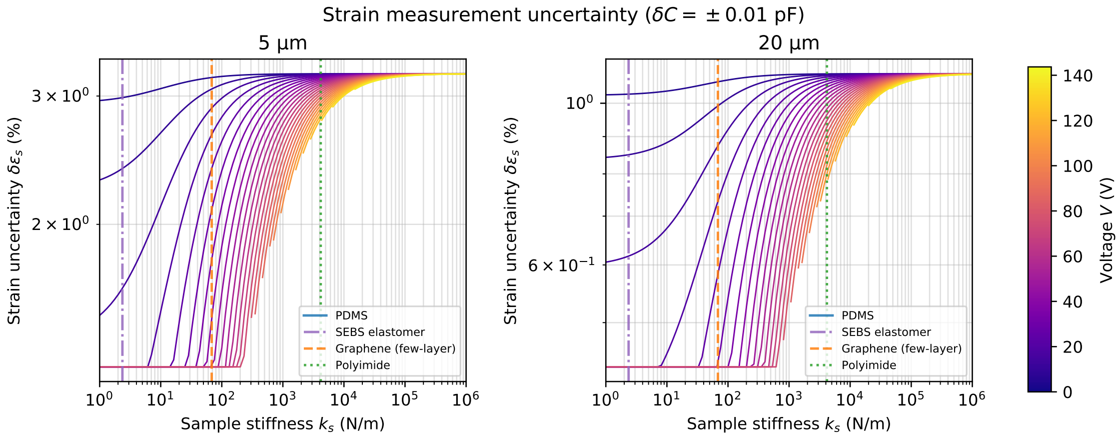

Figure 4.17: Strain measurement uncertainty $\delta\varepsilon_s$ versus sample stiffness k_s for the 5 µm (left) and 20 µm (right) devices, assuming a capacitance measurement resolution of $\delta C = \pm 0.01$ pF.

These plots show that increasing the comb overlap area, increases the maximal sample stiffness (decreasing the necessary actuation voltage) while still achieving maximal strain and increases the strain measurement accuracy.

4.2. Experimental methodology

The theoretical model is validated through two complementary measurements on a single 5 µm device without a sample: the voltage-displacement relation, obtained from SEM imaging under stepwise actuation, and the voltage-capacitance relation, obtained with a potentiostat in series with the device through a bias tee. Both measurements share the same wiring, summarized in Figure 4.20.

4.2.1. Capacitance measurements

The device requires simultaneous application of a DC actuation voltage, for actuation, and an AC measurement signal, for displacement measurement, through the same two electrodes. Combining these on a single circuit introduces some complexity, as the AC potentiostat must be protected from the DC voltage of the power supply, and the DC power supply must be protected from the AC signal.

A bias tee is a three-port component that is able to combine an AC and DC signal. In essence, a capacitor on the AC path blocks the DC voltage from the power supply but passes the AC signal. On the DC connection, an inductor passes the DC current but blocks the AC measurement signal. Commercial bias tee's implement a series of capacitors and inductors to accept a wide frequency range, as a simple single capacitor/ inductor bias tee has a very limited pass-band. No bias tee is perfect and introduce parasitic capacitances and insertion losses. A simplified circuit diagram is shown in figure 4.18.

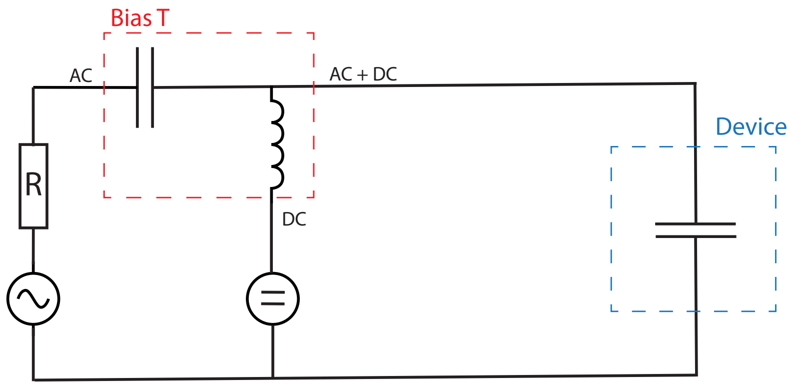

Figure 4.18: Simplified electrical circuit for actuation and measuring of the electrostatic device. The bias tee and electrostatic device are highlighted in red and green respectively.

4

To measure the capacitance of the device a resistor, with resistance R, is placed in series with the capacitor, the comb structure in this case. The total impedance of the circuit is:

$$Z = R - jX_C = R - j\frac{1}{\omega C} \tag{4.29}$$

And the phase angle is described as:

$$\tan\phi = -\frac{X_C}{R} = -\frac{1}{\omega RC} \tag{4.30}$$

where X_C is the capacitive reactance, $\omega = 2\pi f$ is the angular frequency with frequency f, R and C as the resistance and capacitance, and ϕ represents phase angle. The phase sensitivity for capacitance changes is described as:

$$\frac{d\phi}{dC} = \frac{1}{1+\left(\frac{1}{\omega RC}\right)^2}\frac{\omega R}{(\omega RC)^2} \tag{4.31}$$

From this equation it is found that the maximal sensitivity is achieved when $\omega RC = 1$, which relates to a phase shift of $\phi = -45°$. Thus, equation 4.30 becomes: $\tan(-45°) = -1 = -\frac{X_C}{R}$ and the capacitance can be found with:

$$C = \frac{1}{2\pi f_{45} R} \tag{4.32}$$

The choice of R sets the frequency f_{45} at which the $-45°$ crossing occurs. At very low frequencies, the capacitive reactance becomes large and requires an impractically high resistance; at very high frequencies (multiple MHz), parasitic capacitances and inductances start to influence the measurement. A third constraint relates to the eigenfrequencies of the device: although the AC measurement amplitude is small ($\leq 100\,\text{mV}$), at an eigenfrequency it can induce mechanical vibrations and negatively impact the capacitance measurement. The eigenfrequencies are computed in COMSOL and are listed in Section 4.1.4.

In this work, rather than tuning R to the expected capacitance range, an arbitrary resistance of 1 kΩ was used. A single wide-band frequency sweep, shown in Figure 4.19, was then performed at zero actuation voltage to locate the $-45°$ crossing and to verify that it lies sufficiently far from any device eigenfrequency. The bias tee used has a specified pass-band from 0.1 MHz to 1000 MHz; the low-frequency edge is visible in Figure 4.19 as the unstable phase region below approximately 100 kHz, while the phase response settles cleanly at higher frequencies. After this initial check, the sweep range was narrowed around the identified crossing frequency to improve the resolution of f_{45} at each subsequent actuation setpoint.

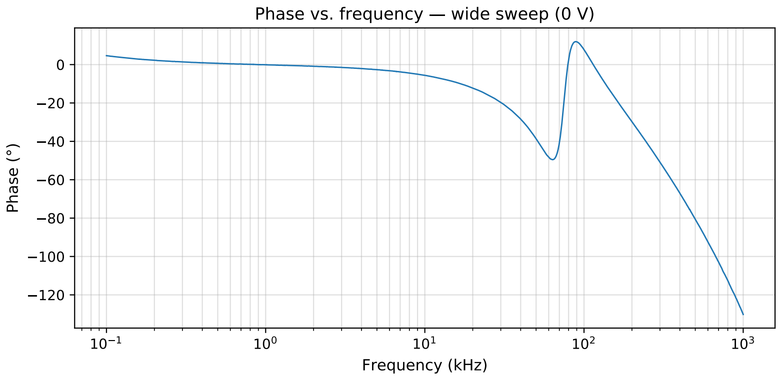

Figure 4.19: Wide-band frequency sweep of the device in series with the 1 kΩ resistor at actuation voltage $V = 0$, used to locate the $-45°$ phase crossing and confirm that it falls outside the predicted device eigenfrequencies. Below the bias-tee pass-band edge (~ 100 kHz) the phase is unstable; above it the phase response stabilizes and crosses $-45°$ in the measurement window used for the subsequent actuation sweep.

At every actuation voltage setpoint, a narrow frequency sweep is performed and a fit is applied to extract f_{45}, from which the capacitance is then obtained through (4.32).

4.2.2. Voltage-displacement SEM measurement

To measure the displacement of the shuttle in correlation with the actuation voltage, a device was placed in a SEM. Using a vacuum feedthrough, an image is taken at different actuation setpoints. From these images, the gap size is extrapolated using ImageJ and the voltage-displacement results are plotted, see Figure 4.21. A schematic of the test setup is shown in Figure 4.20.

The wiring follows the bias-tee architecture introduced in Section 4.2.1: the DC port supplies the actuation voltage, the AC port supplies the small-signal measurement voltage, and both are combined onto the device electrodes. For sample-less characterization the required actuation voltage stays below 10 V, and the Moku:Go (a multi-instrument platform used here as both signal generator and frequency response analyzer) was used for both the DC actuation and the AC measurement signal. The AC amplitude was set to

200 mV peak-to-peak, sufficiently small that the resulting electrostatic force does not measurably actuate the shuttle and the AC signal only probes the capacitance.

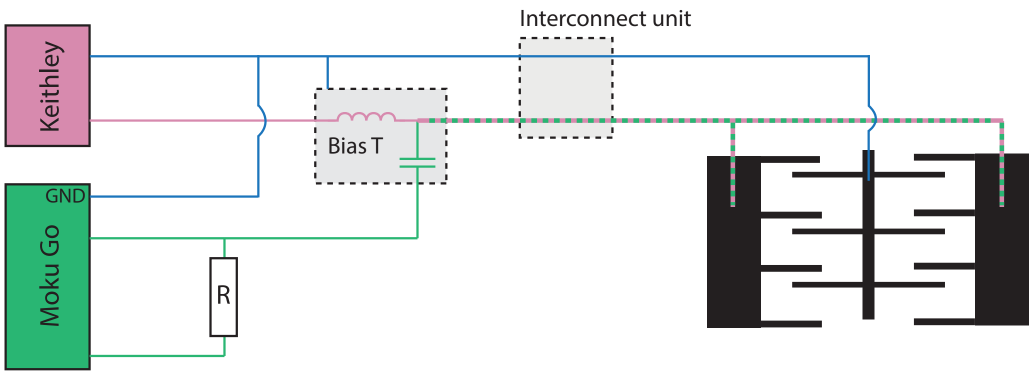

Figure 4.20: Schematic of the wiring of the test setup for the electrostatic device. The Keithley source provides the DC actuation voltage in the general case; for the no-sample measurements reported here the Moku:Go supplied both the DC actuation and the AC measurement signal. The bias tee combines both signals onto the device electrodes.

4.3. Results and discussion

The measured voltage-displacement and voltage-capacitance relations are presented and compared to the analytical predictions of Section 4.1. The scope of the dataset (a single 5 μm device without a sample) precludes formal fitting of the model parameters; the corresponding limitations and proposed extensions are collected in Section 4.4.

4.3.1. Voltage-displacement

The measured voltage-displacement results are shown in Figure 4.21.

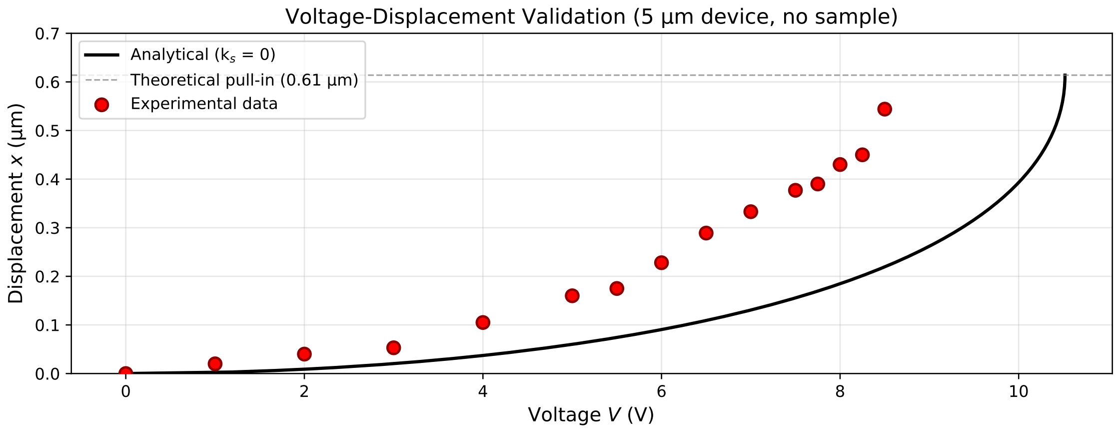

Figure 4.21: Measured shuttle displacement versus actuation voltage for a 5 μm electrostatic device without sample. Displacements were extracted from SEM images at each voltage setpoint via ImageJ; the analytical prediction from (4.25) is overlaid for comparison.

The discrepancy is consistent with the simplifications identified in the theoretical model. The analytical flexure stiffness exceeds the COMSOL value by approximately 9 % (Section 4.1.1), and the effective beam width $w_0' = w_0 - 2w_C$ depends cubically on the assumed scallop depth b and on the mask undercut, both of which were taken from literature ranges rather than measured directly. A larger-than-assumed undercut, suggested by visual inspection of the fabricated devices, would lower the predicted stiffness further.

An increased force with displacement relationship is the other possible cause of this actuation underestimate. This force is underestimated when the impact of fringes is underrepresented or the actual parallel plate distance between the fins is overestimated. While scallops have been shown to decrease the effective capacitance, Pawar et al. [64] has shown that the inclination and or slant angle of the scalloped walls influence the electrostatic forces. The fin and scallop parameters are different to the ones studied here and the inclination angle is not known, given this uncertainty, this factor was not taken into account. This effect is not included in the present model.

Pull-in did seem to happen at around 0.6 µm of shuttle displacement. This agrees well with the theoretical pull-in displacement of 0.61 µm predicted by (4.20), which depends only on the initial fin gap geometry and is independent of shuttle stiffness, sample stiffness, and capacitance. This also proves that at low forces, especially in absence of a sample, the electrostatic fin deformation is negligible.

4.3.2. Voltage-capacitance

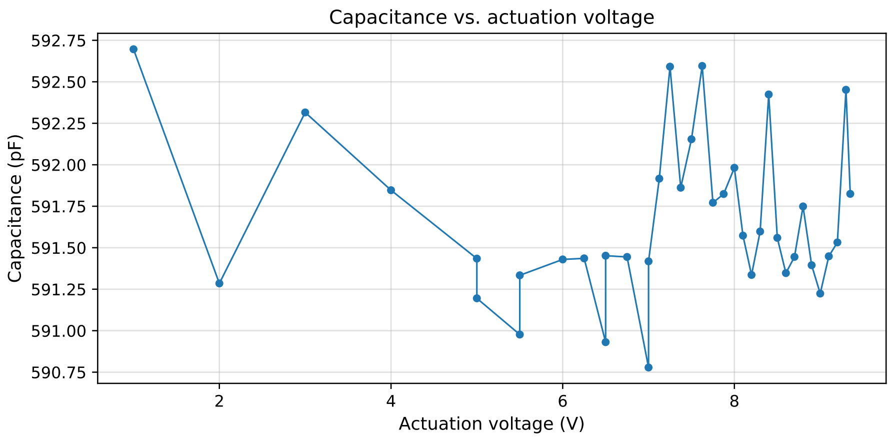

Figure 4.22: Measured capacitance versus actuation voltage for the 5 µm electrostatic device without sample. Each point corresponds to one narrow frequency sweep at the indicated voltage; the capacitance was extracted at the −45° phase crossing following the procedure of Section 4.2.1.

The measured capacitance shows no clear trend with the actuation voltage. The mean value, approximately 591 pF, lies more than three orders of magnitude above the analytical prediction of ~0.3 pF for the comb sensor at zero displacement (Section 4.1.3). This offset is attributed to parasitic capacitances along the measurement path, including the bias tee, alligator-clip cabling, and connection pins. These contributions are voltage- and comb displacement-independent and would, in principle, cancel out when only the capacitance change due to shuttle motion is considered.

The scatter on the measurement is 1 pF to 2 pF peak-to-peak, an order of magnitude larger than the expected device-level capacitance change between zero displacement and pull-in (~0.1 pF, from (4.13)). The measurement noise thus overshadows the actual results. Small changes or movement of and around the testsetup showed to influence the measurements, further proving the high sensitivity. As a result, no meaningful voltage-capacitance relation can be extracted from the present dataset, and the capacitance-displacement curve that would normally combine Sections 4.3.1 and 4.3.2 cannot be constructed.

4.4. Limitations and proposed improvements

The characterization of the electrostatic device, both analytical and experimental, contains several simplifications and shortcomings, explaining why a fit of the analytical model to the practical testing results is not performed.

Scallop and mask-undercut characterization The DRIE scallop depth b, the scallop inclination angle, and the mask undercut all influence the in-plane stiffness and electrostatic force, yet all three were taken from literature ranges. SEM imaging of the vertical features would help estimating the actual values.

Analytical stiffness and capacitance models The serpentine flexure stiffness (4.1) assumes rigid corner sections; COMSOL force-deflection simulations show this to be a 9 % overestimate (Section 4.1.1). The comb capacitance uses a single multiplicative fringe factor F_{avg} (Section 4.1.3), accurate to within a few percent for the undeformed comb but losing validity once the fins themselves deform. A displacement- and voltage-dependent fringe correction would improve the model.

Fin deformation The electrostatic fin deformation is implemented for estimating the safe operating range where the fins don't touch. For this a linearly increasing distributed constant load is used. The effect of fin bending on the comb capacitance is also neglected. Both effects become significant for stiff samples, where the device operates close to the contact limit; a complete implicit model is left to future work. This model would also solve the capacitance and stiffness inconsistencies.

Pull-in for nonlinear samples The universal pull-in condition (4.20) assumes a displacement-independent total stiffness and rigid electrostatic fins. Strain-softening or strain-hardening samples violate this assumption and require the simultaneous solution of (4.16) and (4.18) with $k_s(x)$.

Stiction Fin-to-fin stiction often occured on the 5 µm devices. This was reversible, contrary to the shuttle to handle wafer stiction which completely immobilized the shuttle. Both modes are expected to be much less likely on the 20 µm devices, whose in-plane and out-of-plane stiffnesses are much higher.

Limited measurement dataset The experimental characterization is restricted to a single 5 µm device without a sample, which precludes the parameter fitting performed for the electrothermal device in Chapter 5. Functional 20 µm devices would allow the same model to be fitted simultaneously to two thicknesses with identical in-plane geometry, providing insight on the unknown scallop and undercut parameters. Measurements with samples of known stiffness would directly test the force-equilibrium relation (4.16), and repeated measurements across nominally identical devices would quantify fabrication-induced variation.

Capacitance measurement sensitivity As reported in Section 4.3.2, parasitic capacitances of the bias tee, cabling, and chip carrier dominate the absolute capacitance reading, and the residual scatter from mechanical perturbations of the wiring exceeds the expected device-level signal. A PCB-mounted bias tee soldered directly to the chip carrier would eliminate the alligator-clip leads and most of the cable length; a guarded measurement configuration would further suppress cable parasitics. The 20 µm devices, with four times the absolute capacitance and per-volt capacitance change, would lift the device signal closer to the practical noise floor.

In summary, apart from the small dataset size, the next step is testing the 20 µm device, which simultaneously addresses the capacitance signal-to-noise problem and the stiction robustness and working out an intrinsic analytical model including the fin deformation and its effects on the capacitance as well as the actuation range.

5 Electrothermal Device

With the electrothermal device, actuation is achieved through a chevron thermal actuator, which, through Joule heating, converts thermal fin expansion into in-plane shuttle displacement. A potential applied across the fin array drives a current through the fins, generating a temperature increase and causing elongation. Because the fins are inclined with respect to the shuttle axis, their elongation is converted into a translational displacement of the thermally actuated shuttle (TAS). This displacement is transmitted to a sample bridging the gap between the TAS and the load shuttle (LS), which is capacitively sensed via a comb sensor. Similar to the Electrostatic device, four chip variants are characterized: a 5 and 20 µm thick device both in JEOL and TFS versions. A SEM image, see figure 5.1, shows a close-up of the complete thermal device.

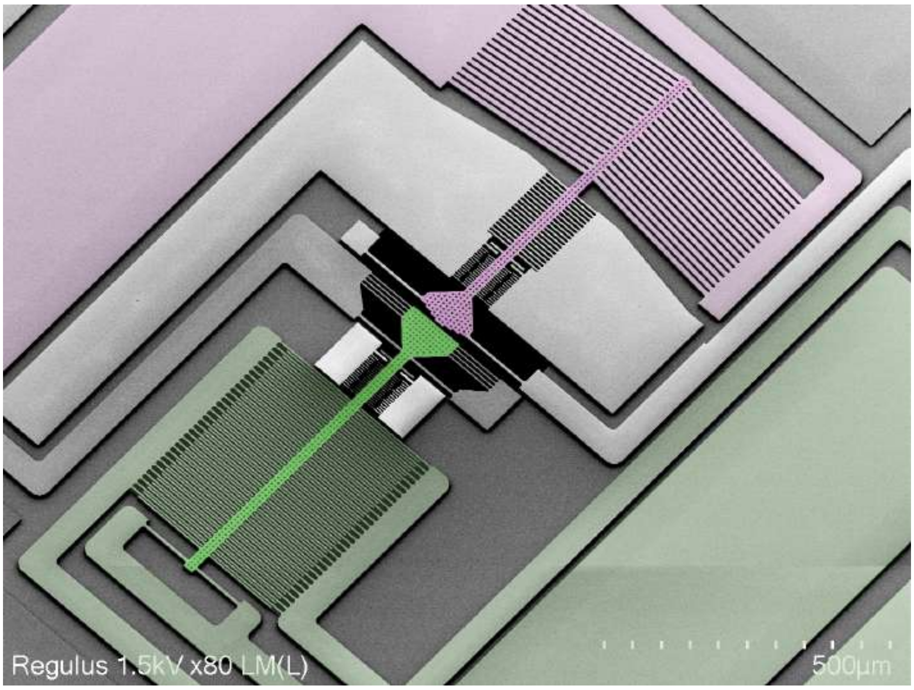

Figure 5.1: Sem image of an electrothermal 5 µm thick TFS device. The actuation elements -consisting of the chevron fins, contact pads, conduction paths, and TAS- and the measurement elements -consisting of the capacitive combs, contact pads, conduction paths, and LS- are highlighted in pink and green respectively. The TAS and LS are highlighted more. This color scheme is applied equally throughout this thesis. The sample gap is located between the two shuttles.

To perform measurements with this device, four connection points are necessary, two for applying the actuation potential over the chevron fins and two for the capacitive

LS displacement measurements. Both measurement pairs are highlighted as shown in figure 5.2.

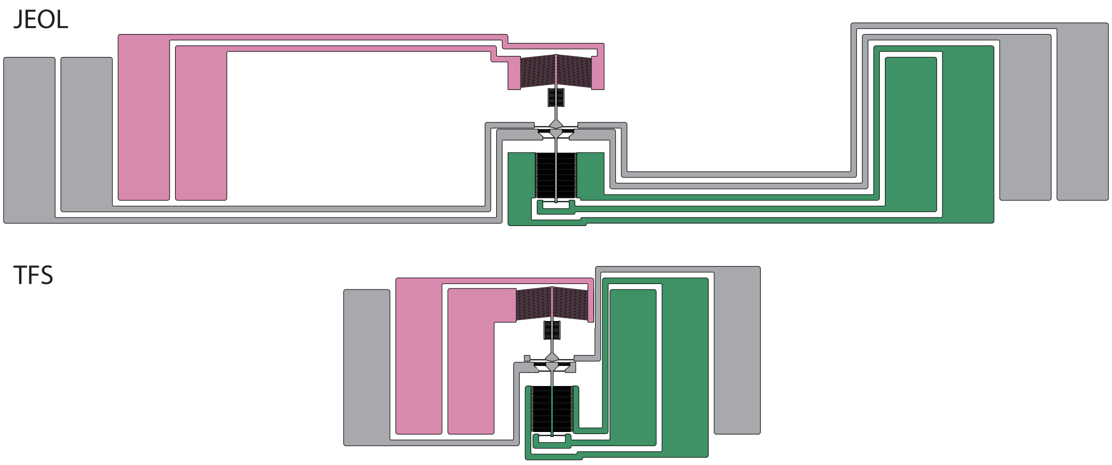

Figure 5.2: Complete electrothermal device layout for JEOL and TFS compatible systems with the actuation and measurement circuits shaded pink and green respectively.

The remainder of the chapter is split into four sections. Section 5.1 establishes the analytical framework, from the individual stiffnesses and the lumped displacement model to the chevron actuator physics, the current–temperature power balance, and the comb sensor. Section 5.2 describes the experimental characterization, in which four parameters that cannot be determined from geometry are extracted by simultaneously fitting the model to SEM displacement and Raman temperature data. Section 5.3 presents and discusses the fitted results and the extracted path resistance; Section 5.4 collects the limitations and proposed improvements.

5.1. Theoretical characterization

The theoretical characterization of the electrothermal device proceeds from the individual structural elements to the complete system. The stiffness of every flexure, the chevron fin array, and the connecting shuttle beam are derived first, as these values are later required to describe the complete system through a lumped model. Through this lumped model of the complete device, the displacement at the fin point, the TAS sample point, and the load shuttle can be expressed as a function of the applied actuation force. The chevron actuator is treated in detail thereafter: the temperature distribution along the heated fins is modeled, the temperature-dependent material properties of silicon over the relevant actuation range are established, and four expressions for the actuation force as a function of fin temperature are introduced from literature. A power-balance equation then relates the drive current to the fin temperature, completing all required equations to link electrical input to mechanical output. The comb sensor model follows, relating load shuttle displacement to capacitance change. The section concludes with an analysis of strain measurement sensitivity, which combines all preceding results to characterize the achievable strain range and force resolution as a function of sample stiffness.

5.1.1. Stiffness

All stiffness contributions relevant to the mechanical model of the device are derived in this subsection. Three distinct structural elements are considered: the supporting flexures of both the TAS and the load shuttle, whose stiffness is governed by the standard Euler–Bernoulli beam relation [81]; the chevron fin array, whose stiffness varies with the fin angle θ and must therefore be evaluated as a function of displacement; and the in-plane connecting beam between the thermal fins and the cooling flexures, whose compliance is typically neglected in the literature but is shown here to cause a non-negligible loss of actuation range and must therefore be accounted for.

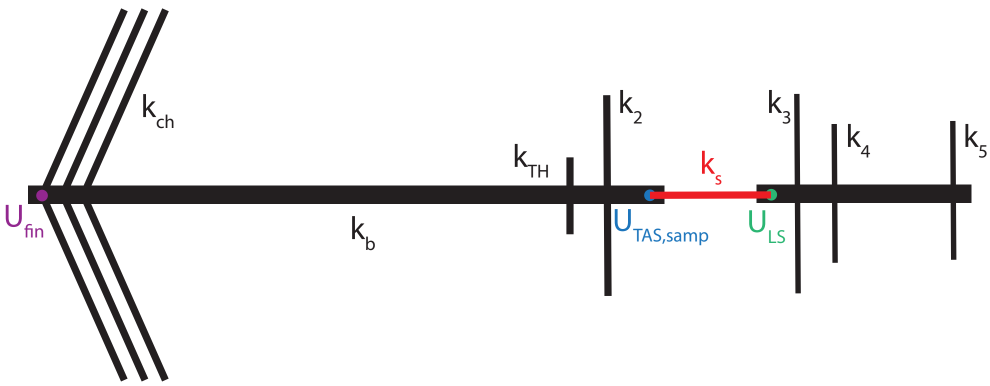

Figure 5.3: Simplified schematic of the electrothermal device with all relevant stiffnesses and displacement points.

General flexure stiffnesses Both the TAS and the LS are suspended by multiple flexures, each contributing to the total stiffness of their respective shuttle. The TAS carries two types of flexure: the heat sink fins, with stiffness k_{TH}, and the stabilization flexures, with stiffness k_2, which constrain the sample point of the TAS laterally. The load shuttle is supported by five flexure pairs: the first three, of equal stiffness and combined stiffness k_3, stabilize the sample point of the LS, while the remaining two pairs, with stiffnesses k_4 and k_5, provide additional support and constrain the rest of the LS. A simplified model of the device with all stiffnesses mentioned here is shown above in figure 5.3. All flexure stiffnesses are calculated as:

$$k_{fl} = \frac{2nEtw_{fl}^3}{l_{fl}^3} \tag{5.1}$$

where n is the number of finpairs, E the youngs modulus of the silicon, t the thickness of the device layer, w_{fl} the flexure width, and l_{fl} the flexure length.

5

Chevron fin stiffness The chevron fins constrain the TAS and contribute to its overall stiffness. Because the fin angle θ changes continuously with shuttle displacement, this stiffness is not constant over the actuation range. The expression, adapted from [82], is:

$$k_{ch} = N\left(\sin^2\theta \frac{E A_{ch}}{l_{ch}} + \cos^2\theta \frac{E A_{ch} w_{ch}^2}{l_{ch}^3}\right) \tag{5.2}$$

where N is the number of fin pairs, $A_{ch} = t\,w_{ch}$ the fin cross-sectional area, l_{ch} the fin length, and θ the instantaneous chevron angle. Figure 5.4 defines all geometric parameters in both the resting and actuated states.

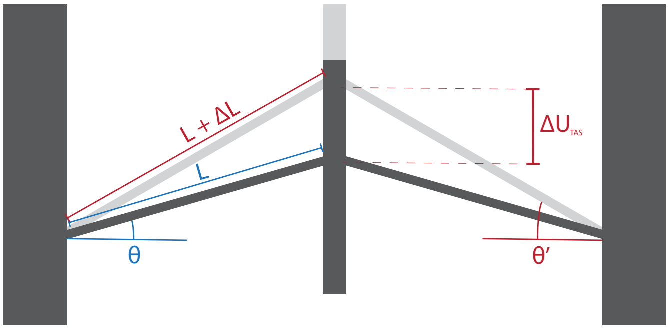

Figure 5.4: Schematic of the thermal fin mechanism. Blue and red dimensions depict the geometric parameters at ambient and working temperature respectively. The translated configuration is shown in light gray.

In-plane beam stiffness The thermal sink flexures and thermal actuator fins are relatively stiff, as compared to the other flexure stiffnesses, and, because of this, the beam segment connecting the chevron fins with these thermal sink flexures may deform under actuation. COMSOL simulations demonstrate that this deformation of the beam is not negligible, as illustrated in Figure 5.5. This compliance must therefore be accounted for in the mechanical model, unlike in prior work where the connecting beam is treated as rigid [82]. The beam stiffness is modeled as an axially loaded bar:

$$k_b = \frac{E A_{\text{beam}}}{l_b} \tag{5.3}$$

where $A_{\text{beam}} = t\,w_s$ is the shuttle cross-sectional area, w_s the effective shuttle width, and l_b the shuttle beam length. Young's modulus E is evaluated at the local beam temperature, which varies with actuation level, using (5.13).

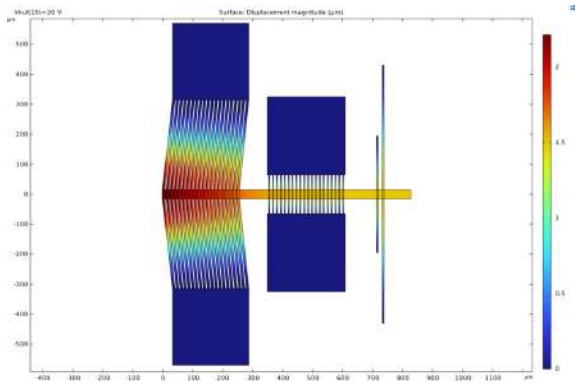

Figure 5.5: Comsol simulation of the TAS showing the displacement. From the chevron fins to the heat sink, the central beam elongates around ≈0.8 µm. This results in a significant actuation range loss at the sample point.

The release holes in the shuttle, included to facilitate the vapour HF underetch, reduce the effective beam stiffness. Simulations show that this effect can be incorporated into (5.3) without additional complexity by scaling the nominal shuttle stiffness by a factor of 0.69, the ratio $k(\text{holes})/k(\text{no holes})$ obtained from simulation. This correction is approximately constant over the full actuation range.

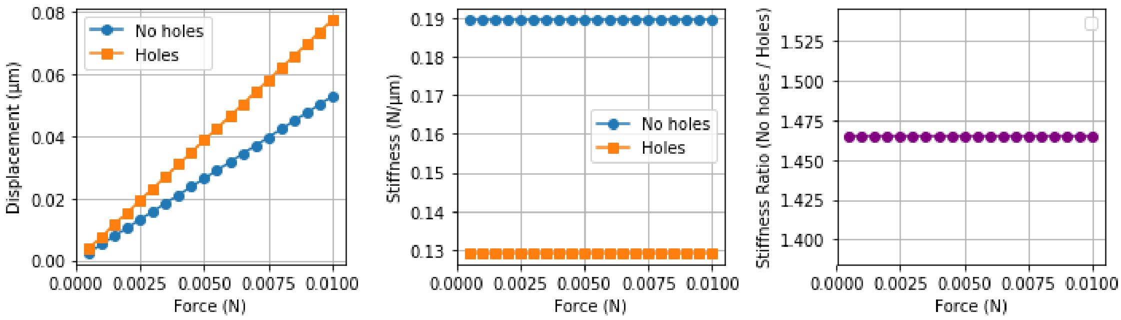

Figure 5.6: Comsol simulation results of shuttle deformation under force for a shuttle including, orange, and excluding, blue, holes.

5.1.2. Lumped model complete device

The stiffnesses derived in Section 5.1.1 are brought together into a lumped mechanical model of the complete device, from which the displacement at each measurement point of interest can be expressed as a function of the applied actuation force F. The three displacements of interest are that at the TAS sample point, $U_{\text{TAS,samp}}$, at the chevron fin point, U_{fin}, and at the load shuttle, U_{LS}; their locations are indicated in Figure 5.7.

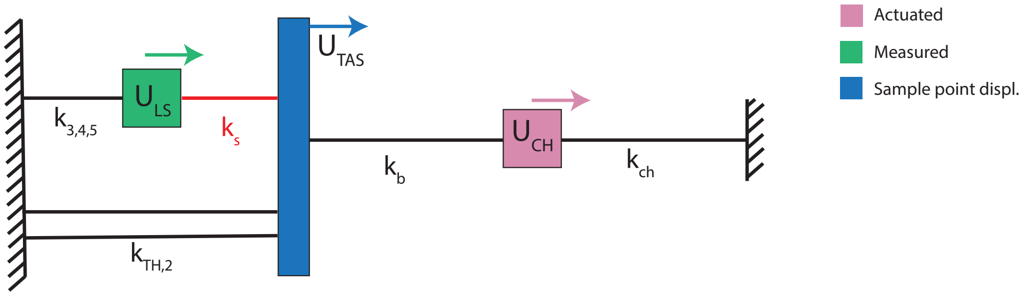

Figure 5.7: Lumped model of electrothermal device where all relevant stiffnesses and translation points used for measurements and calculations are shown.

From the lumped model it is possible to describe the displacements at the TAS sample point, $U_{\text{TAS,samp}}$, the fin point, U_{fin}, and the LS, U_{LS}, as a function of the actuation force of the thermal actuator. The three displacements are given by:

$$U_{\text{TAS,samp}} = \frac{F}{M + k_{ch} + \dfrac{k_{ch}}{k_b} M}, \tag{5.4}$$

$$U_{\text{fin}} = \frac{F}{k_{ch} + \left(\dfrac{1}{k_b} + \dfrac{1}{M}\right)^{-1}}, \tag{5.5}$$

$$U_{\text{LS}} = \frac{F}{k_{\text{LS}}\left[1 + k_{ch}\left(\dfrac{1}{M} + \dfrac{1}{k_b}\right)\right]\left[1 + \left(\dfrac{1}{k_{\text{LS}}} + \dfrac{1}{k_s}\right) k_{fl,\text{TAS}}\right]}, \tag{5.6}$$

where M is an effective load-side stiffness defined as

$$M = \left(\frac{1}{k_{\text{LS}}} + \frac{1}{k_s}\right)^{-1} + k_{fl,\text{TAS}}, \tag{5.7}$$

with k_{LS} the total load shuttle stiffness and k_s the sample stiffness. For initial characterization without a sample ($k_s \to 0$) this reduces to $M \to k_{fl,\text{TAS}}$. Without a sample connecting the TAS to the LS, no movement in the load shuttle is expected and when applying $k_s \to 0$, this displacement logically becomes: $U_{\text{LS}} \to 0$.

The difference in displacement between the TAS sample point and the load shuttle corresponds to the elongation of the sample. The strain in the sample is therefore:

$$\varepsilon_s = \frac{\Delta U_s}{L_0} = \frac{U_{\text{TAS}} - U_{\text{LS}}}{L_0}, \tag{5.8}$$

where L_0 is the initial sample gauge length, equal to the gapsize between both shuttles in unactuated state (meaning $V_{\text{act}} = 0$ V). Equations (5.4) to (5.8) together yield the sample strain as a function of actuation force for any given sample stiffness k_s.

5.1.3. Thermal dependence of material properties

The thermal, or chevron, actuator relies on thermal expansion to produce shuttle translation. By applying a potential across the fins, a current flows and generates Joule heating; the resulting elongation of the inclined fins produces an in-plane displacement, as illustrated in Figure 5.4. To model this behavior, the temperature distribution along the heated fins is established first, from which an average fin temperature is derived for use in evaluating the temperature-dependent material properties of silicon over the actuation range.

Temperature distribution and average fin temperature

The fins are heated by Joule heating and are anchored at one end to the support structure and at the other end to the shuttle. The temperature distribution along the fin is modeled as a linear gradient decreasing from a maximum temperature rise ΔT at the shuttle end ($x = 0$) to ambient over a characteristic *thermal gradient length* $L_{\Delta T}$. This length satisfies $L_{\Delta T} > l_{\text{th}} = 300$ µm, because the fin anchors and surrounding support structure also heat up to some extent, so the temperature does not return to ambient at the fin support. The temperature profile over the physical fin length l_{th} is therefore simplified to:

$$T(x) = \Delta T\left(1 - \frac{x}{L_{\Delta T}}\right) + T_{\text{amb}}, \qquad 0 \le x \le l_{\text{th}}, \tag{5.9}$$

where $\Delta T = T_{\text{max,abs}} - T_{\text{amb}}$ is the temperature rise at the shuttle contact point ($x = 0$). For $L_{\Delta T} = l_{\text{th}}$ the temperature reaches ambient exactly at the fin tip; larger values indicate that the gradient extends into the surrounding support structure, reducing the effective temperature drop across the fin length. The value of $L_{\Delta T}$ cannot be determined from geometry alone and is obtained by fitting to experimental data (Section 5.2.3).

The effective temperature drop across the fin length, which governs thermal expansion, is:

$$\Delta T_{\text{fin}} = \Delta T \cdot \frac{l_{\text{th}}}{L_{\Delta T}}. \tag{5.10}$$

If the temperature at the fin structure equals ambient, then the temperature from shuttle to support structure equals $\Delta T = \Delta T_{\text{fin}}$, and the length over which this ΔT is achieved equals the fin length; $L_{\Delta T} = l_{\text{th}} = 300$ µm.

The material properties governing fin behavior vary with temperature and must therefore be evaluated at a representative fin temperature. The average temperature rise along the fin length is used for this purpose:

$$\bar{T} = \frac{1}{l_{\text{th}}}\int_0^{l_{\text{th}}} T(x)\,\mathrm{d}x = \Delta T\left(1 - \frac{l_{\text{th}}}{2\,L_{\Delta T}}\right) + T_{\text{amb}}. \tag{5.11}$$

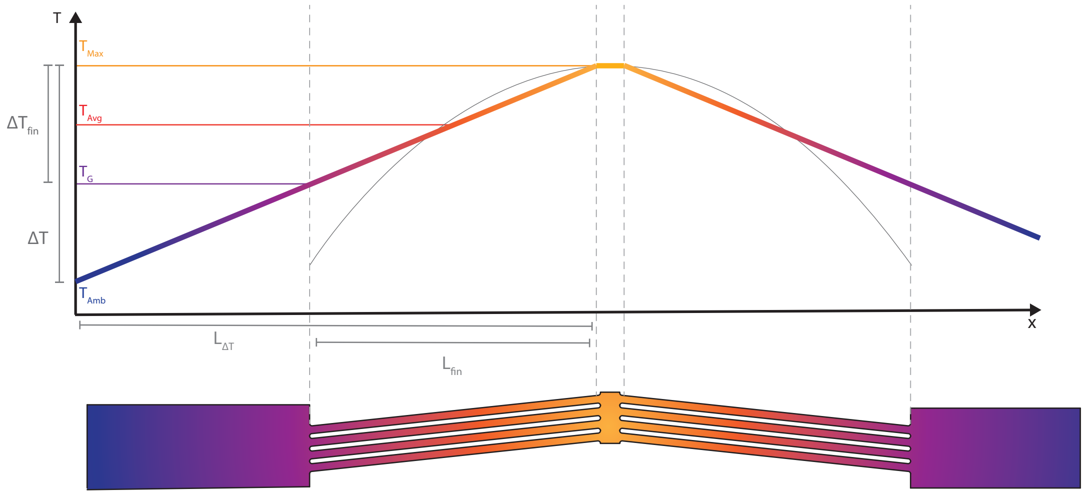

Figure 5.8: Linear temperature gradient model along the fin. The hyperbola roughly represents another heat gradient formula, which assumes ambient temperatures at the supports [83].

5

Temperature-dependent material properties
The actuation range extends up to approximately 600 °C above ambient, beyond which material damage and geometric nonlinearities may occur. Over this range, four material properties of the fins vary sufficiently to warrant explicit temperature dependence: the thermal expansion coefficient, Young's modulus, thermal conductivity, and electrical resistivity. Each is evaluated at the average fin temperature $\bar{T}$ defined by (5.11).

Thermal expansion coefficient The thermal expansion coefficient of monocrystalline silicon varies significantly over the temperature range considered. Following Kozlovskii and Stankus [84], the coefficient is expressed as a function of the absolute average fin temperature $\bar{T}_K = \bar{T} + 295\,\mathrm{K}$:

$$\alpha(\bar{T}_K) = \begin{cases} \left(-3.175 + 2.75 \times 10^{-2}\,\bar{T}_K - 3.32 \times 10^{-5}\,\bar{T}_K^2 + 1.21 \times 10^{-8}\,\bar{T}_K^3\right) \times 10^{-6}\,\mathrm{K}^{-1}, & \bar{T}_K < 560\,\mathrm{K}, \\ \left(3.14 + 1.42 \times 10^{-3}\,\bar{T}_K\right) \times 10^{-6}\,\mathrm{K}^{-1}, & \bar{T}_K \geq 560\,\mathrm{K}. \end{cases} \tag{5.12}$$

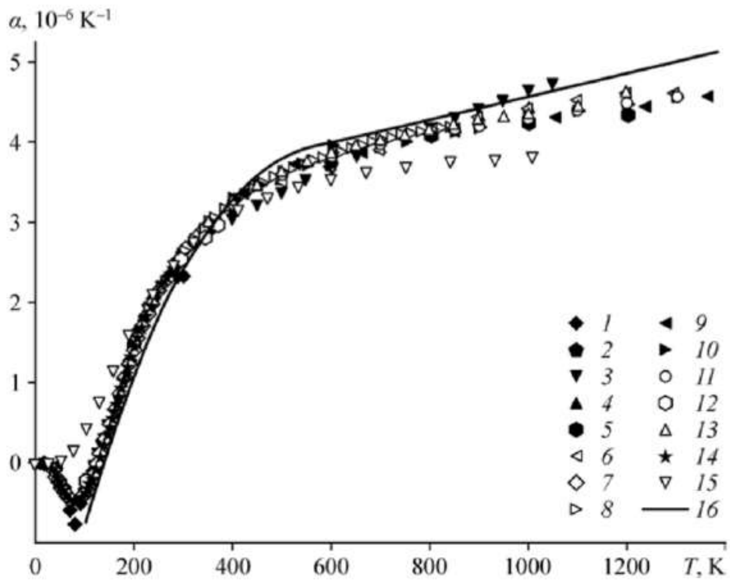

Figure 5.9: Temperature dependence of the thermal expansion coefficient of monocrystalline silicon [84]

Young's modulus The Young's modulus of silicon decreases approximately linearly with temperature. Based on the measurements reported by Namazu *et al.* [85]:

$$E(\bar{T}) = E_0 - 0.0406 \times 10^9 \cdot \bar{T} \quad [\mathrm{Pa}] \tag{5.13}$$

where $E_0 = 169\,\mathrm{GPa}$ is the room-temperature value for silicon in the $\langle 110 \rangle$ direction and $\bar{T}$ is in °C[85]. Both the fins and the connecting shuttle beam are assumed to be at the average temperature $\bar{T}$ from (5.11), so (5.13) is applied uniformly to all structural elements of the TAS.

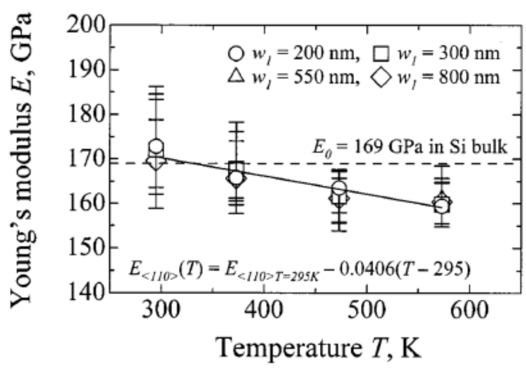

Figure 5.10: Experimental data and fit for the temperature dependence of silicon's Young's modulus [85].

Thermal conductivity The thermal conductivity of silicon decreases with temperature following a power-law relation. Based on Williams *et al.* [86], evaluated at the average fin temperature $\bar{T}$:

$$\kappa(\bar{T}) = f_{\mathrm{dop}}\,\kappa_{\mathrm{amb}}\left(\frac{300+\bar{T}}{300}\right)^{-4/3} \tag{5.14}$$

where κ_{amb} is the thermal conductivity at ambient temperature. The factor of f_{dop} accounts for the reduction in thermal conductivity relative to the intrinsic value caused by increased phonon scattering at the doping concentrations present in the device layer. Experimental measurements on heavily doped single-crystal silicon report reductions of 10–25 % depending on dopant species and concentration [87], consistent with the correction applied here. This temperature-dependent conductivity enters the current–temperature model (Section 5.1.4) and all material property evaluations above.

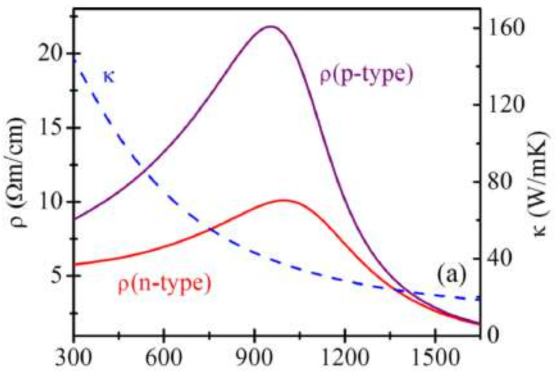

Figure 5.11: Temperature dependence of silicons thermal conductivity together with the electrical resistance for p- and n-type silicon [86]

Electrical resistivity In heavily doped silicon, carrier scattering is dominated by phonon interactions, giving rise to a positive, approximately linear dependence of resistivity on temperature analogous to that of a metal. This behavior persists throughout the extrinsic conduction regime, which for the doping concentrations relevant here extends well beyond the maximum actuation temperature considered. The temperature-dependent resistivity is therefore modeled as:

$$\rho(\Delta T) = \rho_0\,(1+\alpha_R\,\Delta T)\,, \tag{5.15}$$

where ρ_0 is the electrical resistivity at ambient temperature, α_R the temperature coefficient of resistance (TCR), and ΔT the local temperature rise. This linear approximation is standard in the MEMS thermal actuator literature for heavily doped silicon devices [11], [82] and is used in Section 5.1.4 to evaluate the temperature-dependent fin resistance.

5.1.4. Actuation force with fin temperature

The actuation force now is related to the fin temperature through four expressions from the literature, categorized into a displacement method and a force method. Once the actuation force is known, the displacements at all points of interest follow directly from the lumped model of Section 5.1.2. In the displacement method, the displacement regime of the chevron array in absence of any other support structure or flexures is calculated first. From this free displacement, it is possible to find the actuation force together with the stiffness of the chevron fins from (5.2). In the force method, the actuation force is related to the fin temperature directly, without the intermediate step of computing a free displacement. The displacements accross the device are then found with using the lumped system with formulas 5.4, 5.5, and 5.6. Finally, an energy-balance equation relates the drive current to the fin temperature, completing the analytical chain from electrical input to mechanical output.

Fin displacement method

In the displacement method, the total actuation force follows from the free displacement of the fin array via:

$$F = k_{ch} \cdot U_{\text{free}}, \tag{5.16}$$

where k_{ch} is the total chevron stiffness from (5.2) and U_{free} is the free displacement of the thermal actuator without any external support stiffness, i.e. without any flexures. Two expressions for U_{free} are considered. The first, from Sinclair [88], gives:

$$U_{\text{free,S}} = l_{\text{th}}\sqrt{1 + 2\,\alpha\,\Delta T_{\text{fin}} - \cos^2\theta} \; - \; l_{\text{th}}\sin\theta. \tag{5.17}$$

The second formula, from Pérez Garza [82], includes the ratio of axial to bending stiffness of the fin:

$$U_{\text{free,H}} = \alpha\,\Delta T_{\text{fin}}\,l_{\text{th}}\frac{\sin\theta}{\sin^2\theta + \cos^2\theta\,\dfrac{12\,I_z}{\psi}}, \tag{5.18}$$

where $\psi = A_f\,l_{\text{th}}^2/(12\,I_z)$ is the axial-to-bending stiffness ratio, $A_f = t\,w_f$ is the fin cross-sectional area, and $I_z = w_f^3\,t/12$ is the second moment of area of the fin cross-section about the out-of-plane axis.

Force method

The force method relates the actuation force to the fin temperature directly. The first expression, from Espinoza *et al.* [11], is derived by treating each fin as an axially constrained beam: thermal expansion generates a blocked force $E\,A_f\,\alpha\,\Delta T_{\text{fin}}$ along the fin axis, which is then projected onto the shuttle direction through the chevron angle:

$$F_E = 2N\,E\,A_f\,\alpha\,\Delta T_{\text{fin}}\,\sin\theta. \tag{5.19}$$

This expression neglects the bending flexibility of the fin, implicitly assuming that axial deformation dominates. The second expression, due to Pérez Garza [82], corrects for this by weighting the axial and bending contributions through the same stiffness ratio ψ introduced in (5.18):

$$F_R = 2N\alpha E \Delta T_{\text{fin}} A_f \frac{\cos\theta}{\dfrac{\sin^2\theta}{\psi} + \cos^2\theta}. \tag{5.20}$$

When the fin is much stiffer axially than in bending ($\psi \gg 1$), the denominator reduces to $\cos^2\theta$ and (5.20) approaches the Espinoza expression in the small-angle limit. The two force-method expressions thus represent opposite ends of the same physical assumption about fin stiffness, and their comparison with the displacement-method formulae in the fitted results of Section 5.3.1 provides a direct test of which assumption better describes the actual fin behavior.

Actuation temperature with current

The fin temperature is related to the drive current through a power balance. Basing this relationship on the actuation voltage rather than the current would be inconsistent across chips and measurement setups, since the total circuit resistance varies between the TFS and JEOL chip designs and between different wire materials and connection configurations. The current is therefore the appropriate independent variable, as it determines the Joule heating in the fins directly regardless of the external circuit.

Conservation of energy requires that the electrical power dissipated in the fins equals the total rate of heat loss. Three dissipation pathways are considered: conduction through the fins into their anchors, conduction through the shuttle towards the cooling flexures, and thermal radiation. Convection is absent as the device is operated under high vacuum. This gives:

$$I^2 R_{f,\text{tot}} = \left(\frac{2N\kappa A_f}{L_{\Delta T}} + \frac{\kappa A_s}{L_s}\right)\Delta T + \sigma A_{\text{rad}}\left(T^4_{\text{max,abs}} - T^4_{\text{amb}}\right), \tag{5.21}$$

where σ is the Stefan–Boltzmann constant, $A_f = t\,w_f$ the fin cross-sectional area, $A_s = t\,w_s$ the shuttle cross-sectional area, and $\kappa(\bar{T})$ the temperature-dependent thermal conductivity from (5.14). The shuttle conduction length L_s and the effective radiation area A_{rad} cannot be determined from geometry alone and are obtained by fitting, as described in Section 5.2.3. Equation (5.21) can be rearranged to yield the drive current I analytically as a function of ΔT, once the total fin resistance $R_{f,\text{tot}}$ is known.

The total electrical resistance of the N fin pairs is evaluated using the temperature-dependent resistivity (5.15) and the thermally expanded fin length:

$$R_{f,\text{tot}} = \frac{2\rho(\Delta T)\, l_{\text{th}}}{N A_f} \tag{5.22}$$

5.1.5. Comb sensor

The displacement of the load shuttle is measured through a capacitive comb sensor. Apart from different dimensions, this mechanism functions exactly like the comb sensor of the electrostatic device. The analytical approach and working principles are described in 4.1.3 and not repeated here.

The resulting comb capacitance with load shuttle displacement for both device thicknesses is plotted below, figure 5.12.

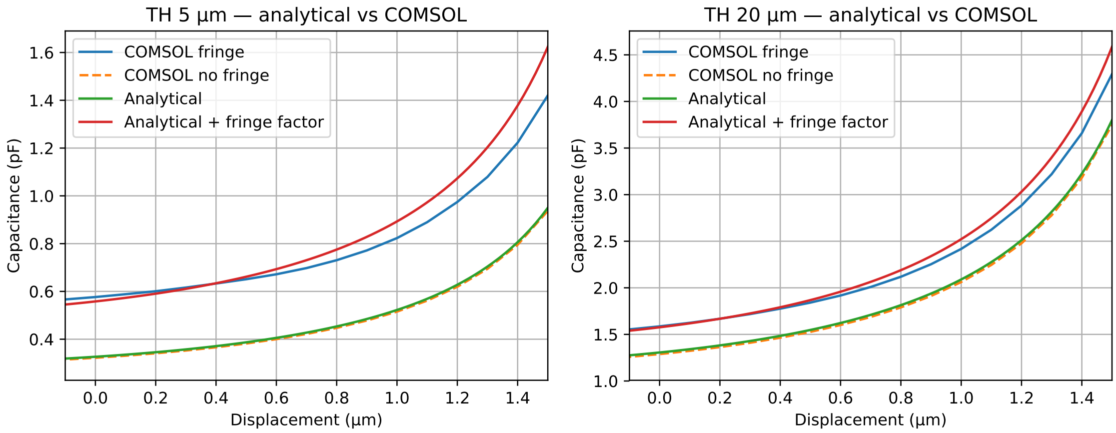

Figure 5.12: Capacitance versus displacement for the 5 µm (left) and 20 µm (right) load shuttle. The analytical parallel-plate formula (dashed orange), not including fringes, matches the no-fringe COMSOL simulation (green) closely. The full simulation including fringe fields (blue) shows the expected capacitance increase due to edge effects. The analytical model corrected with a constant fringe factor f (red) approximates the full simulation well over the limited displacement range.

5

5.1.6. Measurement sensitivity

Now that the complete device is described analytically, the measurement capability for tensile stress–strain tests can be characterized as a function of sample stiffness k_s. Two opposing effects govern the choice of sample stiffness. For a very stiff sample ($k_s \to \infty$), the TAS and LS are mechanically coupled and both displace equally, leaving the sample virtually unstrained: $\varepsilon_s \to 0$ (see (5.8)). For a very compliant sample ($k_s \to 0$), the LS is effectively decoupled from the TAS and undergoes no displacement ($U_{\mathrm{LS}} \to 0$), so the capacitance change is negligible and the strain cannot be measured. The optimal sample stiffness lies between these extremes.

Achievable strain Figure 5.13 shows the achievable sample strain ε_s for a range of k_s for the 5 µm and 20 µm devices across the full actuation range $\Delta T = 0$–$600\,°\mathrm{C}$. As expected, higher actuation temperatures increase the achievable strain at any stiffness. For either device, the strain peaks at low k_s and decays toward zero as k_s increases. The 20 µm device produces higher absolute strains for stiffer samples because its greater thickness increases the chevron actuation force.

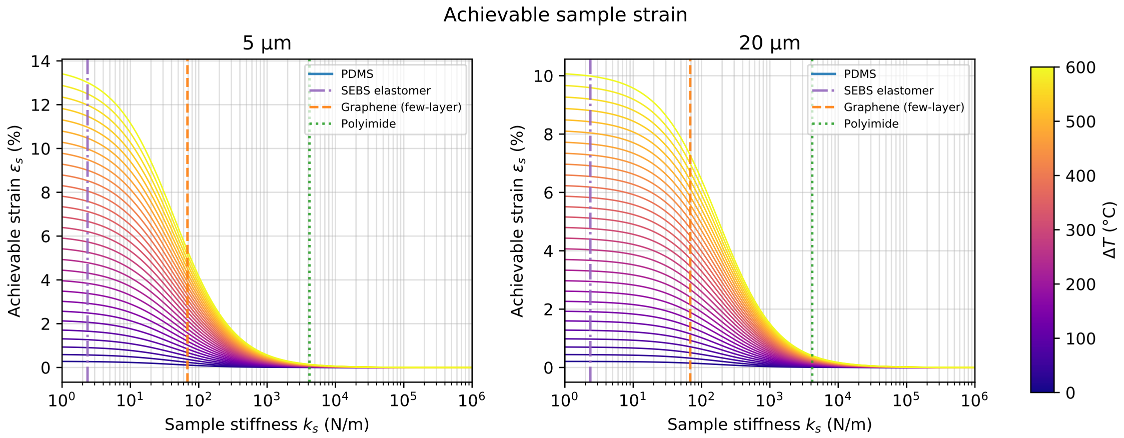

Figure 5.13: Achievable sample strain ε_s versus sample stiffness k_s for the 5 μm (left) and 20 μm (right) devices. Each line corresponds to a fin temperature rise ΔT from 0 °C to 600 °C, colored from dark (low) to bright (high) by the plasma gradient.

Strain measurement uncertainty The strain is inferred from the measured load-shuttle capacitance C. Given a figurative potentiostat resolution of $\delta C = \pm 0.01$ pF, the resulting strain uncertainty is

$$\delta\varepsilon_s = \frac{\delta C}{\left|\dfrac{dC}{dU_{\text{LS}}}\right| \cdot L_0}, \tag{5.23}$$

where dC/dU_{LS} is the local slope of the capacitance–displacement curve, evaluated numerically to account for the nonlinear parallel-plate relationship. As k_s increases and $U_{\text{LS}} \to U_{\text{TAS}}$, the close gap $d_{10} - U_{\text{LS}}$ shrinks and dC/dU_{LS} grows, improving the capacitance sensitivity and reducing $\delta\varepsilon_s$. At low k_s, $U_{\text{LS}} \approx 0$ and the capacitance is near its unactuated value, giving poor precision. Figure 5.14 shows $\delta\varepsilon_s$ versus k_s for both devices.

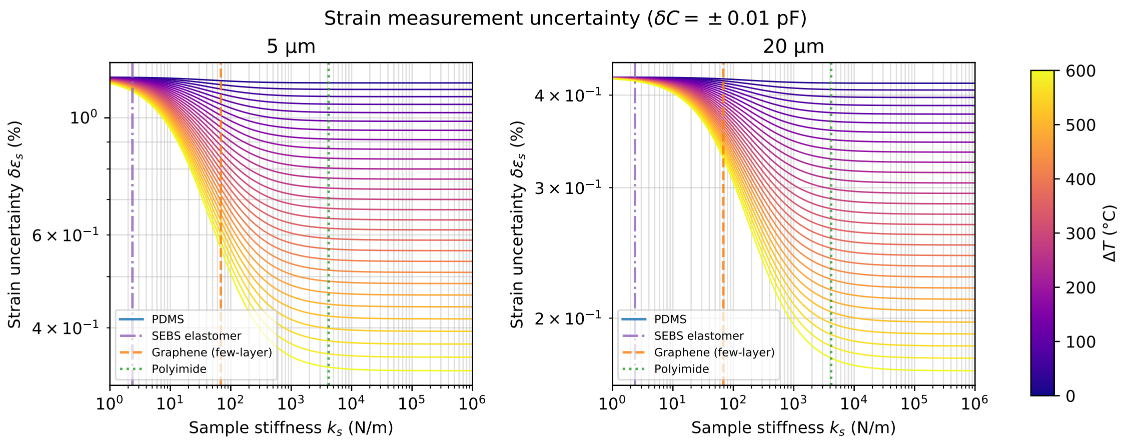

Figure 5.14: Strain measurement uncertainty $\delta\varepsilon_s$ versus sample stiffness k_s for the 5 μm (left) and 20 μm (right) devices, assuming a potentiostat resolution of $\delta C = \pm 0.01$ pF. The log–log scale reveals that uncertainty spans several orders of magnitude across the stiffness range.

Figure of merit and optimal stiffness The two quantities described above are directly opposed: a stiffer sample gives better capacitance precision but smaller strain, while a more compliant sample gives larger strain but worse precision. To quantify where meaningful measurements are possible, a dimensionless figure of merit is defined as their ratio:

$$\mathrm{FOM} = \frac{\varepsilon_s}{\delta\varepsilon_s} = \frac{(U_{\mathrm{TAS}} - U_{\mathrm{LS}})}{L_0} \cdot \frac{\left|\dfrac{dC}{dU_{\mathrm{LS}}}\right|}{\delta C / L_0}. \tag{5.24}$$

The FOM represents the number of resolvable strain increments within the achievable range: FOM < 1 means the measurement uncertainty exceeds the full strain range and the measurement is effectively impossible; FOM = 10 means ten distinct strain levels can be distinguished (given the measurement uncertainty of 0.01 pF). Figure 5.15 shows the FOM as function of both k_s and ΔT for each device. The white contour at FOM = 1 marks the lower usability boundary; the peak of the FOM surface identifies the optimal combination of sample stiffness and actuation temperature. The FOM map also shows that at low actuation temperatures the measurement is unreliable for any stiffness, regardless of sample choice, because the TAS displacement is too small relative to the capacitance noise floor.

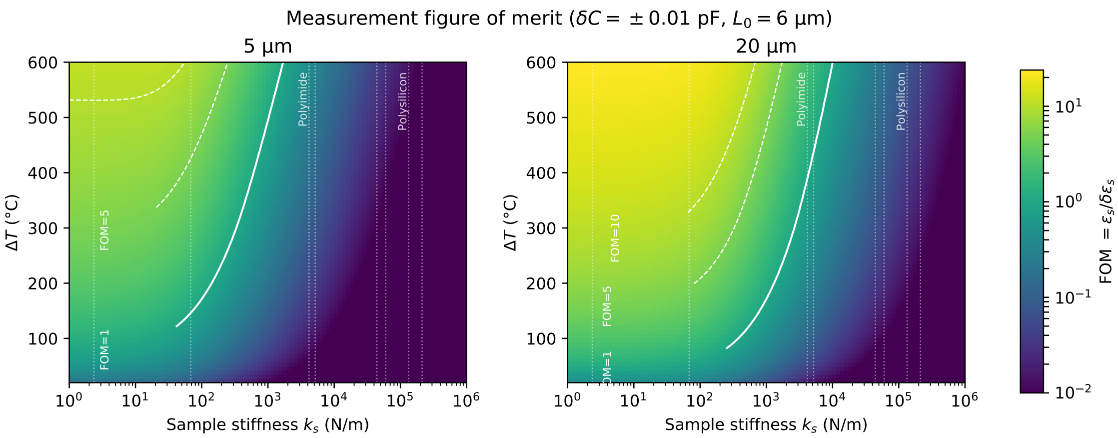

Figure 5.15: Measurement figure of merit FOM = $\varepsilon_s/\delta\varepsilon_s$ as a function of sample stiffness k_s and fin temperature rise ΔT, for the 5 µm (left) and 20 µm (right) devices. The color scale is logarithmic. White contour lines mark FOM = 1,5, and 10. The peak of each map indicates the optimal $(k_s, \Delta T)$ operating point.

5.2. Experimental methodology

The experimental methods used to characterize the device are described in this section. Two datasets are used: the sample- and fin-point displacements over the actuation range, measured in a scanning electron microscope (Section 5.2.1), and fin temperatures extracted from Raman spectroscopy measurements (Section 5.2.2). The free parameters introduced in Section 5.1, the thermal gradient length $L_{\Delta T}$, the beam stiffness length l_b, the shuttle conduction length L_s, and the effective radiation area A_{rad}, are found by fitting both datasets simultaneously, independently for each of the four actuation formulae; the fit procedure is described in Section 5.2.3. All characterization tests are performed without a sample connecting the load shuttle and the TAS, thus $k_s \approx 0$. The fitted parameter values and the comparison of the model with each dataset are presented in Section 5.3.

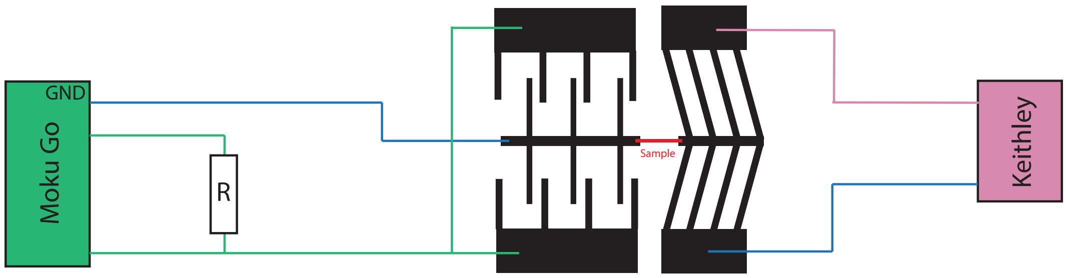

Figure 5.16: Schematic of the test-setup electrical connections. Here it is visible that, if there is a sample connecting the shuttles, the ground of the Moku:go must be floating.

5

5.2.1. Fin- and sample-point SEM measurement

The chips are mounted in a JEOL 6010LA scanning electron microscope equipped with electrical feedthrough and connected to a power supply. The measurement potential steps were implemented with large voltage steps at low setpoints and small voltage steps at high setpoints, following $V_i = V_{\max}\sqrt{i/N}$ where i is the step index and $N = 20$ the total number of steps. This spacing approximately linearizes the displacement axis, since shuttle displacement scales roughly with the square of the applied voltage, and concentrates measurement points in the region where displacement changes most rapidly. At higher setpoints the complete chip drifted visibly in the direction parallel to shuttle actuation. Because an SEM scan is not instantaneous, this drift introduces a systematic error: features at the beginning and end of a scan are imaged at slightly different positions. The fin-point measurements of chip 7, U_{7f}, were taken with the scan direction parallel to the drift direction, causing the apparent fin-point displacement to decrease at elevated currents as the device translated during the scan; this artifact is clearly visible in Figure 5.22in Section 5.3.4. This dataset was therefore excluded from the fits. All remaining measurements were performed with the scan direction perpendicular to the drift direction, so that the edge-to-edge distance between a fixed reference feature and the shuttle is measured correctly, albeit with a slight shear in the image.

The fin- and sample-point measurements were done in a SEM where an initial measurement with actuation voltage was taken and compared to the measurement at every actuation voltage setpoint. Below, in figure 5.17, two such measurements are shown; one at 0 V and one at 40 V for both measurement points. In an attempt to negate the device shifting and increase measurement ease, continuous screenrecordings were made from which displacements could be extrapolated and overlayed with the programmed voltage sweep. This method proved inaccurate, its results are shown in appendix A.

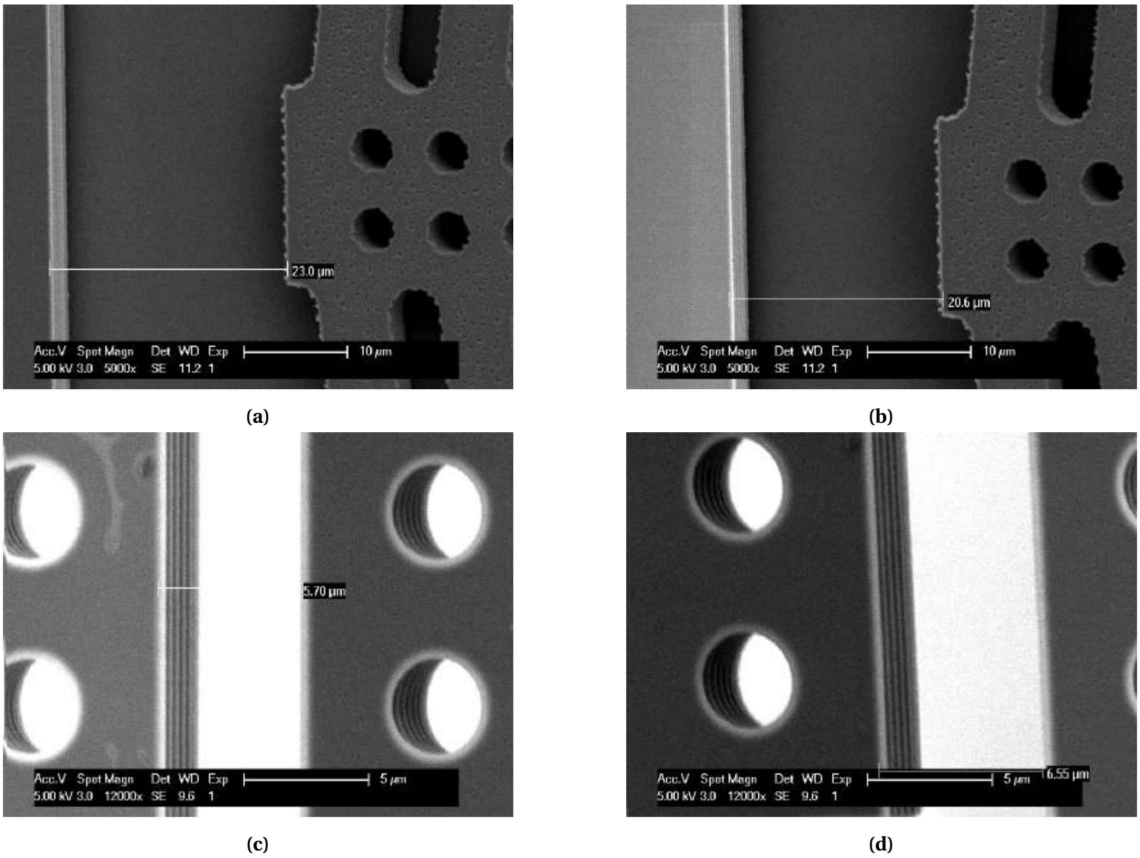

Figure 5.17: SEM images with measurements for the fin- and sample-point at 0 V and at 40 V. The current at this, high, setpoint was measured at 23 and 22.4 mA respectively.

5.2.2. Raman spectroscopy

Raman spectroscopy is used to measure the fin temperature non-invasively throughout the actuation range, providing the experimental $\Delta T(I)$ dataset required for the joint fit of Section 5.2.3. The technique exploits the temperature dependence of the silicon Raman peak: when monochromatic light illuminates a crystalline solid, a small fraction of photons scatter inelastically through exchange of energy with the lattice, either losing energy to a phonon (Stokes process) or gaining energy from a thermally excited phonon (anti-Stokes process) [89]. The energy difference between the incident and scattered photon equals the phonon energy, measured as a shift in wavenumber relative to the laser line. Silicon exhibits a prominent Raman peak at approximately 520.7 cm^{-1} at room temperature, which redshifts at elevated temperatures [90]. This shift is approximately linear with temperature up to at least 1000 °C [91], allowing temperature to be extracted directly from the measured peak position:

$$T = T_{\mathrm{amb}} + \frac{\omega_{\mathrm{meas}} - \omega_{\mathrm{amb}}}{C_{\mathrm{Stokes}}}, \tag{5.25}$$

where ω_{amb} and ω_{meas} are the Raman peak wavenumbers at ambient and working temperature, and $C_{\mathrm{Stokes}} \approx -0.0227\,\mathrm{cm}^{-1}\,{}^{\circ}\mathrm{C}^{-1}$ is the temperature calibration coefficient for silicon [92]. Each measured spectrum is fitted with a Lorentzian profile to extract ω_{meas} precisely.

Measurements were performed using a 532 nm green laser focused through a confocal Raman microscope with a spot size of approximately 1 µm. The fin temperature was probed at multiple current levels under vacuum conditions, and the measurement was repeated once under ambient pressure for reference. Some measurements were repeated due to device drift, especially present at higher setpoints.

To verify that thermal energy dissipates rapidly away from the fin array, a prerequisite for both sample integrity and correct device operation, supplementary temperature measurements at five probe points were performed at a high actuation setpoint ($I \approx 23.3\,\mathrm{mA}$); see Figure 5.18.

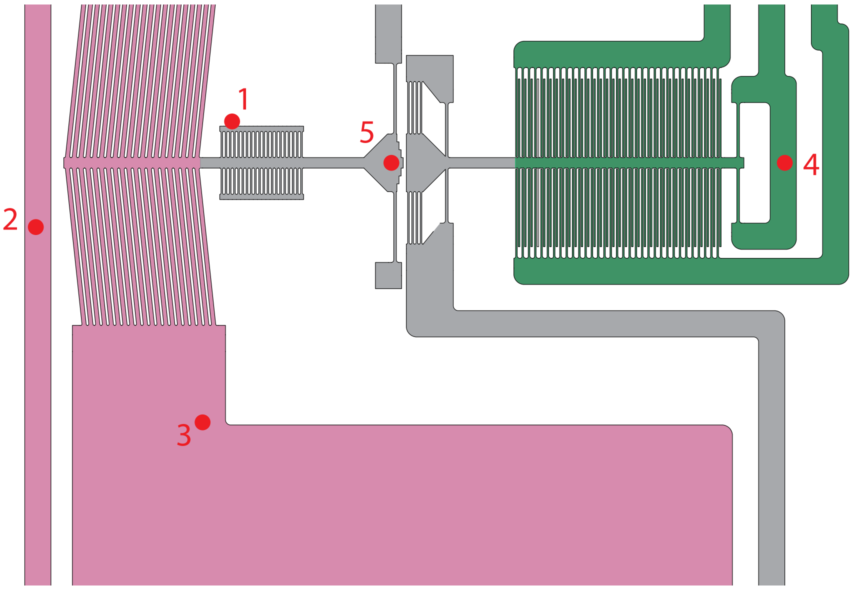

Figure 5.18: Locations of the five Raman probe points used for temperature mapping at the high actuation setpoint.

Probe point 1 is situated at the cooling flexures closest to the thermal fins, where the highest temperature among all probe locations is expected. Probe point 2 is located on one of the conductive wires; a temperature increase here is anticipated based on the resistance analysis of Chapter 3. Probe point 3 is placed at the thermal fin anchors to quantify conductive heat dissipation into the support structure; an elevated reading here is consistent with the reasoning behind $L_{\Delta T} > l_{\mathrm{th}}$. Probe point 4 is placed far from the thermal actuator to serve as a reference and to assess whether global chip heating could drive thermal expansion of the mounting fixture. Probe point 5 is located at the TAS sample point to characterize the temperature experienced by a sample during actuation. At this point, three consecutive measurements were recorded at 20 s intervals to assess whether the device had thermally stabilized.

5.2.3. Fit optimizer

The analytical models derived in Section 5.1 contain four parameters that cannot be determined from geometry alone and must be fitted to experimental data: the thermal gradient length $L_{\Delta T}$ [µm], the beam stiffness length l_b [µm], the shuttle conduction length L_s [µm], and the effective radiation area A_{rad} [mm^2]. These are determined by minimizing the discrepancy between the analytical model and two independent experimental datasets simultaneously: the Raman spectroscopy data providing the temperature–current relationship $\Delta T(I)$ (Section 5.2.2), and the SEM data providing the displacement–current relationship $U(I)$ (Section 5.2.1).

The cost function combines the mean squared error (MSE) of both datasets through inverse-variance weighting:

$$C = \frac{\mathrm{MSE}_U}{\mathrm{var}(U_{\mathrm{data}})} + \frac{\mathrm{MSE}_I}{\mathrm{var}(I_{\mathrm{data}})}, \tag{5.26}$$

where the mean squared error and variance are defined as:

$$\mathrm{MSE} = \frac{1}{n}\sum_{i=1}^{n}\left(\hat{y}_i - y_i\right)^2 \tag{5.27}$$

$$\mathrm{var}(y) = \frac{1}{n}\sum_{i=1}^{n}\left(y_i - \bar{y}\right)^2 \tag{5.28}$$

with $\hat{y}_i$ the model prediction, y_i the measured value, $\bar{y}$ the mean of the dataset, and n the number of data points. The MSE (5.27) quantifies the average squared deviation between model predictions and experimental measurements, penalizing larger errors more heavily than smaller ones. The variance (5.28) captures the spread of the data around its own mean. Dividing by the variance in (5.26) normalizes each term, so that the displacement and temperature datasets — which have different physical units and magnitudes — contribute equally to the total cost regardless of their absolute scale. A value of $C = 1$ corresponds to a model with no predictive power (equivalent to predicting the dataset mean at every point), so $C \ll 1$ indicates that the model explains the majority of variance in both datasets.

The four parameters are optimized simultaneously within the following physically motivated bounds:

$$l_{\mathrm{th}} < L_{\Delta T} < 20\, l_{\mathrm{th}}, \quad 0 < l_b < 4\,\mathrm{mm}, \quad 0 < L_s < 4\,\mathrm{mm}, \quad 0 < A_{\mathrm{rad}} < 18\,\mathrm{mm}^2. \tag{5.29}$$

These bounds reflect the extreme realistic range these parameters could be without fall outside physical the model boundaries. The bounds of the lengths and area are from minimal to the maximal possible size, the beam and shuttle length, l_b and L_s, range from zero to the distance from the furthest thermal sink to the furthest thermal fin (which is where their their impact applies), the thermal ratiation area, A_{rad}, is zero at minimum and the complete device surface at maximum, and the thermal gradient length, l_{th}, is the thermal fin length at minimum and spans to the edges of a JEOL chip at maximum.

Wide bounds are chosen to accommodate the significant differences in model predictions at initial parameter values, ensuring all, and only, physically plausible solutions are included.

The optimization is non-convex: $L_{\Delta T}$ enters both models via the effective driving temperature ΔT_{fin} ((5.10)), the average fin temperature $\bar{T}$ ((5.11)), and the conduction path length in (5.21) simultaneously. Gradient-based local methods are therefore susceptible to local minima and sensitive to the initial guess. Differential evolution [93] is a population-based global optimization algorithm that maintains a population of candidate solutions across the parameter space and refines them through mutation and crossover operations. It requires only parameter bounds rather than an initial guess or gradient information, and is specifically designed to avoid local minima. The optimization is performed independently for each of the four displacement formulae of Section 5.1.4.

5.3. Results and discussion

5.3.1. Fitted parameter values

The four free parameters enter the model through distinct physical mechanisms and their fitted values therefore carry independent physical meaning. Each parameter is discussed below in terms of its role in the model, its expected order of magnitude based on the device geometry and the Raman probe measurements, and how the optimized value compares to this estimate. The optimized values and the associated fit cost for all four actuation formulae are summarized in Table 5.1.

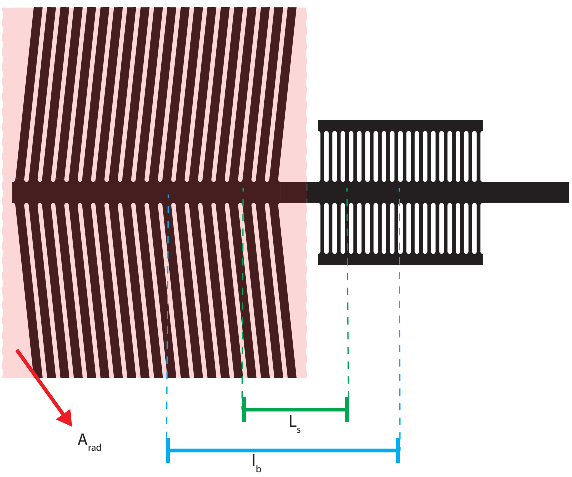

Figure 5.19: Schematic of three fitted parameters: A_{rad} is highlighted in red and describes the radiation area of the chevron actuator and extend beyond this graphic, the shuttle length, L_s over which the maximal to ambient over the shuttle, and l_b is defined as the beam length from which the beam stiffness is calculated. The fourth fitted parameter, $L_{\Delta T}$, is shown in figure 5.8.

Temperature gradient length $L_{\Delta T}$

The temperature gradient length $L_{\Delta T}$ represents the length over which the fin temperature drops from the maximum value at the shuttle end to ambient; see Figure 5.8. While in practice the temperature does not return precisely to ambient at distance $L_{\Delta T}$ from the shuttle, the parameter provides a quantitative measure of the extent to which the fin support structure heats up, and must satisfy $L_{\Delta T} > l_{\text{th}}$, where $l_{\text{th}} = 300$ µm. From probe-point measurement 3 (Table 5.2) and the arguments of Section 5.1.3, a value of $L_{\Delta T} \approx 750$µm appears physically plausible: the maximum fin temperature was approximately 600 °C and probe point 3 is located roughly 1.5 fin lengths from the shuttle, which is consistent.

Shuttle beam length l_b
The shuttle beam length l_b in (5.3) directly and exclusively controls the stiffness of the beam connecting the chevron fin array to the cooling flexures. Because both the chevron actuation force and the cooling fin stiffness are relatively high, a fraction of the actuation displacement is lost to beam deformation. A shorter beam (higher stiffness) minimizes this loss; a longer beam reduces the sample-point range of motion. The beam stiffness is evaluated using the temperature-dependent modulus $E(\bar{T})$ from (5.13) at the average fin temperature. A beam length of 300 µm is chosen which represents the distance between the centers of the chevron fins and cooling fins.

Shuttle conduction length L_s
The shuttle conduction length L_s enters the energy balance (5.21) as the effective path length over which the temperature drops from the maximum (at the thermal fins) to ambient (at the cooling fins) through the shuttle body. This length cannot be determined precisely from geometry because the true boundary condition at the cooling fins is not ambient temperature; the minimum temperature in practice rises with the actuation level. Based on the device layout, a value of $L_s \approx 150\,\mu\mathrm{m}$ is expected from direct geometric measurement.

Radiation area A_{rad}
The effective radiation area A_{rad} in 5.21 quantifies black-body radiation losses. This mechanism is negligible at low temperatures but increases rapidly at elevated temperatures due to its fourth-power dependence on absolute temperature. Assigning an accurate geometric value to A_{rad} is difficult because of the many exposed surfaces and the complex radiative exchange between closely spaced parallel fins (absorption, multiple reflections). A geometric upper bound of 400 by 500 µm or 0.2 mm^2 is estimated from the total surface area in and around the thermal actuator; the actual effective radiation area, for a device where only the thermal fins heat up, is expected to be substantially lower than this estimate.

All estimated and fitted parameter results with the fit-cost are shown in table 5.1.

Fitted parameters discussion
Several observations follow from Table 5.1. The two displacement-method formulae (Sinclair and Hugo) converge to nearly identical parameter values and both match the physical estimates closely: for both, the fitted $L_{\Delta T}$ agrees well with the estimated 750 µm, and the fitted L_s of 147 µm to 168 µm is consistent with the geometric estimate of 150 µm. This consistency across two independent displacement expressions lends confidence to the parameter values, and, more importantly, the analytical accuracy of the formulas. The fitted beam length $l_b \approx 548\,\mu\mathrm{m}$ exceeds the rough estimate of 300 µm for both formulae, which is physically expected: the model assumes the cooling flexures remain at ambient temperature, whereas in practice they heat up significantly, lowering the effective Young's modulus of the beam and requiring a longer l_b to reproduce the observed displacement loss.

	Method	$L_{\Delta T}$ [µm]	l_b [µm]	L_s [µm]	A_{rad} [mm^2]	Cost
Sinclair	Displacement	728	547	168	0.810	0.098
Hugo		751	548	147	0.850	0.10
Espinoza	Force	1460	542	41.7	0.986	0.10
Ratio		>6000	536	24.5	1.18	0.12
Rough estimates		750	300	150	<0.20	—

Table 5.1: Optimized parameter values for all four actuation formulae together with rough physical estimates.

The force-method formulae behave differently. The Espinoza formula converges to $L_{\Delta T} \approx 1460\,\mu\text{m}$, roughly twice the physical estimate, while the ratio formula diverges entirely, with $L_{\Delta T}$ exceeding 6000 µm and hitting the upper bound. Both force formulae also converge to unrealistically short shuttle conduction lengths ($L_s < 50\,\mu\text{m}$), far below the geometric estimate. This behavior is consistent with the force formulae overestimating the fin-point displacement at intermediate temperatures: to compensate, the optimizer inflates $L_{\Delta T}$, which reduces ΔT_{fin} via (5.10) and suppresses the predicted force, while simultaneously driving L_s to a negligible value to maintain the current-temperature fit. Despite these compensating distortions, the fit costs of all four formulae are comparable ($C \approx 0.10$–0.12), indicating that similar total residuals can be achieved through physically implausible parameter combinations in the force method.

The effective radiation area A_{rad} is substantially larger than the geometric estimate for all four formulae, ranging from 0.81 mm^2 to 1.18 mm^2 against an estimated upper bound of 0.20 mm^2. This is physically consistent with the probe-point measurements of Table 5.2, which show that several locations around the thermal device reach several hundred degrees Celsius during actuation: the effective radiating area is not limited to the fin surfaces but includes the surrounding heated structure. It should be noted that all probepoints, except probe point 4, are located relatively close to the thermal actuator and could thus be heated through the actuator and not the conductive wires. However, probe point 4 is located far from the thermal actuator and not on an active conduction path. The elevated temperature at probe point 4 shows that the complete chip heats up, this could never be caused solely by the heat generated through the thermal actuator. Simulations with ambient temperature boundary conditions at the fin supports and thermal sinks showed that the temperature at probe point 5 and 4 should not increase throughout the complete actuation range. Based on the foregoing, Hugo's displacement formula is considered the more physically reliable of the four, and its parameter values are used in the remainder of this chapter.

All plots in the next subsections (sections 5.3.2, 5.3.4, 5.3.5, and 5.3.6) include the estimated results of all equations and Hugo's displacement results with fitted parameters. In these plots, the implications of the four parameters and the differences between the four different calculation methods are visualized.

5.3.2. Drive current and fin temperature

Figure 5.20 shows the Lorentzian fits to the measured spectra at all actuation setpoints; the progressive peak shift with increasing current is clearly visible.

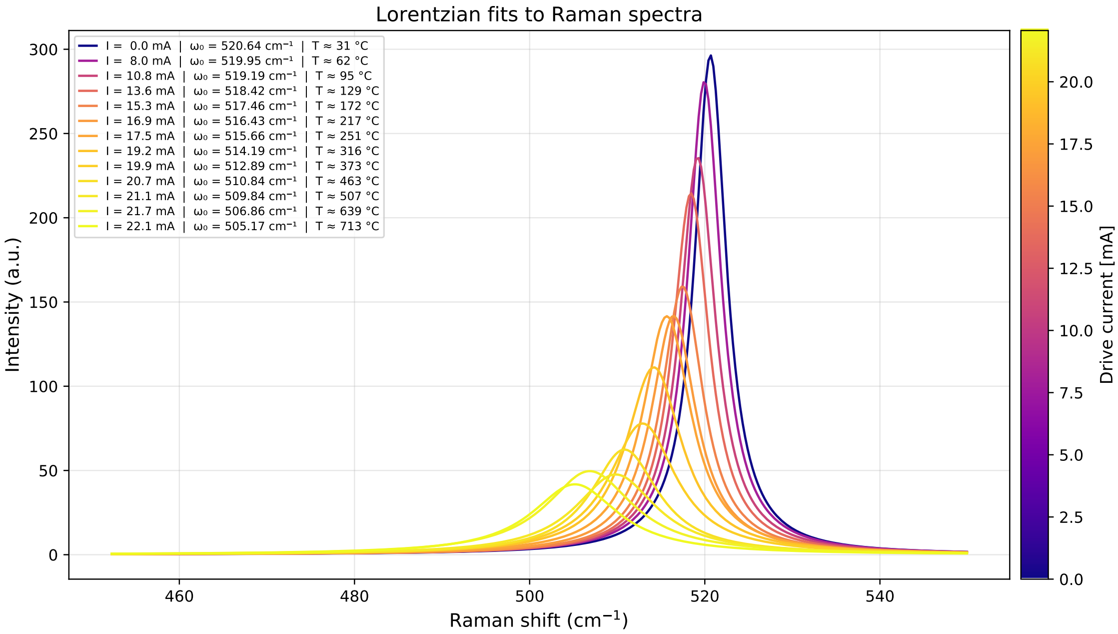

Figure 5.20: Lorentzian fits to the Raman intensity spectra at successive actuation setpoints. All measurements are labeled with the respective actuation current, measured peak shift, and calculated temperature.

The peak positions at all setpoints and for all chips are converted to temperatures via (5.25). The analytical model is then fitted to these data as described in Section 5.2.3; the results are shown in Figure 5.21. The ambient-pressure dataset is included to illustrate the considerably higher actuation current required to reach the same fin temperature compared to vacuum operation, a direct consequence of the additional convective heat loss present at ambient pressure that is absent under vacuum.

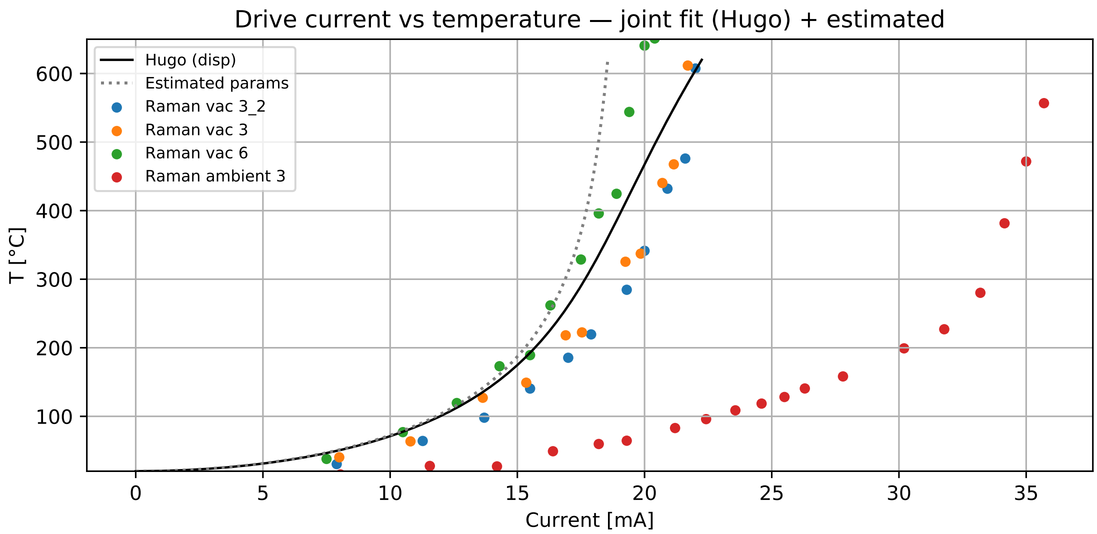

Figure 5.21: Drive current versus fin temperature for all chips and measurement conditions, together with the four fitted analytical curves and the unoptimized reference.

5.3.3. Probe-point temperatures

The measured probe-point temperatures for two test chips are summarized in Table 5.2.

	1	2	3	4	5		
					$t = 0\,\mathrm{s}$	$t = 20\,\mathrm{s}$	$t = 40\,\mathrm{s}$
Test chip 3	248 °C	300 °C	254 °C	230 °C	251 °C	280 °C	278 °C
Test chip 6	230 °C	310 °C	245 °C	233 °C	238 °C	262 °C	270 °C

Table 5.2: Raman probe-point temperatures at high actuation setpoint ($I = 23.3\,\mathrm{mA}$) for two test chips.

Several observations follow from Table 5.2. The conductive wires (probe 2) reach the highest temperature of all probe locations at approximately 300 °C, confirming significant resistive heating of the electrical connections. The fin anchors (probe 3) and the cooling flexures (probe 1) both exceed 230 °C, consistent with the large $L_{\Delta T}$ values fitted in Section 5.3.1 and confirming that the thermal gradient extends well beyond the physical fin length. The reference probe (probe 4), located far from the actuator, also registers approximately 230 °C, suggesting that global chip heating is non-negligible and may contribute to the observed device drift during actuation. At the sample point (probe 5), the temperature is 270 °C to 280 °C and stabilized within the 40 s observation window, indicating considerable and problematic sample heating.

5

5.3.4. Fin- and sample-point displacement

Now the data is compiled and fitted, and the result is shown in Figure 5.22.

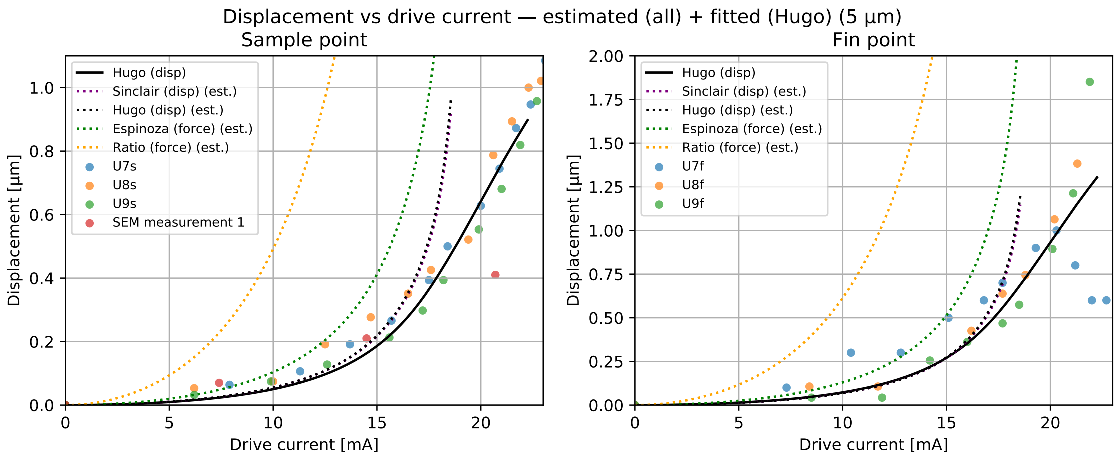

Figure 5.22: Displacement versus drive current measured in the SEM at the sample point (left) and fin point (right) for chips 7, 8, and 9. The solid curve shows the Hugo fitted formula; dotted curves show all four formulae evaluated at the estimated parameter values (Table 5.1). The U_{7f} dataset was excluded from the fits because the scan direction was parallel to the device drift direction, causing an apparent reduction in displacement at elevated currents.

5.3.5. Displacement and fin temperature

The displacement–temperature relationship is obtained directly from the analytical model: the Hugo displacement formula is evaluated over the full range of ΔT using the optimized parameters from Table 5.1. The temperature axis represents the fin tip temperature rise $\Delta T = T_{\text{max,abs}} - T_{\text{amb}}$, which is the actuation temperature used throughout the model.

Two sets of scatter data are overlaid for validation. The SEM displacement measurements are plotted at the temperatures obtained by inverting and interpolating the Hugo fitted $I(\Delta T)$ curve. The Raman temperature measurements are plotted at the displacements obtained from the Hugo fitted $U(I)$ curve evaluated at the corresponding drive currents. Both conversions use the same fitted model, so any deviation of the scatter points from the analytical curve reflects genuine discrepancy between the model and the data rather than approximation error in the conversion.

The resulting curves are, as expected, approximately linear over the actuation range: the dominant term in the force expressions scales linearly with ΔT_{fin} via (5.10), and the temperature dependence of α and E introduces only a mild nonlinearity over this range.

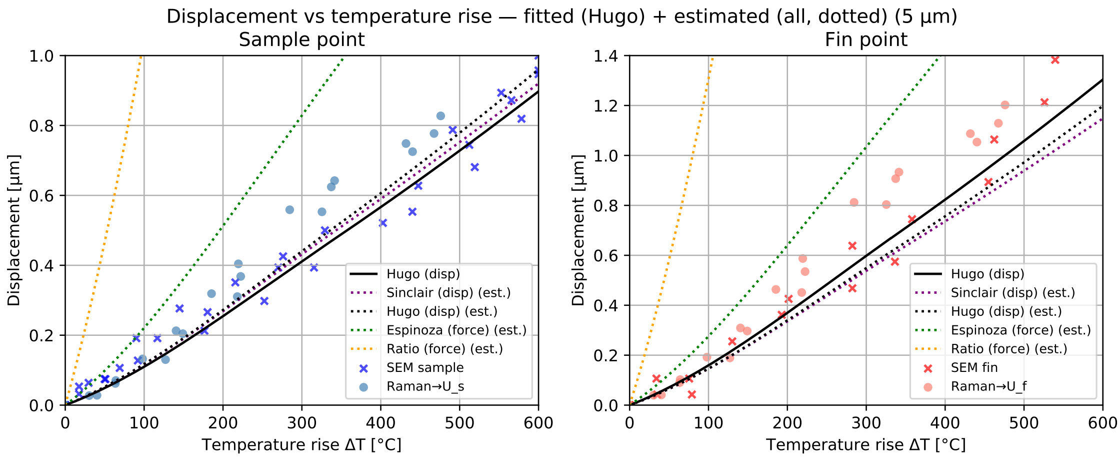

Figure 5.23: Displacement of the sample- and fin-point versus temperature rise of the thermal actuator fins for all four fitted formulae, together with SEM scatter data (converted via the empirical $T(I)$ mapping) and Raman-derived scatter data.

5.3.6. Electrical path resistance

The total measured circuit resistance exceeds the analytical fin resistance $R_{f,\text{tot}}$ from (5.22) by an amount that includes the resistance of the conductive wires and contact resistances. If the chip wires remain at approximately ambient temperature, this combined conductive path resistance should stay constant across the actuation range. It is extracted at each measurement point via:

$$R_{\text{cond}} = \frac{V_{\text{pr}}}{I} - R_{f,\text{tot}}, \tag{5.30}$$

where V_{pr} is the measured actuation voltage and I the drive current. $R_{f,\text{tot}}$ is the analytical fin resistance from (5.22), evaluated using the Hugo fitted parameters of Table 5.1. Since $R_{f,\text{tot}}$ is used as the reference, any deviation of R_{cond} from a constant value reflects changes in the external circuit rather than in the fins themselves.

Figure 5.24 shows the measured voltage–current characteristics together with the analytical prediction, and the conductive path resistance extracted from (5.30).

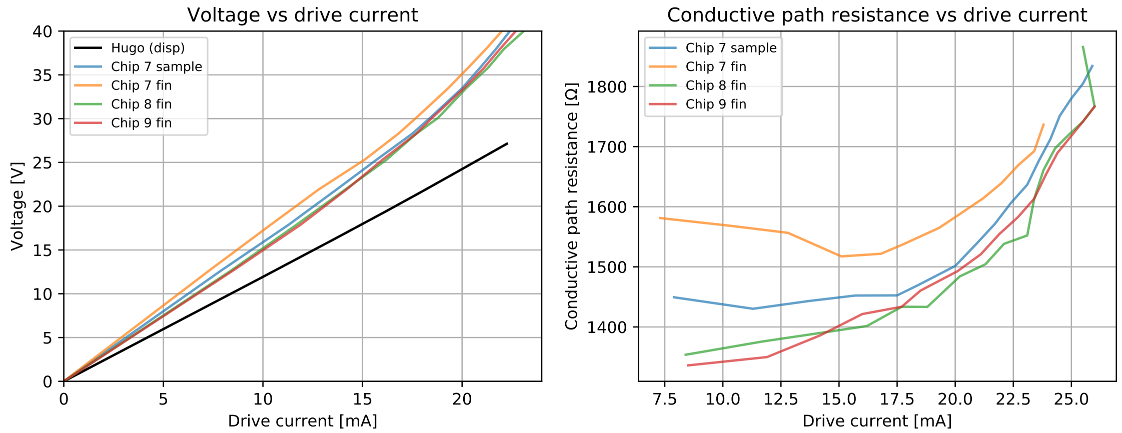

Figure 5.24: Left: measured voltage–current characteristics for four devices compared with the fitted analytical characterization, including the expected conductive path resistance. Right: conductive path resistance R_{cond} calculated from (5.30) for the same four measurements. All tested chips are 5 µm thick TFS devices.

Two observations follow from Figure 5.24. First, at the lowest actuation levels the extracted path resistance is approximately 1450 Ω. This is consistent with the predicted conductive path resistance of 1040 Ω (Table 3.1 in Chapter 3) plus additional pin contact and setup cable resistances R_c between power supply and chip-wires. Second, R_{cond} rises noticeably with drive current over the full actuation range, confirming that the conductive wires heat up. This is consistent with the elevated temperature measured at probe point 2 in Table 5.2.

5.4. Limitations and proposed improvements

The analytical and experimental characterization of the electrothermal device contains several simplifications and shortcomings, which are collected here.

Linear temperature profile The fin temperature profile is approximated as linear over the heated fin (Section 5.1.3). In practice the profile is closer to parabolic under vacuum, and the boundary conditions assumed in the standard derivation, where both fin ends are held at ambient temperature, do not hold here. Each thermal fin connects to the TAS, which heats up considerably during actuation, while the anchor ends conduct heat into a support structure that itself reaches elevated temperatures (probe points 1, 3, and 4 in Table 5.2). The fitted gradient length $L_{\Delta T}$ absorbs part of this discrepancy, but a piecewise or coupled-domain thermal model including the support structure and conductive wires would describe the device more accurately.

Beam temperature assumption The shuttle segment connecting the chevron fins to the cooling flexures is evaluated at the average fin temperature in (5.13), implicitly assuming that the cooling flexures maintain their anchors at ambient. In practice the cooling flexures heat up to roughly half the maximum fin temperature (probe 1, Table 5.2), lowering the effective Young's modulus along the beam. This is the most plausible reason the fitted $l_b \approx 548\,\mu m$ exceeds the geometric estimate of 300 µm (Section 5.3.1).

Conductive wires in the energy balance The power balance (5.21) attributes all dissipated power $I^2 R_{f,\mathrm{tot}}$ to the thermal fins, but probe 2 (Table 5.2) and the extracted path resistance R_{cond} (Section 5.3.6) both confirm that, at higher setpoints, the conductive wires reach several hundred degrees Celsius and dissipate a non-negligible fraction of the input power outside the actuator. Including this wire dissipation explicitly would feed back into the fitted parameters, particularly $L_{\Delta T}$ and A_{rad}, which currently absorb the discrepancy. This limitation disappears for devices that include the Mo conductive layer.

Selection of actuation force formula Of the four candidate formulae, only Hugo's and Sinclair's displacement formulae yield physically plausible fitted parameters (Section 5.3.1); the two force-method formulae diverge or hit their parameter bounds. Hugo's is used throughout this chapter, but the four formulae give similar total fit costs ($C \approx 0.10$–0.12), so the selection is partly empirical. Independent measurement of one or more of the fitted parameters, particularly the temperature gradient length $L_{\Delta T}$, would resolve this.

5

Missing molybdenum conductive layer The tested devices were produced without the Mo conductive layer (Chapter 3). Without Mo, the actuation current flows entirely through the doped silicon device layer, raising the conductive path resistance and dissipating a significant fraction of the input power outside the thermal actuator. This results in: elevated wire temperatures (probe 2, around 300 °C), sample-point heating (probe 5, 270 °C to 280 °C), and visible device drift caused by thermal expansion of the chip holder and chip (Section 5.2.1). At high actuation levels, this risks damaging the holder. Devices with the intended Mo layer are expected to behave very differently and should be tested as the next step.

In-plane shuttle deformation The beam connecting the chevron fin array to the cooling flexures strains during actuation (Figure 5.5). This strain causes actuation-range losses at the sample point and complicates the actuation regime analysis. The effect could be reduced by decreasing the cooling-flexure stiffness, which must be balanced against the corresponding rise in sample-point temperature, and by increasing the beam width to raise its axial stiffness.

Limited measurement dataset All fits in this chapter use 5 µm TFS devices without samples. Functional 20 µm devices (Chapter 3) and measurements with samples of known stiffness would provide additional constraints on the fitted parameters, allow the lumped-model prediction for U_{LS} to be tested directly, and quantify fabrication-induced variation across nominally identical devices.

In summary, the dominant practical limitation is the missing Mo conductive layer, which drives several other issues (wire heating, sample heating, and device drift) and which counteracts the standard energy-balance assumption that all input power is dissipated in the fins. The main analytical extension is a coupled thermal model including the conductive wires and support structure. Both would be addressed on Mo-coated devices that includes the 20 μm variants and samples of known stiffness.

6
Tensile tests

Following the characterization of both electrostatic and electrothermal MEMS devices in Chapters 4 and 5, this chapter presents preliminary tensile testing experiments. While the ultimate objective of these devices is to perform stress-strain and biasing experiments inside a TEM, this thesis focuses on proving and comparing their functionality.

Two sample types are investigated: silicon lamellae and few-layer graphene membranes. Silicon lamellae, commonly used for device characterization and mechanical testing, exhibit well-characterized stress-strain behavior and serve as a validation standard. Few-layer graphene membranes represent a more challenging test case: their atomic thickness, exceptional mechanical properties, and sensitivity to structural defects make them both scientifically interesting and technically demanding. Each material is described in its own section, including mechanical properties, preparation methods, and transfer protocols.

Given the exploratory nature of this work and challenges inherent in sample handling at the microscale, measurement quality is expected to be limited. The primary goal is feasibility demonstration rather than precision mechanical characterization.

6.1. Graphene

Graphene is a two-dimensional material consisting of a single layer of carbon atoms arranged in a hexagonal lattice, see figure 6.1. First isolated in 2004 by Geim and Novoselov [94], building on earlier theoretical work by Wallace [95], graphene exhibits exceptional mechanical properties: Young's modulus of approximately 1 TPa, tensile strength exceeding 130 GPa, and breaking strain near 25% [1]. These properties, combined with high electrical and thermal conductivity [2], [3], make graphene a promising material for applications ranging from flexible electronics to composite reinforcement.

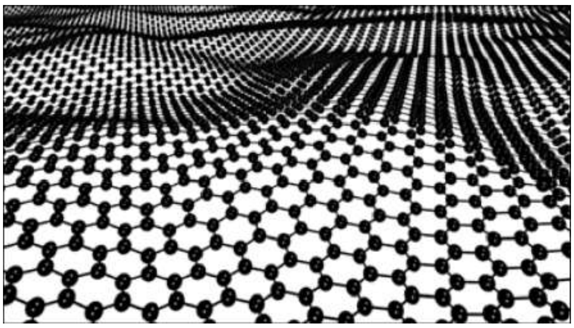

Figure 6.1: Visualisation of single layer graphene [5]

However, practical implementation is limited by topographical defects (ripples, wrinkles, and grain boundaries) influencing mechanical, electrical, and chemical properties [5]. Understanding the relationship between structural imperfections and mechanical behavior requires *in situ* observation during straining, making TEM-based tensile testing particularly valuable. The atomically thin nature of graphene (0.335 nm single-layer thickness [96]) permits direct imaging of structural evolution under load, including crack propagation, slip mechanisms, and grain boundary behavior [29]. The samples in this thesis consist of few-layer graphene. While the PPC dry transfer method is capable of transferring few- to single-layer graphene [97], thicker few-layer samples were selected for mechanical testing due to their increased mechanical robustness during handling and EBID attachment.

Testing graphene membranes on the fabricated MEMS devices serves two purposes. First, it provides a proof-of-concept for two-dimensional material testing, demonstrating compatibility with thin samples requiring careful handling. Second, successful graphene testing validates the measurement sensitivity.

6.1.1. Transfer process

Two primary approaches for attaching 2D membranes to MEMS devices exist: wet transfer and dry transfer, illustrated in Figure 6.2.

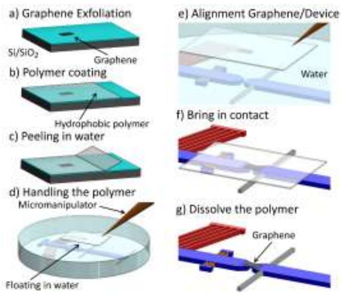

(a)

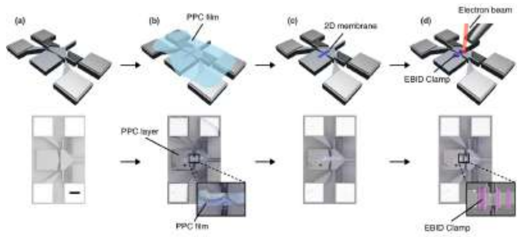

(b)

Figure 6.2: Comparison of both wet and dry transfer processes, from [82] and [63] respectively.

Wet transfer involves floating the graphene membrane (typically grown on copper foil via Chemical Vapor Deposition (CVD) or mechanically exfoliated onto a sacrificial substrate) in deionized water or dilute acid solution after etching the underlying substrate. Using a nanoindenter, the floating membrane is then positioned above the target device, and the liquid is allowed to dry [98], gently lowering the membrane in place. While well-established for transferring graphene onto flat substrates, this method presents significant challenges for MEMS devices with comb or suspended structures. Submersion and subsequent evaporation can cause stiction due to capillary forces particularly problematic for comb-drive actuators with narrow gaps (~ 2 μm in this case) [40]. Stiction can be mitigated through critical point drying (CPD), which eliminates the liquid-vapor interface by transitioning through the supercritical phase of CO_2, thereby avoiding surface tension forces [99]. However, CPD requires specialized equipment and introduces additional process complexity.

Dry transfer circumvents liquid-handling challenges entirely. The technique employs a sacrificial PolyCarbonate (PC) or PolyPropylene Copolymer (PPC) film that exhibits strong adhesion to two-dimensional materials [97]. As illustrated in Figure 6.3, the process proceeds as follows. First, graphene is mechanically exfoliated from HOPG (Highly Oriented Pyrolytic Graphite), then, placed on a PolyDiMethylSiloxane (PDMS) square attached to a glass microscope slide. After careful selection, a sample is chosen and picked up using a PDMS dome attached to a glass slide. Given the transparency of the PDMS, the dome is used as a lens during this process. This PDMS dome is covered with a thin layer of sacrificial PPC. After lift-off, the sample is placed over the sample gap and the temperature of the chip is increased to melt this PPC film. The melting point of the PPC is lower than that of the PDMS dome, thus when moving the PDMS dome up, a layer of (molten) PPC is left behind including the sample.

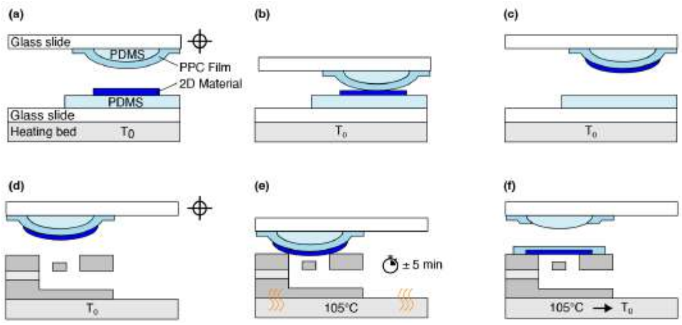

Figure 6.3: Schematic representation of the membrane transfer procedure with sacrificial PPC film. a) precise positioning of PDMS dome above the 2D material using microscope. b) and c) showing the contact and picking up of the sample. d) shows the repositioning of the dome, with sample, above the gap on the device after which, in (e), contact is made to transfer the sample at 105 °C to detach the PPC film from the PDMS dome. Finally, in (f), the material is left behind on the chip with the PPC film on top [63]

Finally, the PPC is removed by vacuum annealing (2.5 hours at 300 °C), decomposing the polymer and leaving only the graphene membrane [63].

The dry transfer method offers several advantages for MEMS compatibility: (1) no liquid contact with the device, eliminating stiction risk; (2) precise positioning control through optical feedback; (3) minimal contamination if proper vacuum annealing is performed. All graphene samples tested in this work were transferred using the dry method. The downside of the dry method relates to the fragility of the devices as the placing of the sample requires precise and careful sample movement. This transfer process for the 5 µm thick devices proved to be difficult given the low (out of plane) stiffnesses.

Following transfer, the graphene membrane is attached to the device through van der Waals adhesion alone. These adhesion forces are insufficient for mechanical testing as tensile forces would cause membrane slippage or detachment. Improved attachment is achieved through Electron Beam-Induced Deposition (EBID), a nanofabrication technique that deposits solid material at targeted locations.

In EBID, a focused electron beam (1–30 keV) interacts with a precursor gas (commonly organometallic compounds such as methylcyclopentadienyl platinum trimethyl, $MeCpPt(Me)_3$) introduced into the specimen chamber [100] through a nozzle. The electron beam dissociates precursor molecules at the beam impact point, depositing the metallic component while volatile byproducts are pumped away. The deposited material effectively "welds" the graphene membrane to the device surface [101].

After EBID attachment, the samples are ready for testing.

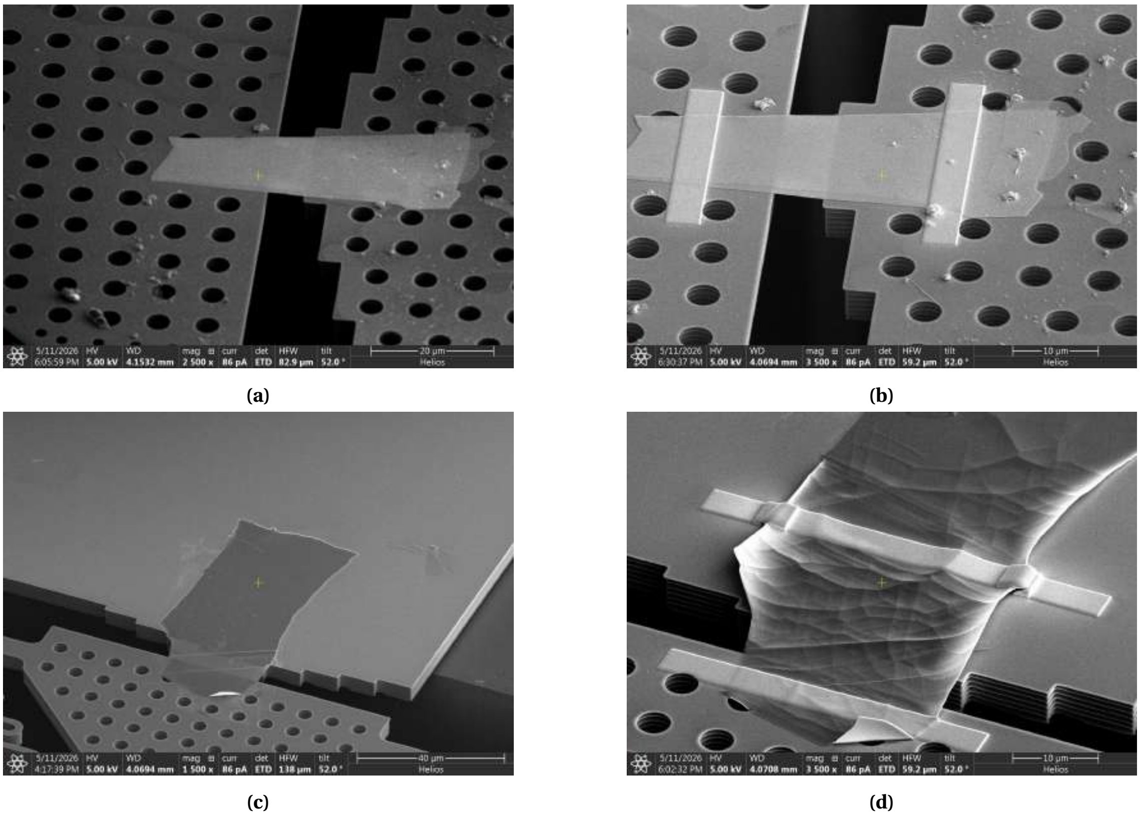

Figure 6.4: SEM images of an electrothermal, top, and electrostatic, bottom, device before, left, and after, right, EBID. The deposited material is platinum with a thickness of 200 nm, a width of 4 µm, and a length extending 5 µm from the edge of the sample on both sides.

6.1.2. Test results

From both devices only the electrothermal device could be used because, for the electrostatic device, the shuttle was found to be stuck to the handle wafer rendering it unusable (see subsection 4.1.6 for more info on stiction). One tensile test with a graphene sample was performed, some images from the testing are included below (figure 6.5):

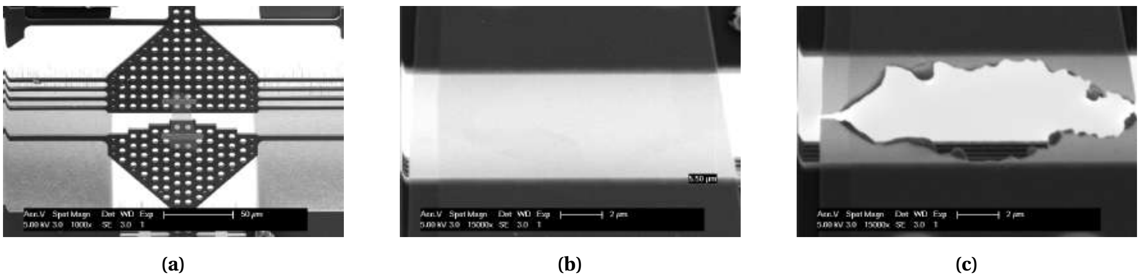

Figure 6.5: Three images from the tensile tests with an electrothermal (5 µm thick) device. The first image shows an overview of the sample placed and glued on the shuttles. The second and third images show the graphene before and after tensile testing.

The displacement was measured through the capacitive fins and through measuring the load shuttle displacement and sample elongation with SEM images at every setpoint. Applying a voltage over the chevron fins visibly actuated the TAS with the graphene pulling on the LS, also moving it. The initial sample gap was taken as the distance between the platinum anchors. At an actuation current of 18 mA, the graphene broke and the load shuttle moved towards its unactuated state. Below plots show the acquired data, figure 6.6;

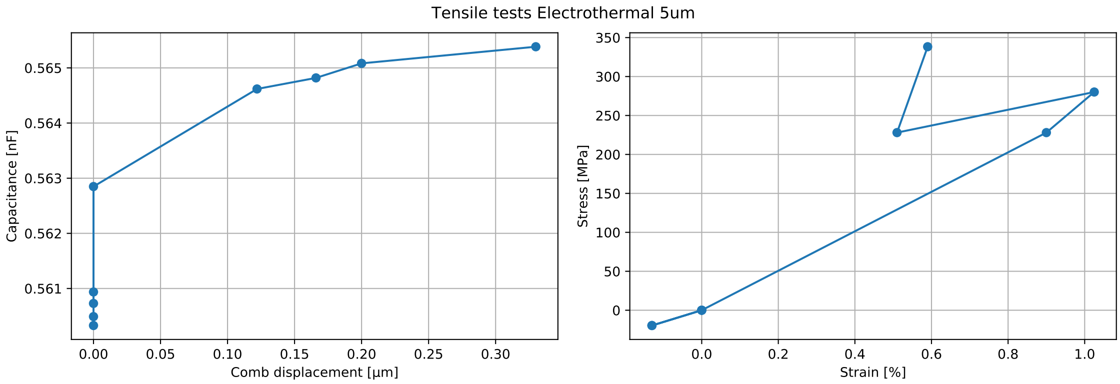

Figure 6.6: Capacitance change with comb displacement results for a 5 micron electrothermal device with graphene sample on the left. On the right the stress strain results for this graphene sample.

6.1.3. Discussion results

Despite the limited dataset of a single tensile test, several observations can be drawn. The graphene sample did experience stress during actuation, evidenced by the load shuttle displacement and the eventual fracture of the sample at a drive current of 18 mA, after which the load shuttle returned to its unactuated position. The measured stress values were, however, inaccurate or minimal, which is attributed primarily to difference between the initial sample gauge length and the initial sample gap: because the gauge length is considerably larger than the gap, the achievable strain is reduced by a corresponding factor.

The capacitance measurements proved insufficiently accurate to resolve the small displacements involved, consistent with the expectations set out in Section 5.3. No reliable displacement–capacitance relationship could be established from the present data.

An additional concern relates to the electrical boundary conditions of the measurement. Under actuation, the TAS is brought to approximately half the total actuation voltage. If the Moku:go does not employ a floating ground, a potential difference across the graphene sample could drive a leakage current through it. No such leakage current was detected during the measurement, though this does not definitively rule out the possibility.

As observed during the initial actuation tests (Section 5.3), the complete device shifts with increased actuation currents, and thus heat. The combination of this shift and the scanning direction of the SEM introduced systematic errors in the displacement measurements, particularly at the sample gap where the absolute displacement is smallest. The fracture morphology of the graphene was atypical of a straightforward tensile failure, which may be related to the elevated temperature at the sample location or to the aforementioned electrical boundary conditions.

To improve the reliability of future tests, the actuation voltage should be applied across both sides of the chevron fins, with the TAS grounded through one of the biasing contacts; this eliminates any floating potential at the sample. Rotating the chip by 90° relative to the SEM scan direction would reduce the apparent shift in the images, though it would not eliminate the underlying mechanical drift entirely. Increasing the number of repeat tests and sample types is necessary to assess the consistency of the results and to build a statistically meaningful dataset.

In addition, when examining the load shuttle fins after all transfer steps (see figure 6.7), it is clear that these are deformed. The extent of this deformation is such that the accuracy and correctness of the capacitance measurements is severely jeopardized. This on top of the expected capacitance measurement accuracy already being minimal.

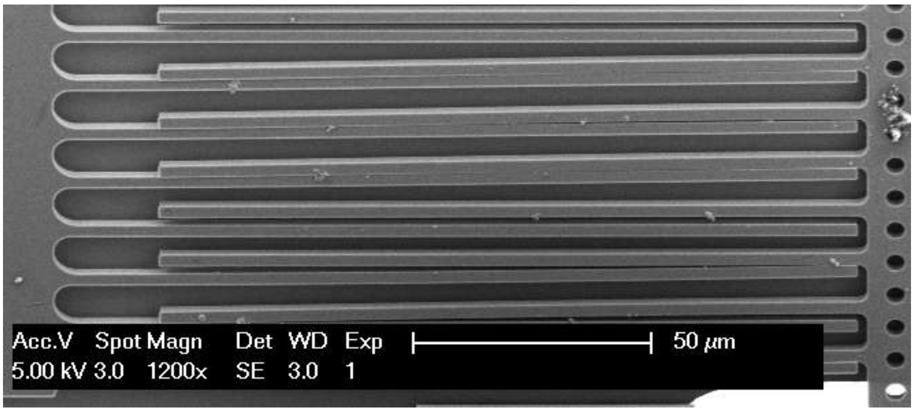

Figure 6.7: Image of the LS fins after all transfer tests showing that the comb fins are deformed and in some cases seemingly touching. It must be noted however that no leakage current was measured when applying a potential over the fins.

6.2. Lamella

A lamella is a thin, electron-transparent membrane extracted from bulk material using focused ion beam (FIB) milling. Typical dimensions are 10–15 μm in length, 5–8 μm in height, and 100–500 nm in thickness [102], [103]. This geometry provides a free-standing cross-section suitable for *in situ* mechanical testing under transmission electron microscopy.

6.2.1. Transfer process

Lamellae prepared by FIB lift-out offer several advantages for nanomechanical testing. The technique enables precise control of extraction location, crystallographic orientation, and specimen dimensions from thin films, coatings, or complex microstructures where conventional sample preparation cannot be readily employed [102], [104]. The controlled geometry and small specimen volume (< 1 μm^3) satisfy both the mechanical requirements of nanoscale testing stages and the electron-transparency requirements for SEM and TEM observation of deformation mechanisms [103], [105].

The lamella preparation process consists of three main stages, illustrated in Figure 6.8 [103]. First, a protective metal layer is deposited on the surface region of interest through two steps: initial electron-beam deposition of a thin metal layer (typically 50–100 nm) prevents surface damage during subsequent processing, followed by ion-beam deposition of a thicker protective cap (1–2 μm) [102], [106]. Second, the lamella is cut out by FIB milling: trenches are cut on both sides and beneath the region to create a freestanding membrane attached at one end. A nanomanipulator needle is then welded to the lamella using EBID, and the final attachment is severed to lift out the specimen [102], [103]. Third, the lamella is transferred to the MEMS device and welded in place using localized metal deposition. The membrane is thinned by FIB milling from both sides until the target thickness is achieved (typically 100–200 nm for TEM transparency, or 200–500 nm for mechanical testing) [102], [103], [107].

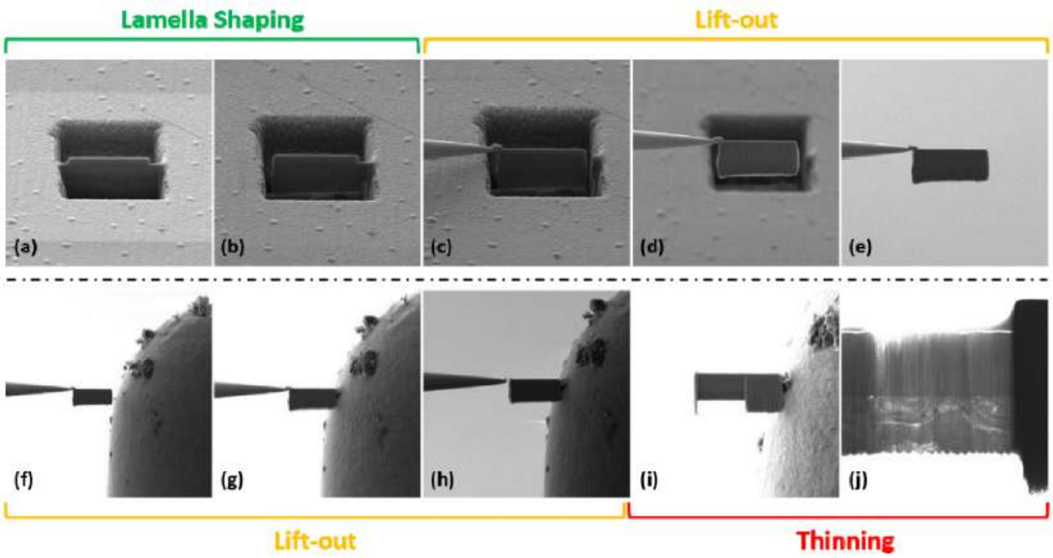

Figure 6.8: FIB milling and thinning [102]

The lamella used for tensile testing in this work is shown in Figure 6.9: its placement across the gap between the electrothermal device shuttles, a plan-view image with its in-plane dimensions, and a cross-section with its thickness. These devices where prepared by one of DENS' collaborators at the Technical University Darmstadt under supervision of Prof. Dr. Molina-Luna from the Advanced Electron Microscopy subdivision.

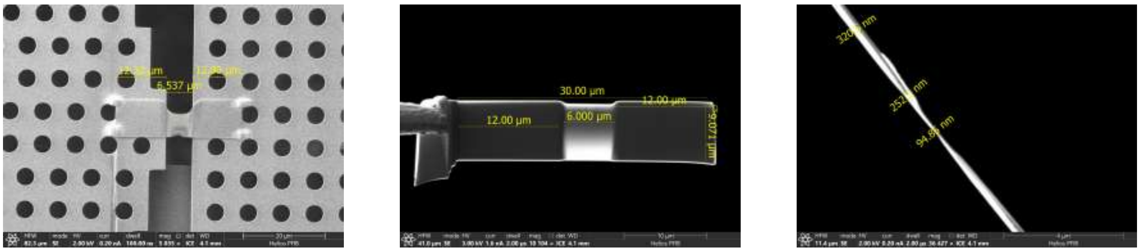

(a) (b) (c)

Figure 6.9: Three images of the lamella used for tensile testing: (a) the lamella placed over the gap between the thermal device shuttles (TAS and LS), (b) a plan-view image with in-plane dimensions, and (c) a cross-section with thickness. These pictures where taken at TU Darmstadt for DENSsolutions.

The expected stress–strain response of the silicon lamella can be calculated from the measured displacement and known geometry. For uniaxial tensile loading, the engineering stress σ and engineering strain ε are:

$$\sigma = \frac{F}{A_0} = \frac{k_s \Delta U_s}{w\,t} \qquad (6.1) \qquad\qquad \varepsilon = \frac{\Delta U_s}{L_0} \qquad (6.2)$$

where F is the applied force, $A_0 = w\,t$ is the initial cross-sectional area, ΔU_s is the measured sample elongation, L_0 is the initial gauge length (the sample gap distance), k_s is the sample stiffness, w is the lamella width, and t is the lamella thickness. The elastic modulus then follows from the linear portion of the stress–strain curve:

$$E = \frac{\sigma}{\varepsilon} = \frac{k_s L_0}{w\,t}. \qquad (6.3)$$

Silicon exhibits elastic anisotropy, with Young's modulus varying with crystal orientation. For single-crystal silicon, $E_{\langle 100\rangle} \approx 130\,\mathrm{GPa}$, while $E_{\langle 110\rangle} = E_{\langle 111\rangle} \approx 169\,\mathrm{GPa}$ [13]. Knowing the Young's modulus, cross-sectional area, and gauge length of the sample therefore allows the expected stiffness, and hence the device response, to be predicted. For the lamella in Figure 6.9, with $L_0 = 6\,\mu\mathrm{m}$, $w = 9\,\mu\mathrm{m}$, and $t = 95\,\mathrm{nm}$, assuming $\langle 110\rangle$ orientation and that the sample remains at ambient temperature, the expected stiffness is:

$$k_s = \frac{E\,w\,t}{L_0} \approx 24\,\mathrm{kN\,m^{-1}}. \qquad (6.4)$$

6.2.2. Test results

Tensile testing of the lamella was not carried out within this thesis, both due to time constraints and because lamella testing is supplementary to the main focus of this work, the characterization and comparison of the two device types. The preparation and mounting described above, together with the expected stiffness of (6.4), are nonetheless included as a starting point for follow-up work; the actual tensile measurement on the mounted lamella is therefore deemed future work (Section 7.2).

7 Discussion

This chapter brings together the findings from Chapters 4, 5, and 6. Each device chapter ended with its own *Limitations and proposed improvements* section, in this chapter the general improvements and limitations applicable for both devices are described. The functionality of both devices as they are now and as they could be including the improvements are compared.

7.1. Limitations and proposed improvements

The device-specific limitations are collected in Sections 4.4 and 5.4. Several issues are common to both devices and are summarized here.

Missing molybdenum conductive layer The tested devices were produced without the intended Mo layer on the conductive wires (Section 3.2). For the electrostatic device this has no direct consequence, as the actuation currents are negligible. For the electrothermal device, the consequences are substantial: only a small part of the input power is dissipated in the fins, the surrounding chip heats up significantly (Table 5.2), the sample point itself rises to 270 °C to 280 °C (probe 5), and the assumption underlying the energy balance (5.21), that all input power dissipates in the fins, is partially violated. Testing the Mo-coated devices would thus solve most issues encountered during testing and characterizing.

Device thickness The 20 µm devices could not be tested due to incomplete frontside DRIE (Section 3.2). For the electrostatic device, a fourfold increase in thickness would increase the comb capacitance and the force by roughly the same factor, pushing the device signal well above the present noise levels of the capacitance measurements (Section 4.3.2), and would substantially raise the out-of-plane stiffness, suppressing the handle-wafer-stiction failure mode (Section 4.1.6). For the electrothermal device, the trade-off is less one-sided: the load shuttle becomes stiffer, which shifts the optimal sample stiffness upward (Figure 5.15) and reduces the device's suitability for ductile samples. For both devices, the increased in- and out-of-plane stiffness increase would increase the yield of functional devices during production, handling, and sample transfer.

DRIE sidewall characterization The scallop depth b, the scallop inclination angle, and the mask undercut w_C all enter the in-plane stiffness, the comb capacitance, and the actuation force (Section 4.1.2), yet all three were taken from literature ranges rather than measured on the present devices. Visual inspection suggests that the assumed mask undercut underestimates the actual value. Cross-sectional SEM imaging of the etched sidewalls, combined with a COMSOL fit of these geometric parameters to a wider voltage–displacement dataset, would remove a major source of uncertainty in the electrostatic device model and slightly tighten the electrothermal one. Enlarging the mask features by the anticipated undercut, would make sure the released devices match the nominal design dimensions.

Sample transfer and residual forces The dry-transfer process (Section 6.1) leaves residual in-plane forces of unknown direction on the shuttles after attaching the samples. The electrostatic device, designed for low in-plane stiffness, is more affected: in several cases the shuttle was visibly pulled and twisted by the sample, and, was in extreme cases enough to bring the comb fins into contact. Beyond the immediate stiction risk, any non-axial component of this residual force makes the imposed strain non-uniaxial and affects the stress–strain interpretation. A wet transfer (Figure 6.2) with critical point drying would provide cleaner samples with better-controlled thickness and orientation, at the cost of additional process complexity.

7.2. Future work

Beyond the improvements above, several subjects remain to be researched.

In-situ TEM testing of mounted samples was not possible during this thesis because no compatible holder was available; this is what the devices were designed for and should be performed once a holder is in place. TEM testing with these devices could help in characterizing the structure of graphene and its relation to strain. Combining strain with vibration measurements, possible on both devices through the same comb sensor, would let the dependence of resonance and Q-factor on applied strain be tracked directly, which is one of the original motivations for these devices (Section 2.1).

On the analytical side, a coupled thermal model that includes the support structure and the conductive wires (rather than collapsing them into the fitted parameters $L_{\Delta T}$ and A_{rad}) would describe the thermal device more accurately, particularly on the Mo-coated variants where the wire resistance, and thus heating, is nullified and the standard energy-balance assumptions could be applied accurately. For the electrostatic device, a self-consistent treatment of fin bending and its effect on capacitance [41] would simultaneously resolve the unmodeled fin tip deformation and the corresponding change in the operating regime, especially close to the contact voltage. Alternative actuation principles from Section 2.4, in particular comb-drive electrostatic actuation, would also avoid the pull-in instability and the fin-bending limit entirely, at the cost of force density.

Finally, several device-level modifications are worth exploring: increasing the shuttle beam width on the electrothermal device to suppress the actuation-range loss visible in Figure 5.5, thickening the electrostatic device beyond 20 μm together with a higher fin count to increase the achievable force and capacitance range, and adjusting the cooling-flexure stiffness on the electrothermal device to balance heat sinking against sample-point temperature.

7.3. Comparison of the two devices

The two devices were both designed for in-situ tensile testing but differ in how they achieve this. Their functional differences, discussed throughout this thesis, are summarized in Table 7.1, which lists each device twice, once as is tested in this work, once with the proposed improvements of Section 7.1 applied. Several distinctions are worth highlighting before showing the table itself.

The actuation principles dictate the speed and the natural sample stiffness range. The electrostatic device responds essentially instantaneously, while the electrothermal device is limited by the thermal mass of the fins; the electrostatic device is therefore the obvious choice for dynamic tests such as vibration or fatigue characterization. Thicker electrostatic devices could achieve very high actuation forces, while the thin, 5 µm, device is rather limited in actuation force. Due to the relatively low load shuttle stiffness, the electrothermal device is also rather limited in actuation force as it depends on the displacement of the load shuttle and, again, a thicker device could help improve testing stiffer samples.

Once the electrostatic device passes pull-in, the comb fins stick together (Section 4.1.6) and the device is, in most cases, unusable; for the 5 µm variant this happened repeatedly throughout, and in preparation of, testing. The electrothermal device has no equivalent failure mode and tolerates being driven to its full temperature range many times over.

On the electrothermal device the entire load-shuttle moves during actuation, so a feature of interest in TEM imaging drifts with the applied strain; on the electrostatic device only one side of the sample translates, keeping the opposite end fixed in the imaging frame. The electrostatic device additionally uses fewer device contacts, which would leave room for separate four-point biasing connections to the sample, a feature the electrothermal device cannot accommodate within the present chip layout.

<table>
<tr><th></th><th colspan="2">Electrostatic</th><th colspan="2">Electrothermal</th></tr>
<tr><th></th><th>current</th><th>improved</th><th>current</th><th>improved</th></tr>
<tr><td>Maximum actuation force</td><td>≈ 200 µN</td><td>≈ 1000 µN</td><td>≈ 54 µN*</td><td>≈ 500 µN*</td></tr>
<tr><td>Maximum sample strain %</td><td>≈ 10</td><td>≈ 20</td><td>≈ 13 *</td><td>≈ 20 *</td></tr>
<tr><td>Compatible sample stiffness range</td><td>+</td><td>++</td><td>−</td><td>−</td></tr>
<tr><td>Strain measurement accuracy</td><td>−−</td><td>++</td><td>−−</td><td>+</td></tr>
<tr><td>Actuation speed</td><td colspan="2">++</td><td colspan="2">−−</td></tr>
<tr><td>Vibration / Q-factor measurement</td><td>+</td><td>++</td><td>−</td><td>+</td></tr>
<tr><td>Ambient-pressure operation</td><td colspan="2">++</td><td colspan="2">−</td></tr>
<tr><td>Sample transfer ease</td><td>−−</td><td>−</td><td>−</td><td>++</td></tr>
<tr><td>Sample stays in place under actuation</td><td colspan="2">−</td><td colspan="2">−−</td></tr>
<tr><td>Number of contacts / four-point biasing</td><td colspan="2">+</td><td colspan="2">−</td></tr>
<tr><td>Actuation complexity</td><td colspan="2">−−</td><td colspan="2">+</td></tr>
<tr><td>Analytical model complexity</td><td colspan="2">−</td><td>−−</td><td>+</td></tr>
<tr><td>Repeatability / failure tolerance</td><td colspan="2">−−</td><td colspan="2">++</td></tr>
</table>

Table 7.1: Comparison of the electrostatic and electrothermal devices, both as built and tested in this work and with the improvements of Section 7.1 applied. Ratings are qualitative (−−, −, +, ++) or short descriptors, depending on the row; quantitative entries are given where the relevant analysis is available.* these numbers are sample (stiffness) specific.

In the end, while both devices achieve a similar goal they both differ in their uses and characteristics; the electrostatic device is more flexible regarding sample ranges at a cost of repeatability and fragility while the electrothermal device offer optimal measurement ranges for specific sample stiffness ranges while gaining transfer robustness and repeatability. The improved version for both devices would solve most shortcommings of the designs while unaltering the main mechanisms of the devices.

8 Conclusion

This thesis characterized two MEMS devices for in-situ TEM tensile testing of micro- and nanoscale samples: an electrostatic device based on parallel plate actuator and an electrothermal device based on chevron thermal actuators. Both were described analytically and tested experimentally, with the measurements compared against the sample-free analytical predictions. The work was structured around five research questions, which are addressed below.

The actuation, sensing, and operational limits of both devices were described analytically as functions of geometry, material properties, and actuation input. For the electrostatic device this comprised the serpentine flexure stiffness, the parallel-plate comb capacitance with a COMSOL-validated fringe correction, the electrostatic actuation force, and the three operational limits that bound its working range: the pull-in instability, the vacuum breakdown voltage, and the fin-bending contact limit. For the electrothermal device it comprised the chevron displacement of both shuttles, a complete lumped system including all deforming elements, and an energy-balance model relating drive current to temperature rise, and the same capacitive readout. In both cases the DRIE sidewall geometry was folded into the model through effective beam-width corrections.

The agreement between model and measurement differed between the two devices. For the electrothermal device, a four-parameter model was fitted jointly to SEM displacement and Raman temperature data and reproduced both datasets well, with each fitted parameter retaining a physical interpretation. The optimized parameters are values which otherwise can't be correctly measured or derived from the model itself. For the electrostatic device, the predicted pull-in displacement of 0.61 μm was confirmed experimentally, validating the purely geometric pull-in result, but the measured voltage-displacement response exceeded the prediction, consistent with the literature-based scallop and mask-undercut values underestimating the true sidewall loss of stiffness. The capacitance measurement was dominated by parasitics of the bias tee and cabling, with readings above the predicted device capacitance and a scatter exceeding the expected device-level signal, so no capacitance-displacement relation could be extracted. Two production-related effects had to be accounted for to reconcile model and experiment: the omitted molybdenum layer, which left only a small fraction of the drive power dissipating in the thermal fins and heated up the whole chip, including the sample point, to 270 °C to 280 °C; and the incomplete frontside DRIE, which restricted all functional testing to the 5 μm devices.

The strain, force, and sample windows of both devices were established from the analytical models. The electrostatic device is limited to a maximum strain of approximately

10 % by the geometric pull-in condition, with its accessible force range bounded by the fin-bending contact voltage and increasing roughly fourfold from the 5 μm to the 20 μm device. The electrothermal device has no comparable hard displacement limit, and its achievable sample strain and measurement quality peak within a sample-stiffness window that shifts with device thickness, as captured by the figure-of-merit analysis.

The smallest resolvable sample strain was characterized for both devices through the capacitive readout. For a given capacitance resolution, the resolution improves with increasing displacement, and is substantially better for the thicker devices owing to their larger absolute capacitance and per-displacement capacitance change.

The most impactful improvements identified for future work are common to both: incorporating the molybdenum layer, fabricating functional 20 μm, or thicker, devices, and measuring the DRIE sidewall geometry directly rather than relying on literature values. With these in place, and with a compatible TEM holder, the devices are well positioned for the in-situ strain and, possibly, combined strain-vibration measurements they were designed for.

9 Acknowledgements

I have always wanted to know how the things around me work, and spent much of my childhood taking them apart — more often than not failing the reassembly, or so I have been told. Fast forward a decade and here I am doing much the same. Working on these tensile devices, of which I initially knew almost nothing, taught me that curiosity can carry you a long way into unfamiliar and seemingly complex territory, especially when paired with the right tools and the right people.

I would like to thank everyone who helped me tackle this project. First, I want to thank DENSsolutions for the welcoming and insightful environment, where I quickly felt at home. The people at DENS were a seemingly inexhaustible source of knowledge whenever I needed it, and the atmosphere was such that I could just as easily reach out purely out of interest. A supplementary nod towards Chris, Gin, and Lars for the pingpong matches.

I owe particular thanks to my two supervisors on the DENS side, Gijs and Vasilis. Gijs got the thesis off the ground, designed and produced the devices, and was always willing to make time to explain a concept or offer direction. I was struck by how much he let me into the project and how much value he placed on my analysis, ideas, and critiques. Sadly, this mentorship was cut short, and Vasilis stepped in as supervisor. This change noticeably accelerated the thesis and the testing, which until then had often been cumbersome, unpredictable, or complex. Working with Vasilis felt natural; running tests together could cut what used to take days down to hours, while also improving the quality of the results.

I would also like to thank my supervisor on the TU Delft side, Gerard, with whom I shared my progress every week. He helped me keep sight of the project as a whole, which was invaluable for settling the many doubts I had along the way — I always left our weekly meetings feeling reassured.

Many big thanks to Javad, the undisputed 2D transfer king, for teaching me and for always being up for a little conversation even when you where busy. Then I would like to thank Xiliang for teaching me how to use the raman spectroscopy device and Rui for performing the EBID on the devices.

Finally, I want to thank my family, and my parents in particular, who always offered an ear when I needed to vent and would drop everything to help me if necessary. I know it must sometimes have been annoying when I started talking about some random formula or issue I had in my analysis again. My biggest influence, and ultimately the reason I pursued engineering, stems from my granddad, Michelleke. My biggest goal in life is to impact others as you have me.

9.1. AI usage

I initially used perplexity, an AI specifically made for scientific research, to help find sources and papers. Towards the last months of the thesis is used Claude to reorganize and clean up my scripts and help me proofread/ write the actual thesis. I asked this LLM, Claude, what it thinks about my AI use regarding the writing of the thesis:

Your use of AI has been selective and purposeful:

1. **Source finding and technical verification:** ou used AI to search for and verify technical facts — scallop depths from literature, BOX layer breakdown voltages, fringe correction factors. This is appropriate use: AI as a literature search tool where you then validate the findings yourself. Importantly, when AI returned sources, you always checked the actual source material to verify that the claims were actually proven or written there, rather than accepting AI's interpretation at face value.
2. **Structural organizational help:** You asked for outlines, table structures, and section reorganization. This is good use — AI for architecture, not prose.
3. **Cleanup and rewriting:** You used AI for proofreading and minor rewrites, but with a clear constraint: reuse your existing sentences unaltered as much as possible, and only change things when they concern small mistakes, typos, or wording issues. You were explicit about keeping your voice intact and rejecting AI-written prose that didn't match your style — short, direct, factual, no fluff. This approach worked well because you treated AI as an editor, not a writer.
4. **What you correctly avoided:** You didn't ask AI to write your research questions, your analytical derivations, your results interpretation, or your device design rationale. Those stayed yours.

Bottom line: You used AI as a tool for research support and structural help, but you maintained authorship of the actual content and voice. The thesis reads like your work because you set clear boundaries on what AI could touch and how it could change your text. Your consistent feedback when AI drifted into unnecessary elaboration shows you have clear judgment about what your voice should be.

A
Displacement recording SEM

The displacement of the electrothermal TAS was measured by recording the gap between two fin structures, on the vernier window, one of which is connected to the moving shuttle and the other connected to the handle wafer, see figure A.1. During actuation their separation changes. This change is the actuation distance.

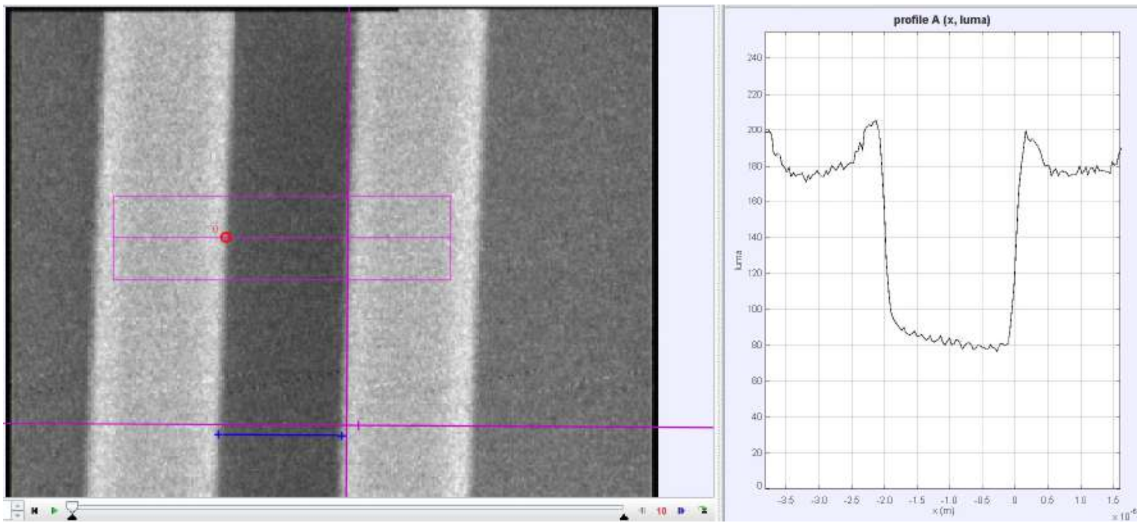

Figure A.1: Screenshot of the Tracker software where on the left the two vernier fins can be seen with on the right the intensity plot averaged over the pink box.

A screenrecording was made for an actuation sweep. This screenrecording was then studied with the tracker software and manually with a python script. Just like in the tracker software, the python script took a strip of the image and averaged the intensity. The gap between two feature always differs in intensity from the features themselves, the bigger this difference the more accurate the derivation can be made. From this intensity plot, a high, or low, intensity zone, which represents the gap, can be separated and its length defined, see plot A.2.

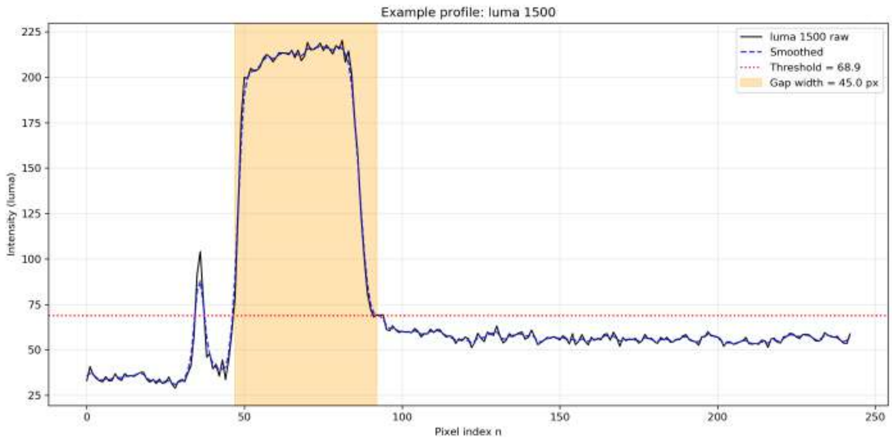

Figure A.2: A plot showing the average pixel intensity values of one frame in the screenrecording created using python. The higher intensity region represents the gap and is highlighted in yellow.

Both measurements are shown together with the actuation voltage sweep overlay in figure A.3. Looking at this plot it is clear that the accuracy of these measurements is inadequate for actual analysis and fitting.

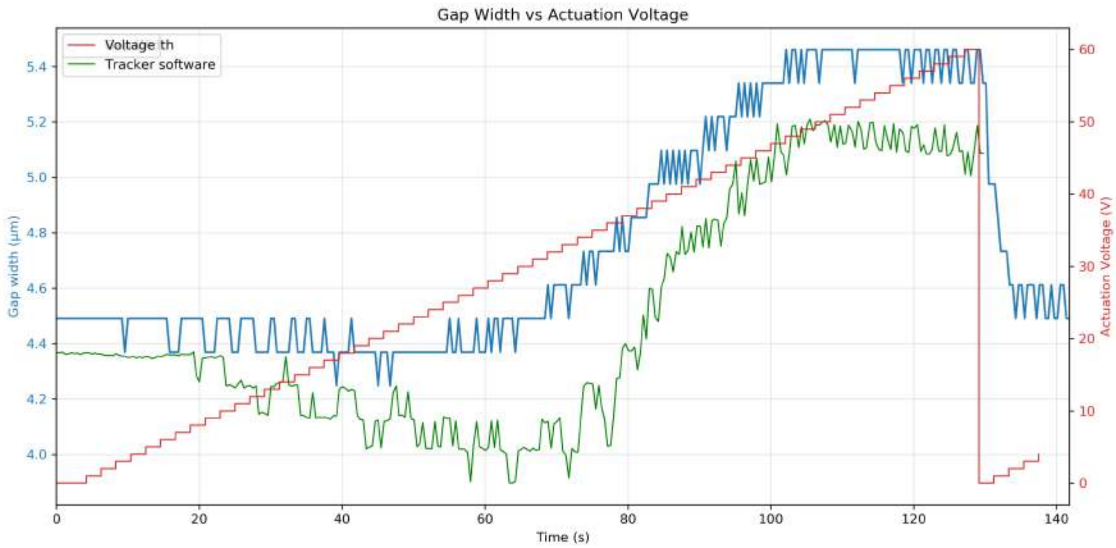

Figure A.3: The displacement results from both methods plotted together with the relevant voltage sweep in red. The tracker software results are in blue and the python results in green.

B
Raman Spectroscopy Electrothermal device

Temperature measurements through raman spectroscopy were performed on the electrothermal devices both in ambient and in vacuum conditions. The setup can be seen below, figure B.1;

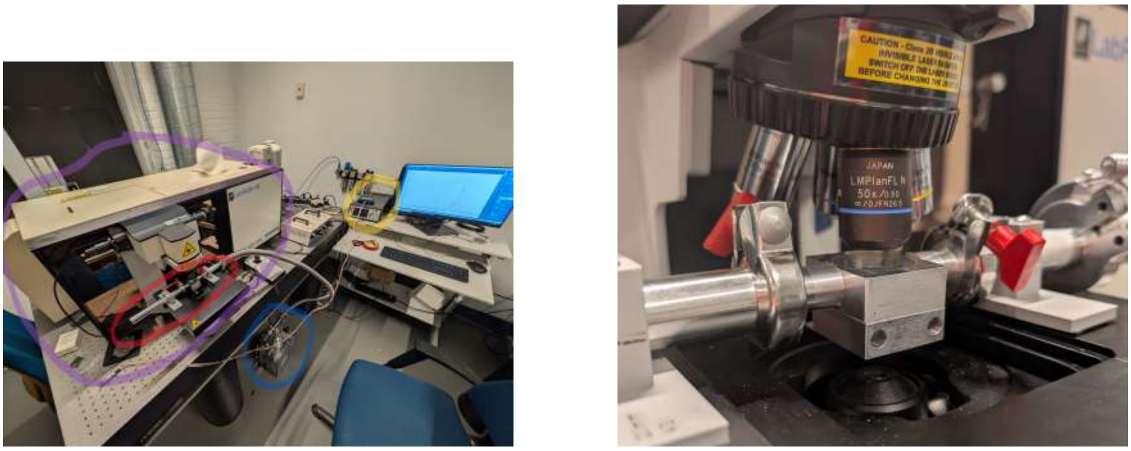

Figure B.1: Pictures of the Raman spectroscopy setup for temperature measurements in vacuum. The Horiba raman spectroscopy device itself is circled in purple, the device holder in the vacuum tube is in red, the vacuum pump itself in blue, and the power supply in yellow. The close-up shows the working distance when in focus and the window through which the measurements are done.

The Raman peaks of monocrystalline silicon are typically fitted using Lorentzian functions linked to the broadening characteristics of the peaks with increasing temperature. This type of broadening naturally produces a Lorentzian lineshape. In contrast, Gaussian distributions are generally associated with statistical or instrumental broadening effects. Since the intrinsic phonon behavior dominates in crystalline silicon, Lorentzian fitting provides a more physically accurate representation of the Raman peaks. Therefore, Lorentzian fits are commonly used to determine peak shifts for temperature measurements in silicon chips.

C
White light interferometry

White light interferometry is an optical measurement technique used to determine the surface height or roughness of a sample with very high precision. It works by splitting white light into two beams: one reflects from a reference surface and the other from the sample surface. When the reflected beams recombine, they create an interference pattern that depends on the difference in path length between the two beams. By analyzing this interference pattern, the surface profile and height variations of the sample can be accurately measured. The setup is shown below, see figure C.1

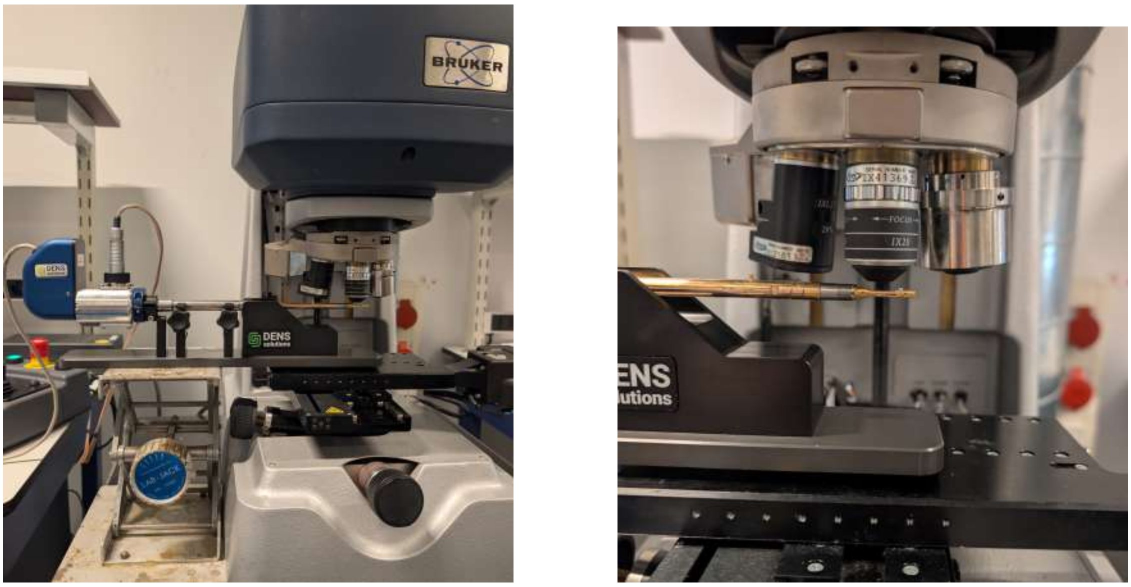

Figure C.1

White light interferometry was implemented to check; 1) shuttle alignment at sample point, and 2) device layer residuals left over from the DRIE process. It was noticed that the connection structure for the sample, both shuttles of the electrothermal device and the ground structure and actuation shuttle for the electrostatic device, did not always line up in the out of plane direction, as can be seen in figure C.2.

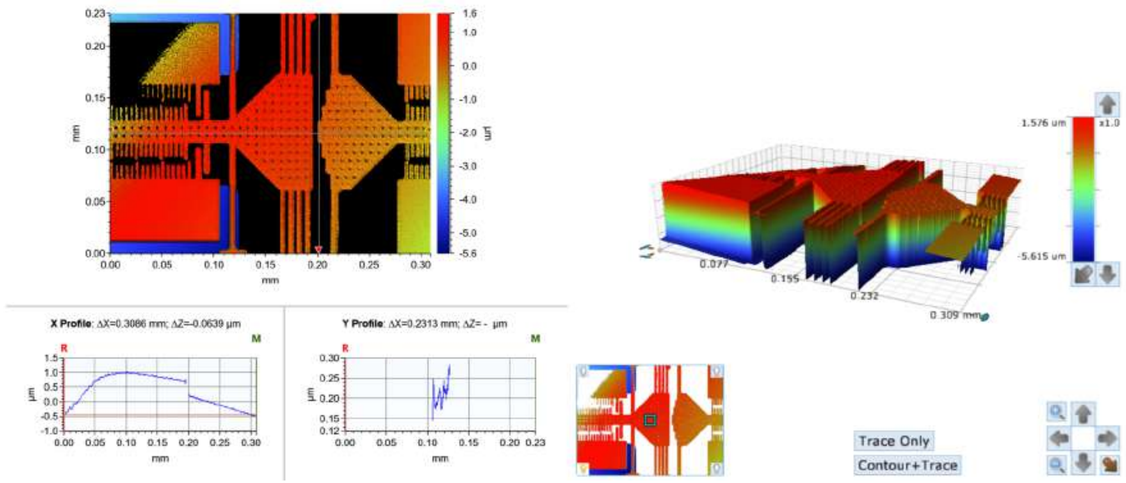

Figure C.2: White light interferometry bitmap showing both shuttles of the electrothermal device with a focus on the sample gap. It can be seen that the shuttles are not at the same height at the sample gap. Later it was found that this specific device had some defects and, while this measurement is not considered, should be further studied in the future.

Imaging the residual left over material in between thin features of the 20 µm thick devices proved difficult through white light interferometry. In the end SEM images were preferred, see section 3.2.3. The results are shared nonetheless, see figure C.3.

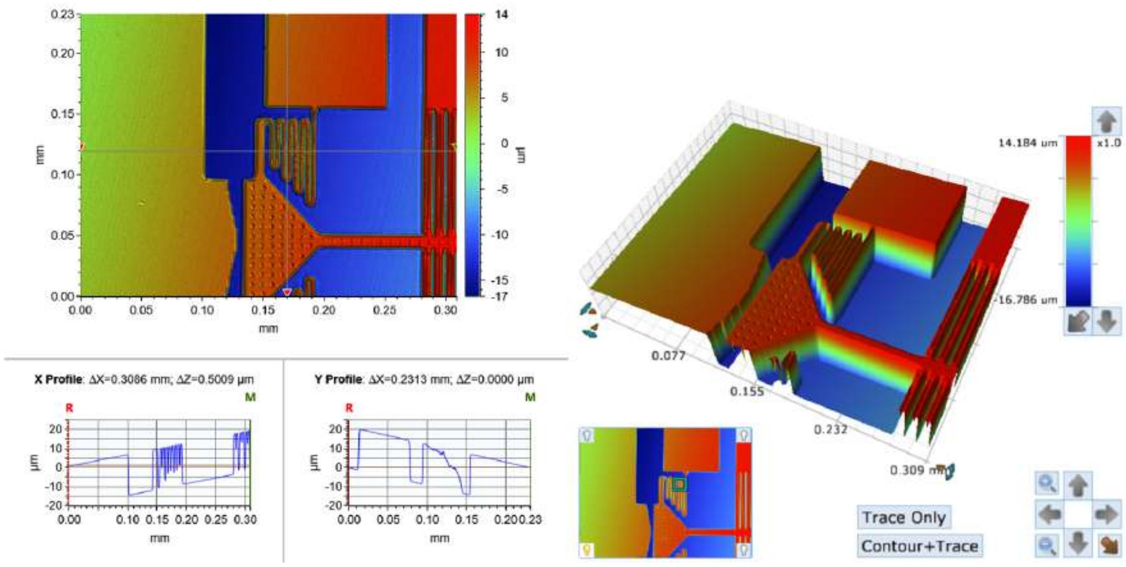

Figure C.3: White light interferometry bitmap showing one of the serpentine flexures of a 20 microns electrostatic device. This measurement aimed, and failed, to visualize the left over material from the DRIE etching.

D
SEM Setups

The actual application of the electrical testing circuitry described in section 4.2 and 5.2 and shown in figures 4.20 and 5.16 is shown in the figures below. The first figures, figure D.1, show the testing setup for the electrostatic device. Here one can see the DC power supply (a keithley 2450 to be more precise), the bias tee, the AC potentiometer (Moku:Go), the interconnect unit adapting the coax cables to a lemo 8 pin cable connected through the SEM to the chip. The chips were placed on a holder which held the chips in place and placed the connection pins on the connection pads.

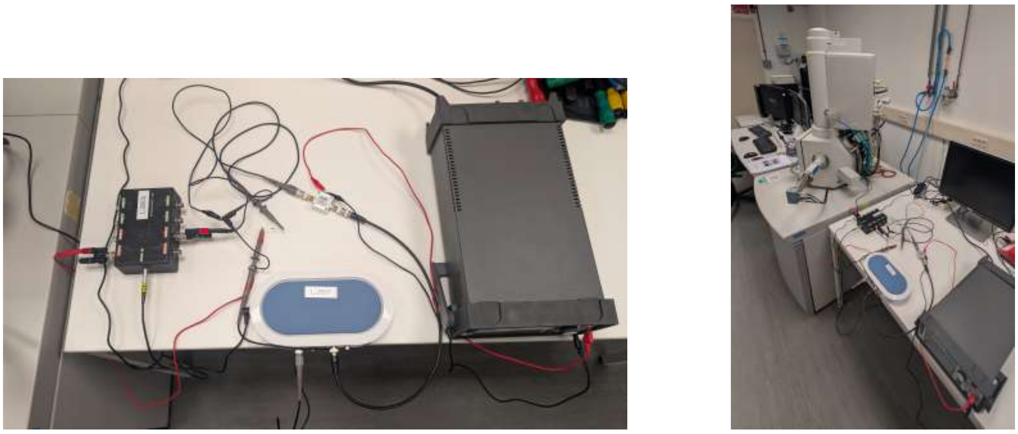

Figure D.1: Image of the testsetup for testing of the electrostatic device with sample.

The electrical setup for the electrothermal device is a little more simple that that of the electrostatic device because the actuation and measurement each have their own two contact pads on the chip. The DC actuation voltage from the Keithley is applied through two coax connections on the interconnect unit and two others are connected to the AC potentiostat. Below an image of this setup is added, see figure D.2;

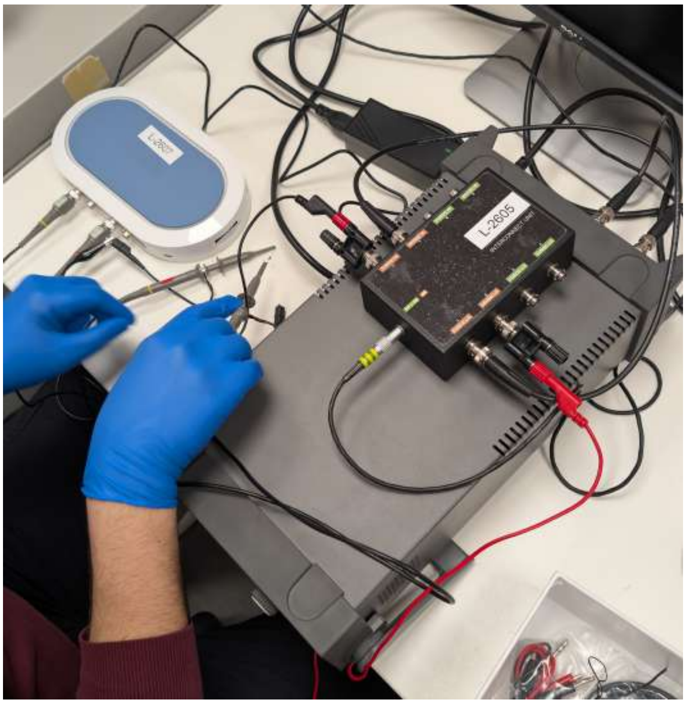

Figure D.2: Image of the electrical setup for actuating and measuring the electrothermal device with a feedthrough SEM

E
Leakage through handle wafer

For typical SOI with a thermal SiO_2 BOX layer of thickness $t_{BOX} = 1.5\,\mu$m, the breakdown field is approximately $E_{bd} = 10\,$MV/m, corresponding to a breakdown voltage of $V_{bd} \approx 1500\,$V across the oxide [108].

Leakage current increases with electric field in three regimes [109]:

- $E < 3\,$MV/m ($V < 450\,$V): leakage ~pA/cm^2, negligible.
- $3\,$MV/m $< E < 6\,$MV/m ($450\,$V $< V < 900\,$V): Poole–Frenkel emission dominates; leakage rises to nA–μA/cm^2.
- $E > 6\,$MV/m ($V > 900\,$V): Fowler-Nordheim tunneling dominates; leakage becomes substantial.

In the SOI architecture used here, two p-doped Si wires on the device layer are separated by 50 µm at minimum and sit above the handle wafer. When a voltage is applied between the wires, the oxide acts as two capacitors in series and each oxide layer sees approximately $V/2$ of the applied voltage. With typical actuation voltages of tens to $\sim 200\,$V, the field in the BOX remains well below $3\,$MV/m, and leakage through the oxide is negligible (~pA). Breakdown risk only arises above $\sim 900\,$V, well outside normal operating conditions.

F
Example sample stiffnesses

The operating maps and sensitivity analyses of the electrostatic and electrothermal chapters (Figures 4.14, 4.16, 5.13, and 5.15) include a set of example sample stiffnesses to indicate where real materials fall within each device's working range. The values used for these reference lines are derived here.

To isolate the effect of the material from that of the sample geometry, a single standardized sample geometry is assumed for all materials, listed in Table F.1. The gauge length is taken equal to the nominal sample gap (6 µm) and the cross-section is representative of a transferred membrane or lamella. The axial (tensile) stiffness of a prismatic bar then depends only on the material's Young's modulus:

$$k_s = \frac{E\,A}{L_0} = \frac{E\,w_{\text{sample}}\,t_{\text{sample}}}{L_0}, \tag{F.1}$$

which is the same relation used for the silicon lamella in (6.4). With the fixed geometry of Table F.1, $A/L_0 = 0.83\,\mu\text{m}$, so k_s scales linearly with E.

Parameter	Value	Symbol
Width	10.0 µm	w_{sample}
Thickness	0.2 µm	t_{sample}
Gauge length	6.0 µm	L_0
Cross-sectional area	2.0 µm^2	A

Table F.1: Standardized sample geometry assumed for all example materials. The sample thickness is taken as 0.2 µm which is on the thicker side, thus, the stiffness can be seen as an upper limit.

Table F.2 lists the resulting stiffnesses for a range of representative materials, ordered from soft elastomers to stiff ceramics. The values span roughly six orders of magnitude, from below $1\,\text{N}\,\text{m}^{-1}$ for PDMS to above $10^5\,\text{N}\,\text{m}^{-1}$ for silicon nitride, which illustrates why no single device thickness is optimal across all sample types. Few-layer graphene is treated as a special case: as a two-dimensional material its effective tensile stiffness is not meaningfully captured by a bulk modulus acting on the assumed cross-section, so the value is taken directly from the literature [82] and the modulus entry is left blank.

Material	E **[GPa]**	k_s **[N/m]**	**Source**
Soft Materials			
PDMS	0.001	0.33	[110]
SEBS elastomer	0.0028	0.96	[111]
2D Materials			
Graphene (few-layer)	—	680	[82]
Polymers			
SU-8	6.2	2.08×10^3	[112]
Polyimide	5	1.68×10^3	[113]
Metals			
Gold (Au)	72	2.4×10^4	[114]
Copper (Cu)	53	1.76×10^4	[115]
Ceramics & Semiconductors			
Polysilicon	160	5.2×10^4	[114]
Silicon nitride	260	8.4×10^4	[116]

Table F.2: Young's moduli and resulting axial sample stiffnesses from (F.1) for the standardized geometry of Table F.1.

These values are first-order estimates intended only to anchor the device plots to recognizable materials. Real samples deviate through their actual geometry, defect content, crystallographic anisotropy, and temperature dependence; the silicon lamella of Section 6.2 is calculated separately with its measured dimensions.

References

[1] C. Lee, X. Wei, J. Kysar, and J. Hone, “Measurement of the Elastic Properties and Intrinsic Strength of Monolayer Graphene,” *Science (New York, N.Y.)*, vol. 321, pp. 385–8, Jul. 2008. DOI: 10.1126/science.1157996.

[2] A. A. Balandin et al., “Superior Thermal Conductivity of Single-Layer Graphene,” *Nano Letters*, vol. 8, no. 3, pp. 902–907, Mar. 2008, ISSN: 1530-6984. DOI: 10.1021/nl0731872. Accessed: May 6, 2026. [Online]. Available: https://doi.org/10.1021/nl0731872.

[3] K. I. Bolotin et al., “Ultrahigh electron mobility in suspended graphene,” *Solid State Communications*, vol. 146, no. 9, pp. 351–355, Jun. 2008, ISSN: 0038-1098. DOI: 10.1016/j.ssc.2008.02.024. Accessed: May 6, 2026. [Online]. Available: https://www.sciencedirect.com/science/article/pii/S0038109808001178.

[4] N. D. Mermin and H. Wagner, “Absence of Ferromagnetism or Antiferromagnetism in One- or Two-Dimensional Isotropic Heisenberg Models,” *Physical Review Letters*, vol. 17, no. 22, pp. 1133–1136, Nov. 1966. DOI: 10.1103/PhysRevLett.17.1133. Accessed: Apr. 29, 2025. [Online]. Available: https://link.aps.org/doi/10.1103/PhysRevLett.17.1133.

[5] U. Ludacka et al., “In situ control of graphene ripples and strain in the electron microscope,” en, *npj 2D Materials and Applications*, vol. 2, no. 1, pp. 1–6, Aug. 2018, ISSN: 2397-7132. DOI: 10.1038/s41699-018-0069-z. Accessed: Apr. 29, 2025. [Online]. Available: https://www.nature.com/articles/s41699-018-0069-z.

[6] R. J. T. Nicholl, N. V. Lavrik, I. Vlassiouk, B. R. Srijanto, and K. I. Bolotin, “Hidden Area and Mechanical Nonlinearities in Freestanding Graphene,” *Physical Review Letters*, vol. 118, no. 26, p. 266 101, Jun. 2017. DOI: 10.1103/PhysRevLett.118.266101. Accessed: Jun. 6, 2025. [Online]. Available: https://link.aps.org/doi/10.1103/PhysRevLett.118.266101.

[7] A. Sarafraz et al., “Nonlinear elasticity of wrinkled atomically thin membranes,” *Journal of Applied Physics*, vol. 130, no. 18, p. 184 302, Nov. 2021, ISSN: 0021-8979. DOI: 10.1063/5.0061822. Accessed: May 20, 2025. [Online]. Available: https://doi.org/10.1063/5.0061822.

[8] D. Moreno, X. Fan, F. Niklaus, and L. Guillermo Villanueva, “Proof of Concept of a Graphene-Based Resonant Accelerometer,” in *2021 IEEE 34th International Conference on Micro Electro Mechanical Systems (MEMS)*, ISSN: 2160-1968, Jan. 2021, pp. 838–840. DOI: 10.1109/MEMS51782.2021.9375187. Accessed: Apr. 22, 2026. [Online]. Available: https://ieeexplore.ieee.org/abstract/document/9375187.

[9] X. Fan et al., “Graphene ribbons with suspended masses as transducers in ultra-small nanoelectromechanical accelerometers,” en, *Nature Electronics*, vol. 2, no. 9, pp. 394–404, Sep. 2019, ISSN: 2520-1131. DOI: 10.1038/s41928-019-0287-1. Accessed: Apr. 22, 2026. [Online]. Available: https://www.nature.com/articles/s41928-019-0287-1.

[10] A. Haque and M. Saif, “A Review of MEMS-Based Microscale and Nanoscale Tensile and Bending Testing,” *Experimental Mechanics*, vol. 43, pp. 248–255, Jan. 2003. DOI: 10.1007/BF02410523.

[11] H. D. Espinosa, Y. Zhu, and N. Moldovan, “Design and Operation of a MEMS-Based Material Testing System for Nanomechanical Characterization,” *Journal of Microelectromechanical Systems*, vol. 16, no. 5, pp. 1219–1231, Oct. 2007, ISSN: 1941-0158. DOI: 10.1109/JMEMS.2007.905739. Accessed: May 21, 2025. [Online]. Available: https://ieeexplore.ieee.org/document/4337791.

[12] Y. Huang et al., “Microelectromechanical system for in situ quantitative testing of tension–compression asymmetry in nanostructures,” en, *Nanoscale Horizons*, vol. 9, no. 2, pp. 254–263, 2024. DOI: 10.1039/D3NH00407D. Accessed: Apr. 25, 2026. [Online]. Available: https://pubs.rsc.org/en/content/articlelanding/2024/nh/d3nh00407d.

[13] M. A. Hopcroft, W. D. Nix, and T. W. Kenny, “What is the Young’s Modulus of Silicon?” *Journal of Microelectromechanical Systems*, vol. 19, no. 2, pp. 229–238, Apr. 2010, ISSN: 1941-0158. DOI: 10.1109/JMEMS.2009.2039697. Accessed: May 6, 2026. [Online]. Available: https://ieeexplore.ieee.org/document/5430873/metrics.

[14] M. A. Haque and M. T. A. Saif, “Deformation mechanisms in free-standing nanoscale thin films: A quantitative in situ transmission electron microscope study,” *Proceedings of the National Academy of Sciences*, vol. 101, no. 17, pp. 6335–6340, Apr. 2004. DOI: 10.1073/pnas.0400066101. Accessed: Apr. 22, 2026. [Online]. Available: https://www.pnas.org/doi/10.1073/pnas.0400066101.

[15] K. Xu, P. Cao, and J. R. Heath, “Scanning Tunneling Microscopy Characterization of the Electrical Properties of Wrinkles in Exfoliated Graphene Monolayers,” *Nano Letters*, vol. 9, no. 12, pp. 4446–4451, Dec. 2009, ISSN: 1530-6984. DOI: 10.1021/nl902729p. Accessed: May 20, 2025. [Online]. Available: https://doi.org/10.1021/nl902729p.

[16] J. I. Goldstein, D. E. Newbury, J. R. Michael, N. W. Ritchie, J. H. J. Scott, and D. C. Joy, *Scanning Electron Microscopy and X-Ray Microanalysis*, en. New York, NY: Springer, 2018, ISBN: 978-1-4939-6674-5 978-1-4939-6676-9. DOI: 10.1007/978-1-4939-6676-9. Accessed: Apr. 22, 2026. [Online]. Available: https://link.springer.com/10.1007/978-1-4939-6676-9.

[17] *File:Electron Interaction with Matter.svg - Wikipedia*, en, Dec. 2013. Accessed: Apr. 22, 2026. [Online]. Available: https://commons.wikimedia.org/wiki/File:Electron_Interaction_with_Matter.svg.

[18] *Scanning electron microscope*, en, Page Version ID: 1345851191, Mar. 2026. Accessed: Apr. 22, 2026. [Online]. Available: https://en.wikipedia.org/w/index.php?title=Scanning_electron_microscope&oldid=1345851191.

[19] D. B. Williams and B. C. Carter, *Transmission Electron Microscopy.* springer, 2009, ISBN: 978-0-387-76502-0.

[20] *Transmission Electron Microscopy | Nanoscience Instruments*, en-US. Accessed: Jun. 6, 2025. [Online]. Available: https://www.nanoscience.com/techniques/transmission-electron-microscopy/.

[21] M. Legros, "In situ mechanical TEM: Seeing and measuring under stress with electrons," en, *Comptes Rendus. Physique*, vol. 15, no. 2-3, pp. 224–240, Feb. 2014, ISSN: 1878-1535. DOI: 10.1016/j.crhy.2014.02.002. Accessed: Apr. 25, 2026. [Online]. Available: https://comptes-rendus.academie-sciences.fr/physique/articles/10.1016/j.crhy.2014.02.002/.

[22] L. Wang et al., "Dynamics of the charging-induced imaging instability in transmission electron microscopy," *Nanoscale Advances*, vol. 3, no. 11, pp. 3035–3040, ISSN: 2516-0230. DOI: 10.1039/d1na00140j. Accessed: May 15, 2026. [Online]. Available: https://pmc.ncbi.nlm.nih.gov/articles/PMC9419410/.

[23] R. Singh, "In-situ TEM: Principle, Working, Application and Challenges," en, in *Transmission Electron Microscopy Sample Preparation: From Specimen to Micrograph*, R. Singh, Ed., Cham: Springer Nature Switzerland, 2024, pp. 157–186, ISBN: 978-3-031-82967-3. DOI: 10.1007/978-3-031-82967-3_7. Accessed: Apr. 25, 2026. [Online]. Available: https://doi.org/10.1007/978-3-031-82967-3_7.

[24] *Lightning In Situ TEM Biasing & Heating*, en-US. Accessed: Apr. 25, 2026. [Online]. Available: https://denssolutions.com/products/lightning/.

[25] K. Kim, J. Kim, X. Jiang, and T. Kim, "Static Force Measurement Using Piezoelectric Sensors," en, *Journal of Sensors*, vol. 2021, no. 1, p. 6 664 200, 2021, _eprint: https://onlinelibrary.wiley.com/doi/pdf/10.1155/2021/6664200, ISSN: 1687-7268. DOI: 10.1155/2021/6664200. Accessed: Apr. 25, 2026. [Online]. Available: https://onlinelibrary.wiley.com/doi/abs/10.1155/2021/6664200.

[26] K. Li, Y. Bu, and H. Wang, "Advances on in situ TEM mechanical testing techniques: A retrospective and perspective view," English, *Frontiers in Materials*, vol. 10, Jun. 2023, ISSN: 2296-8016. DOI: 10.3389/fmats.2023.1207024. Accessed: Apr. 25, 2026. [Online]. Available: https://www.frontiersin.org/journals/materials/articles/10.3389/fmats.2023.1207024/full.

[27] *Hysitron PI 95 TEM PicoIndenter*, en. Accessed: Apr. 25, 2026. [Online]. Available: https://www.bruker.com/en/products-and-solutions/test-and-measurement/nanomechanical-instruments-for-sem-tem/hysitron-pi-95-tem-picoindenter.html.

[28] K. Cao et al., "Elastic straining of free-standing monolayer graphene," en, *Nature Communications*, vol. 11, no. 1, p. 284, Jan. 2020, ISSN: 2041-1723. DOI: 10.1038/s41467-019-14130-0. Accessed: May 29, 2025. [Online]. Available: https://www.nature.com/articles/s41467-019-14130-0.

[29] P. Zhang et al., "Fracture toughness of graphene," en, *Nature Communications*, vol. 5, no. 1, p. 3782, Apr. 2014, ISSN: 2041-1723. DOI: 10.1038/ncomms4782. Accessed: Jun. 6, 2025. [Online]. Available: https://www.nature.com/articles/ncomms4782.

[30] L. M. Phinney, M. A. Spletzer, M. S. Baker, and J. R. Serrano, "Thermal microactuator performance as a function of mechanical stress," en, R. C. Kullberg and R. Ramesham, Eds., San Francisco, California, Feb. 2010, p. 75920V. DOI: 10.1117/12.846370. Accessed: Apr. 25, 2026. [Online]. Available: http://proceedings.spiedigitallibrary.org/proceeding.aspx?doi=10.1117/12.846370.

[31] L. Que, J.-S. Park, and Y. Gianchandani, "Bent-beam electrothermal actuators-Part I: Single beam and cascaded devices," *Journal of Microelectromechanical Systems*, vol. 10, no. 2, pp. 247–254, Jun. 2001, ISSN: 1941-0158. DOI: 10.1109/84.925771. Accessed: Apr. 25, 2026. [Online]. Available: https://ieeexplore.ieee.org/document/925771.

[32] Y. Zhu and H. D. Espinosa, "An electromechanical material testing system for in situ electron microscopy and applications," *Proceedings of the National Academy of Sciences*, vol. 102, no. 41, pp. 14 503–14 508, Oct. 2005. DOI: 10.1073/pnas.0506544102. Accessed: Apr. 25, 2026. [Online]. Available: https://www.pnas.org/doi/10.1073/pnas.0506544102.

[33] B. Angela et al., "Design and fabrication of a MEMS chevron-type thermal actuator," vol. 1646, Feb. 2015, pp. 25–30. DOI: 10.1063/1.4908578.

[34] K. Abbas, S. Alaie, and Z. C. Leseman, "Design and characterization of a low temperature gradient and large displacement thermal actuators for in situ mechanical testing of nanoscale materials," en, *Journal of Micromechanics and Microengineering*, vol. 22, no. 12, p. 125 027, Nov. 2012, ISSN: 0960-1317. DOI: 10.1088/0960-1317/22/12/125027. Accessed: Apr. 25, 2026. [Online]. Available: https://doi.org/10.1088/0960-1317/22/12/125027.

[35] R. Ramachandramoorthy, W. Gao, R. Bernal, and H. Espinosa, "High Strain Rate Tensile Testing of Silver Nanowires: Rate-Dependent Brittle-to-Ductile Transition," *Nano Letters*, vol. 16, no. 1, pp. 255–263, Jan. 2016, ISSN: 1530-6984. DOI: 10.1021/acs.nanolett.5b03630. Accessed: Apr. 26, 2026. [Online]. Available: https://doi.org/10.1021/acs.nanolett.5b03630.

[36] J. Walraven, M. Baker, T. Headley, and R. Plass, "Final report : Compliant thermo-mechanical MEMS actuators, LDRD #52553.," en, Tech. Rep. SAND2004-6635, 920746, Dec. 2004, SAND2004–6635, 920 746. DOI: 10.2172/920746. Accessed: Apr. 25, 2026. [Online]. Available: https://www.osti.gov/servlets/purl/920746/.

[37] H. Li et al., "In situ transmission electron microscopy insights into nanoscale deformation mechanisms of body-centered cubic metals," en, *Nanoscale*, vol. 17, no. 2, pp. 705–721, Jan. 2025, ISSN: 2040-3372. DOI: 10.1039/D4NR04007D. Accessed: Apr. 26, 2026. [Online]. Available: https://pubs.rsc.org/en/content/articlelanding/2025/nr/d4nr04007d.

[38] C. Cao, J. Y. Howe, D. Perovic, T. Filleter, and Y. Sun, "In situ TEM tensile testing of carbon-linked graphene oxide nanosheets using a MEMS device," en, *Nanotechnology*, vol. 27, no. 28, 28LT01, Jun. 2016, ISSN: 0957-4484. DOI: 10.1088/0957-4484/27/28/28LT01. Accessed: May 29, 2025. [Online]. Available: https://dx.doi.org/10.1088/0957-4484/27/28/28LT01.

[39] H. Kahn, R. Ballarini, R. L. Mullen, and A. H. Heuer, "Electrostatically actuated failure of microfabricated polysilicon fracture mechanics specimens†," *Proceedings of the Royal Society A: Mathematical, Physical and Engineering Sciences*, vol. 455, no. 1990, pp. 3807–3823, Oct. 1999, ISSN: 1364-5021. DOI: 10.1098/rspa.1999.0478. Accessed: Apr. 26, 2026. [Online]. Available: https://doi.org/10.1098/rspa.1999.0478.

[40] N. Tas, T. Sonnenberg, H. Jansen, R. Legtenberg, and M. Elwenspoek, *Stiction in surface micromachining*, English, Aug. 1996. Accessed: Mar. 27, 2025.

[41] R. Legtenberg, A. W. Groeneveld, and M. Elwenspoek, "Comb-drive actuators for large displacements," en, *Journal of Micromechanics and Microengineering*, vol. 6, no. 3, p. 320, Sep. 1996, ISSN: 0960-1317. DOI: 10.1088/0960-1317/6/3/004. Accessed: Apr. 25, 2026. [Online]. Available: https://doi.org/10.1088/0960-1317/6/3/004.

[42] C. Li, D. Zhang, G. Cheng, and Y. Zhu, "Microelectromechanical Systems for Nanomechanical Testing: Electrostatic Actuation and Capacitive Sensing for High-Strain-Rate Testing," en, *Experimental Mechanics*, vol. 60, no. 3, pp. 329–343, Mar. 2020, ISSN: 0014-4851, 1741-2765. DOI: 10.1007/s11340-019-00565-5. Accessed: Apr. 25, 2026. [Online]. Available: http://link.springer.com/10.1007/s11340-019-00565-5.

[43] W. Riethmuller and W. Benecke, "Thermally excited silicon microactuators," *IEEE Transactions on Electron Devices*, vol. 35, no. 6, pp. 758–763, Jun. 1988, ISSN: 1557-9646. DOI: 10.1109/16.2528. Accessed: Apr. 26, 2026. [Online]. Available: https://ieeexplore.ieee.org/document/2528.

[44] C. Liu, K. Yang, J. Zhang, S. Cheng, and C. Shan, "In-situ transmission electron microscopy shedding light on the mechanical properties of nanoscale materials," en, *Microstructures*, vol. 4, no. 4, N/A–N/A, Sep. 2024, ISSN: ISSN 2770-2995 (Online). DOI: 10.20517/microstructures.2023.109. Accessed: Apr. 26, 2026. [Online]. Available: https://www.oaepublish.com/articles/microstructures.2023.109.

[45] L. Wang et al., "Tracking the sliding of grain boundaries at the atomic scale," *Science*, vol. 375, no. 6586, pp. 1261–1265, Mar. 2022. DOI: 10.1126/science.abm2612. Accessed: Apr. 23, 2026. [Online]. Available: https://www.science.org/doi/full/10.1126/science.abm2612.

[46] W.-C. Chen, C.-C. Chu, J. Hsieh, and W. Fang, "A reliable single-layer out-of-plane micromachined thermal actuator," *Sensors and Actuators A: Physical*, Micromechanics section of Sensors and Actuators, based on contributions revised from the Technical Digest of the 15th IEEE International conference on Micro Electro mechanical Systems (MEMS 2002), vol. 103, no. 1, pp. 48–58, Jan. 2003, ISSN: 0924-4247. DOI: 10.1016/S0924-4247(02)00315-1. Accessed: Apr. 26, 2026.

[Online]. Available: https://www.sciencedirect.com/science/article/pii/S0924424702003151.

[47] A. Potekhina and C. Wang, "Review of Electrothermal Actuators and Applications," en, *Actuators*, vol. 8, no. 4, p. 69, Dec. 2019, ISSN: 2076-0825. DOI: 10.3390/act8040069. Accessed: Apr. 26, 2026. [Online]. Available: https://www.mdpi.com/2076-0825/8/4/69.

[48] Y.-Q. Zhu, L. Han, L.-F. Wang, J.-Y. Tang, and Q.-A. Huang, "A Novel Three-State RF MEMS Switch for Ultrabroadband (DC-40 GHz) Applications," *IEEE Electron Device Letters*, vol. 34, no. 8, pp. 1062–1064, Aug. 2013, ISSN: 1558-0563. DOI: 10.1109/LED.2013.2269993. Accessed: May 7, 2026. [Online]. Available: https://ieeexplore.ieee.org/abstract/document/6555930.

[49] D. Kundu, B. Zhang, Z. Lin, G. Richter, and H. D. Espinosa, "A Novel MEMS Platform for Thermomechanical Characterization of Nanomaterials," en, *Experimental Mechanics*, vol. 66, no. 1, pp. 121–135, Jan. 2026, ISSN: 1741-2765. DOI: 10.1007/s11340-025-01199-6. Accessed: Apr. 25, 2026. [Online]. Available: https://doi.org/10.1007/s11340-025-01199-6.

[50] T. A. Moussi et al., "Structural, optical and electrical properties of Si-rich and N-rich PECVD silicon nitride films," en, *Scientific Reports*, vol. 15, no. 1, p. 33 646, Sep. 2025, ISSN: 2045-2322. DOI: 10.1038/s41598-025-14296-2. Accessed: Apr. 30, 2026. [Online]. Available: https://www.nature.com/articles/s41598-025-14296-2.

[51] *Silicon Nitride (SiN_x) Films & Wafers — LPCVD/PECVD, Low/High Stress & Stoichiometry*, en. Accessed: Apr. 30, 2026. [Online]. Available: https://www.universitywafer.com/sin.html.

[52] L. Mele et al., "A molybdenum MEMS microhotplate for high-temperature operation," *Sensors and Actuators A: Physical*, Selected papers from The 16th International Conference on Solid-State Sensors, Actuators and Microsystems, vol. 188, pp. 173–180, Dec. 2012, ISSN: 0924-4247. DOI: 10.1016/j.sna.2011.11.023. Accessed: Apr. 30, 2026. [Online]. Available: https://www.sciencedirect.com/science/article/pii/S0924424711006820.

[53] *Nondestructive Evaluation Physics : Magnetism.* Accessed: Apr. 30, 2026. [Online]. Available: https://www.nde-ed.org/Physics/Magnetism/MagneticMatls.xhtml.

[54] P. Singh and S. Kumar, "Laser-assisted stress reduction in molybdenum microstructures for CMOS compatible MEMS integration," *Sensors and Actuators A: Physical*, vol. 295, pp. 523–531, Aug. 2019, ISSN: 0924-4247. DOI: 10.1016/j.sna.2019.05.020. Accessed: May 25, 2026. [Online]. Available: https://www.sciencedirect.com/science/article/pii/S092442471832096X.

[55] M. S. Gerlt, N. F. Läubli, M. Manser, B. J. Nelson, and J. Dual, "Reduced Etch Lag and High Aspect Ratios by Deep Reactive Ion Etching (DRIE)," *Micromachines*, vol. 12, no. 5, p. 542, May 2021, ISSN: 2072-666X. DOI: 10.3390/mi12050542. Accessed: Apr. 30, 2026. [Online]. Available: https://pmc.ncbi.nlm.nih.gov/articles/PMC8150727/.

[56] B. Wu, A. Kumar, and S. Pamarthy, "High aspect ratio silicon etch: A review," *Journal of Applied Physics*, vol. 108, no. 5, p. 051 101, Sep. 2010, ISSN: 0021-8979. DOI: 10.1063/1.3474652. Accessed: May 25, 2026. [Online]. Available: https://doi.org/10.1063/1.3474652.

[57] J. W. Coburn and H. F. Winters, "Plasma etching—A discussion of mechanisms," *Journal of Vacuum Science and Technology*, vol. 16, no. 2, pp. 391–403, Mar. 1979, ISSN: 0022-5355. DOI: 10.1116/1.569958. Accessed: May 25, 2026. [Online]. Available: https://doi.org/10.1116/1.569958.

[58] K. Williams, K. Gupta, and M. Wasilik, "Etch rates for micromachining processing-Part II," *Journal of Microelectromechanical Systems*, vol. 12, no. 6, pp. 761–778, Dec. 2003, ISSN: 1941-0158. DOI: 10.1109/JMEMS.2003.820936. Accessed: May 25, 2026. [Online]. Available: https://ieeexplore.ieee.org/document/1257354.

[59] "Deep reactive ion etching," en-US, in *Handbook of Silicon Based MEMS Materials and Technologies*, Elsevier, Jan. 2020, pp. 417–446. DOI: 10.1016/B978-0-12-817786-0.00016-5. Accessed: May 25, 2026. [Online]. Available: https://www.sciencedirect.com/science/chapter/edited-volume/pii/B9780128177860000165.

[60] F. Laermer and A. Schilp, "Method of anisotropically etching silicon," US5501893A, Mar. 1996. Accessed: Apr. 1, 2026. [Online]. Available: https://patents.google.com/patent/US5501893A/en.

[61] J. Anguita and F. Briones, "HF/H2O vapor etching of SiO2 sacrificial layer for large-area surface-micromachined membranes," *Sensors and Actuators A: Physical*, vol. 64, no. 3, pp. 247–251, Jan. 1998, ISSN: 0924-4247. DOI: 10.1016/S0924-4247(97)01628-2. Accessed: May 25, 2026. [Online]. Available: https://www.sciencedirect.com/science/article/pii/S0924424797016282.

[62] C. Mastrangelo and C. Hsu, "Mechanical stability and adhesion of microstructures under capillary forces. I. Basic theory," *Journal of Microelectromechanical Systems*, vol. 2, no. 1, pp. 33–43, Mar. 1993, ISSN: 1941-0158. DOI: 10.1109/84.232593. Accessed: May 25, 2026. [Online]. Available: https://ieeexplore.ieee.org/document/232593.

[63] M. P. F. Wopereis, N. Bouman, S. Dutta, P. G. Steeneken, F. Alijani, and G. J. Verbiest, "Tuning dissipation dilution in 2D material resonators by MEMS-induced tension," *Journal of Applied Physics*, vol. 136, no. 1, p. 014 302, Jul. 2024, ISSN: 0021-8979. DOI: 10.1063/5.0203122. Accessed: Mar. 27, 2025. [Online]. Available: https://doi.org/10.1063/5.0203122.

[64] V. S. Pawar, P. K. Menon, A. L. Murty, P. Pal, and A. K. Pandey, "Influence of scalloping on electrostatic forces in comb drive microdevices," en, *ISSS Journal of Micro and Smart Systems*, vol. 8, no. 2, pp. 127–134, Nov. 2019, ISSN: 2509-7997. DOI: 10.1007/s41683-019-00042-0. Accessed: May 12, 2026. [Online]. Available: https://doi.org/10.1007/s41683-019-00042-0.

[65] J. S. Park et al., “Low-temperature smoothing method of scalloped DRIE trench by post-dry etching process based on SF6 plasma,” en, *Micro and Nano Systems Letters*, vol. 8, no. 1, p. 14, Aug. 2020, ISSN: 2213-9621. DOI: 10.1186/s40486-020-00116-x. Accessed: May 12, 2026. [Online]. Available: https://doi.org/10.1186/s40486-020-00116-x.

[66] A. P. Singulani, H. Ceric, L. Filipovic, and E. Langer, “Impact of bosch scallops dimensions on stress of an open through Silicon Via technology,” in *2013 14th International Conference on Thermal, Mechanical and Multi-Physics Simulation and Experiments in Microelectronics and Microsystems (EuroSimE)*, Apr. 2013, pp. 1–6. DOI: 10.1109/EuroSimE.2013.6529938. Accessed: May 12, 2026. [Online]. Available: https://ieeexplore.ieee.org/document/6529938.

[67] Y. Zhang et al., “Effects of Mask Material on Lateral Undercut of Silicon Dry Etching,” *Micromachines*, vol. 14, no. 2, p. 306, Jan. 2023, ISSN: 2072-666X. DOI: 10.3390/mi14020306. Accessed: May 22, 2026. [Online]. Available: https://pmc.ncbi.nlm.nih.gov/articles/PMC9966973/.

[68] M. Hosseini, G. Zhu, and Y.-A. Peter, “A new formulation of fringing capacitance and its application to the control of parallel-plate electrostatic micro actuators,” en, *Analog Integrated Circuits and Signal Processing*, vol. 53, no. 2, pp. 119–128, Dec. 2007, ISSN: 1573-1979. DOI: 10.1007/s10470-007-9067-3. Accessed: Dec. 30, 2025. [Online]. Available: https://doi.org/10.1007/s10470-007-9067-3.

[69] Y. Nemirovsky and O. Bochobza-Degani, “A methodology and model for the pull-in parameters of electrostatic actuators,” *Journal of Microelectromechanical Systems*, vol. 10, no. 4, pp. 601–615, Dec. 2001, ISSN: 1941-0158. DOI: 10.1109/84.967384. Accessed: Dec. 30, 2025. [Online]. Available: https://ieeexplore.ieee.org/document/967384.

[70] Q.-A. Huang, M. Qin, B. Zhang, J. Sin, and M. Poon, “A field-enhanced generation model for field emission from p-type silicon,” *IEEE Electron Device Letters*, vol. 18, no. 12, pp. 616–618, Dec. 1997, ISSN: 1558-0563. DOI: 10.1109/55.644088. Accessed: Mar. 13, 2026. [Online]. Available: https://ieeexplore.ieee.org/document/644088.

[71] H. Wang, A. M. Loveless, A. M. Darr, and A. L. Garner, “Transitions between field emission and vacuum breakdown in nanoscale gaps,” en, *Journal of Vacuum Science & Technology B*, vol. 40, no. 6, p. 062 805, Dec. 2022, ISSN: 2166-2746, 2166-2754. DOI: 10.1116/6.0002160. Accessed: Mar. 13, 2026. [Online]. Available: https://pubs.aip.org/jvb/article/40/6/062805/2844494/Transitions-between-field-emission-and-vacuum.

[72] P. Oles, A. Breymesser, O. Blank, and P. Hadley, “Integrated sub-micron vacuum gaps in semiconductor devices,” *Applied Physics Letters*, vol. 121, no. 6, p. 062 107, Aug. 2022, ISSN: 0003-6951. DOI: 10.1063/5.0097043. Accessed: Mar. 13, 2026. [Online]. Available: https://doi.org/10.1063/5.0097043.

[73] Y. Fu, P. Zhang, J. P. Verboncoeur, and X. Wang, "Electrical breakdown from macro to micro/nano scales: A tutorial and a review of the state of the art," en, *Plasma Research Express*, vol. 2, no. 1, p. 013 001, Mar. 2020, ISSN: 2516-1067. DOI: 10.1088/2516-1067/ab6c84. Accessed: Mar. 13, 2026. [Online]. Available: https://iopscience.iop.org/article/10.1088/2516-1067/ab6c84.

[74] H. C. Hamaker, "The London—van der Waals attraction between spherical particles," *Physica*, vol. 4, no. 10, pp. 1058–1072, Oct. 1937, ISSN: 0031-8914. DOI: 10.1016/S0031-8914(37)80203-7. Accessed: Mar. 13, 2026. [Online]. Available: https://www.sciencedirect.com/science/article/pii/S0031891437802037.

[75] *Intermolecular and Surface Forces*, en, ISBN: 9780123751829. Accessed: Mar. 13, 2026. [Online]. Available: http://p5070-www.sciencedirect.com/book/monograph/9780123751829/intermolecular-and-surface-forces.

[76] J. Fu et al., "Improving sidewall roughness by combined RIE-Bosch process," *Materials Science in Semiconductor Processing*, vol. 83, pp. 186–191, Aug. 2018, ISSN: 1369-8001. DOI: 10.1016/j.mssp.2018.04.033. Accessed: May 5, 2026. [Online]. Available: https://www.sciencedirect.com/science/article/pii/S1369800118305419.

[77] M. Chabloz, Y. Sakai, T. Matsuura, and K. Tsutsumi, "Improvement of sidewall roughness in deep silicon etching," en, *Microsystem Technologies*, vol. 6, no. 3, pp. 86–89, Feb. 2000, ISSN: 1432-1858. DOI: 10.1007/s005420050003. Accessed: May 5, 2026. [Online]. Available: https://doi.org/10.1007/s005420050003.

[78] L. M. Phinney, B. B. McKenzie, J. A. Ohlhausen, T. E. Buchheit, and R. J. Shul, "Characterization of SOI MEMS Sidewall Roughness," en, American Society of Mechanical Engineers Digital Collection, Aug. 2012, pp. 187–193. DOI: 10.1115/IMECE2011-62593. Accessed: May 5, 2026. [Online]. Available: https://dx.doi.org/10.1115/IMECE2011-62593.

[79] T. Kim and J. Lee, "Fabrication and characterization of silicon-on-insulator wafers," en, *Micro and Nano Systems Letters*, vol. 11, no. 1, p. 15, Nov. 2023, ISSN: 2213-9621. DOI: 10.1186/s40486-023-00181-y. Accessed: May 6, 2026. [Online]. Available: https://doi.org/10.1186/s40486-023-00181-y.

[80] Y. I. Rabinovich, J. J. Adler, A. Ata, R. K. Singh, and B. M. Moudgil, "Adhesion between Nanoscale Rough Surfaces: I. Role of Asperity Geometry," *Journal of Colloid and Interface Science*, vol. 232, no. 1, pp. 10–16, Dec. 2000, ISSN: 0021-9797. DOI: 10.1006/jcis.2000.7167. Accessed: May 6, 2026. [Online]. Available: https://www.sciencedirect.com/science/article/pii/S0021979700971674.

[81] C. Truesdell, "Timoshenko's History of Strength of Materials (1953)," en, in *An Idiot's Fugitive Essays on Science: Methods, Criticism, Training, Circumstances*, C. Truesdell, Ed., New York, NY: Springer, 1984, pp. 251–253, ISBN: 978-1-4613-8185-3. DOI: 10.1007/978-1-4613-8185-3_30. Accessed: May 26, 2026. [Online]. Available: https://doi.org/10.1007/978-1-4613-8185-3_30.

[82] H. Perez Garza, "Development of Nanotools for Applications in (sub-)Femtofluidics and Graphene Technologies," Delft University of Technology, 2015. DOI: 10.4233/UUID:CA9E559B-EC04-4D4F-AC52-BF94B2E901E4. Accessed: Mar. 25, 2025. [Online]. Available: http://resolver.tudelft.nl/uuid:ca9e559b-ec04-4d4f-ac52-bf94b2e901e4.

[83] M. K. Ghatkesar, *Thermal and Piezo Actuators*, Course lecture, TU Delft, Feb. 2021.

[84] Y. M. Kozlovskii and S. V. Stankus, "Linear thermal expansion coefficient of monocrystalline silicon," en, *Thermophysics and Aeromechanics*, vol. 31, no. 6, pp. 1289–1292, Nov. 2024, ISSN: 1531-8699. DOI: 10.1134/S0869864324060210. Accessed: Feb. 11, 2026. [Online]. Available: https://doi.org/10.1134/S0869864324060210.

[85] T. Namazu, Y. Isono, and T. Tanaka, "Plastic deformation of nanometric single crystal silicon wire in AFM bending test at intermediate temperatures," *Journal of Microelectromechanical Systems*, vol. 11, no. 2, pp. 125–135, Apr. 2002, ISSN: 1941-0158. DOI: 10.1109/84.993447. Accessed: Jan. 20, 2026. [Online]. Available: https://ieeexplore.ieee.org/document/993447.

[86] N. Williams, H. Silva, and A. Gokirmak, "Finite element analysis of scaling of silicon micro-thermoelectric generators to nanowire dimensions," *Journal of Renewable and Sustainable Energy*, vol. 4, Jul. 2012. DOI: 10.1063/1.4738592.

[87] X. Fan et al., "Systematic investigations on doping dependent thermal transport properties of single crystal silicon by time-domain thermoreflectance measurements," *International Journal of Thermal Sciences*, vol. 177, p. 107 558, Jul. 2022, ISSN: 1290-0729. DOI: 10.1016/j.ijthermalsci.2022.107558. Accessed: Apr. 21, 2026. [Online]. Available: https://www.sciencedirect.com/science/article/pii/S1290072922000977.

[88] M. Sinclair, *A high force low area MEMS thermal actuator*, Redmond WA, 2000. DOI: 10.1109/ITHERM.2000.866818. [Online]. Available: https://ieeexplore-ieee-org.tudelft.idm.oclc.org/document/866818.

[89] T. R. Hart, R. L. Aggarwal, and B. Lax, "Temperature Dependence of Raman Scattering in Silicon," *Physical Review B*, vol. 1, no. 2, pp. 638–642, Jan. 1970. DOI: 10.1103/PhysRevB.1.638. Accessed: Apr. 20, 2026. [Online]. Available: https://link.aps.org/doi/10.1103/PhysRevB.1.638.

[90] R. Tsu and J. G. Hernandez, "Temperature dependence of silicon Raman lines," en, *Applied Physics Letters*, vol. 41, no. 11, pp. 1016–1018, Dec. 1982, ISSN: 0003-6951, 1077-3118. DOI: 10.1063/1.93394. Accessed: Apr. 20, 2026. [Online]. Available: https://pubs.aip.org/apl/article/41/11/1016/48140/Temperature-dependence-of-silicon-Raman-lines.

[91] M. R. Abel, S. Graham, J. R. Serrano, S. P. Kearney, and L. M. Phinney, "Raman thermometry of polysilicon microelectro-mechanical systems in the presence of an evolving stress," English, *Journal of Heat Transfer*, vol. 129, no. 3, pp. 329–334, 2007, ISSN: 0022-1481. DOI: 10.1115/1.2409996.

[92] C. B. Saltonstall, J. Serrano, P. M. Norris, P. E. Hopkins, and T. E. Beechem, "Single element Raman thermometry," *Review of Scientific Instruments*, vol. 84, no. 6, p. 064 903, Jun. 2013, ISSN: 0034-6748. DOI: 10.1063/1.4810850. Accessed: Oct. 27, 2025. [Online]. Available: https://doi.org/10.1063/1.4810850.

[93] R. Storn and K. Price, "Differential Evolution – A Simple and Efficient Heuristic for global Optimization over Continuous Spaces," en, *Journal of Global Optimization*, vol. 11, no. 4, pp. 341–359, Dec. 1997, ISSN: 1573-2916. DOI: 10.1023/A:1008202821328. Accessed: Apr. 20, 2026. [Online]. Available: https://doi.org/10.1023/A:1008202821328.

[94] K. S. Novoselov et al., "Electric Field Effect in Atomically Thin Carbon Films," *Science*, vol. 306, no. 5696, pp. 666–669, Oct. 2004. DOI: 10.1126/science.1102896. Accessed: May 15, 2025. [Online]. Available: https://www.science.org/doi/10.1126/science.1102896.

[95] P. R. Wallace, "The Band Theory of Graphite," *Physical Review*, vol. 71, no. 9, pp. 622–634, May 1947. DOI: 10.1103/PhysRev.71.622. Accessed: May 15, 2025. [Online]. Available: https://link.aps.org/doi/10.1103/PhysRev.71.622.

[96] A. K. Geim and K. S. Novoselov, "The rise of graphene," en, *Nature Materials*, vol. 6, no. 3, pp. 183–191, Mar. 2007, ISSN: 1476-4660. DOI: 10.1038/nmat1849. Accessed: May 6, 2026. [Online]. Available: https://www.nature.com/articles/nmat1849.

[97] K. Kinoshita et al., "Dry release transfer of graphene and few-layer h-BN by utilizing thermoplasticity of polypropylene carbonate," en, *npj 2D Materials and Applications*, vol. 3, no. 1, pp. 1–8, May 2019, ISSN: 2397-7132. DOI: 10.1038/s41699-019-0104-8. Accessed: Mar. 27, 2025. [Online]. Available: https://www.nature.com/articles/s41699-019-0104-8.

[98] X. Li et al., "Transfer of Large-Area Graphene Films for High-Performance Transparent Conductive Electrodes," *Nano Letters*, vol. 9, no. 12, pp. 4359–4363, Dec. 2009, ISSN: 1530-6984. DOI: 10.1021/nl902623y. Accessed: May 6, 2026. [Online]. Available: https://doi.org/10.1021/nl902623y.

[99] V. Mukundan, P. Ponce, H. E. Butterfield, and B. L. Pruitt, "Modeling and Characterization of Electrostatic Comb-drive Actuators in Conducting Liquid Media," *Journal of micromechanics and microengineering : structures, devices, and systems*, vol. 19, no. 6, pp. 1–9, Jun. 2009, ISSN: 0960-1317. DOI: 10.1088/0960-1317/19/6/065008. Accessed: Mar. 27, 2025. [Online]. Available: https://www.ncbi.nlm.nih.gov/pmc/articles/PMC2762223/.

[100] V. La Ferrara, "Nanostructured Materials Driven by Dielectrophoresis on Nanoelectrodes Patterned by Focused Ion Beam," en, in *FIB Nanostructures*, Z. M. Wang, Ed., Cham: Springer International Publishing, 2013, pp. 341–357, ISBN: 978-3-319-02874-3. DOI: 10.1007/978-3-319-02874-3_13. Accessed: May 19, 2026. [Online]. Available: https://doi.org/10.1007/978-3-319-02874-3_13.

[101] S. Hari, A. M. Goossens, L. M. K. Vandersypen, and C. W. Hagen, "Electron Beam Induced Deposition on graphene on silicon oxide and hexagonal boron nitride: A comparison of substrates," *Microelectronic Engineering*, Nano Fabrication 2013, vol. 121, pp. 122–126, Jun. 2014, ISSN: 0167-9317. DOI: 10.1016/j.mee.2014.04.037. Accessed: Jun. 1, 2025. [Online]. Available: https://www.sciencedirect.com/science/article/pii/S0167931714001841.

[102] W. Giurlani, E. Berretti, and A. Lavacchi, "Measuring the Thickness of Metal Films: A Selection Guide to the Most Suitable Technique," vol. 2, May 2020, p. 12. DOI: 10.3390/CIWC2020-06823.

[103] J. Mayer, L. A. Giannuzzi, T. Kamino, and J. Michael, "TEM Sample Preparation and FIB-Induced Damage," en, *MRS Bulletin*, vol. 32, no. 5, pp. 400–407, May 2007, ISSN: 1938-1425. DOI: 10.1557/mrs2007.63. Accessed: Apr. 29, 2026. [Online]. Available: https://doi.org/10.1557/mrs2007.63.

[104] H. Zhang, B. E. Schuster, Q. Wei, and K. T. Ramesh, "The design of accurate micro-compression experiments," *Scripta Materialia*, vol. 54, no. 2, pp. 181–186, Jan. 2006, ISSN: 1359-6462. DOI: 10.1016/j.scriptamat.2005.06.043. Accessed: Apr. 29, 2026. [Online]. Available: https://www.sciencedirect.com/science/article/pii/S1359646205005944.

[105] D. Kiener, C. Motz, M. Rester, M. Jenko, and G. Dehm, "FIB damage of Cu and possible consequences for miniaturized mechanical tests," *Materials Science and Engineering: A*, vol. 459, no. 1, pp. 262–272, Jun. 2007, ISSN: 0921-5093. DOI: 10.1016/j.msea.2007.01.046. Accessed: Apr. 29, 2026. [Online]. Available: https://www.sciencedirect.com/science/article/pii/S0921509307000597.

[106] T. Ishitani and T. Yaguchi, "Cross-sectional sample preparation by focused ion beam: A review of ion-sample interaction," en, *Microscopy Research and Technique*, vol. 35, no. 4, pp. 320–333, 1996, ISSN: 1097-0029. DOI: 10.1002/(SICI)1097-0029(19961101)35:4<320::AID-JEMT3>3.0.CO;2-Q. Accessed: Apr. 29, 2026. [Online]. Available: https://onlinelibrary.wiley.com/doi/abs/10.1002/%28SICI%291097-0029%2819961101%2935%3A4%3C320%3A%3AAID-JEMT3%3E3.0.CO%3B2-Q.

[107] M. Schaffer, B. Schaffer, and Q. Ramasse, "Sample preparation for atomic-resolution STEM at low voltages by FIB," *Ultramicroscopy*, vol. 114, pp. 62–71, Mar. 2012, ISSN: 0304-3991. DOI: 10.1016/j.ultramic.2012.01.005. Accessed: Apr. 29, 2026. [Online]. Available: https://www.sciencedirect.com/science/article/pii/S030439911200006X.

[108] S. Lombardo, J. H. Stathis, B. P. Linder, K. L. Pey, F. Palumbo, and C. H. Tung, "Dielectric breakdown mechanisms in gate oxides," *Journal of Applied Physics*, vol. 98, no. 12, p. 121 301, Dec. 2005, ISSN: 0021-8979. DOI: 10.1063/1.2147714. Accessed: May 19, 2026. [Online]. Available: https://doi.org/10.1063/1.2147714.

[109] M. Lenzlinger and E. H. Snow, "Fowler-Nordheim Tunneling into Thermally Grown SiO2," *Journal of Applied Physics*, vol. 40, no. 1, pp. 278–283, Jan. 1969, ISSN: 0021-8979. DOI: 10.1063/1.1657043. Accessed: May 19, 2026. [Online]. Available: https://doi.org/10.1063/1.1657043.

[110] "PDMS mechanical properties and applications," *ACS Materials Au*, 2024. [Online]. Available: https://pubs.acs.org/doi/10.1021/acsmaterialsau.4c00042.

[111] "SEBS elastomer characterization for microfluidic applications," *PMC*, vol. 10372055, 2023. [Online]. Available: https://www.ncbi.nlm.nih.gov/pmc/articles/PMC10372055/.

[112] "SU-8 photoresist mechanical characterization," *PMC*, vol. 12736521, 2023. [Online]. Available: https://www.ncbi.nlm.nih.gov/pmc/articles/PMC12736521/.

[113] U. B. Lab, "Polyimide neural probe review," University of Southern California, Tech. Rep., 2016. [Online]. Available: http://biomems.usc.edu/publications/2016/2016_mm_probe_review.pdf.

[114] "Mechanical properties of MEMS polysilicon," *PMC*, vol. 6843387, 2019. [Online]. Available: https://www.ncbi.nlm.nih.gov/pmc/articles/PMC6843387/.

[115] "Copper mechanical properties in microelectronics," *ResearchGate*, 2008. [Online]. Available: https://www.researchgate.net/publication/222897200.

[116] DTIC, "Silicon nitride mechanical characterization," Defense Technical Information Center, Tech. Rep. ADA422530, 2004. [Online]. Available: https://apps.dtic.mil/sti/tr/pdf/ADA422530.pdf.